PB89-159057

Validation Testing of New Mechanisms with Outdoor Chamber Data. Volume 3 Calculation of Photochemical Reaction Photolysis Rates in the UNC Outdoor Chamber

North Carolina Univ. at Chapel Hill

Prepared for

Environmental Protection Agency
Research Triangle Park, NC

Jan 89

U.S. Department of Commerce
National Technical Information Service
NTIS

TECHNICAL REPORT DATA
(Please read Instructions on the reverse before completing)

1. REPORT NO. EPA/600/3-89/010c	2. PB89 159057/AS
4. TITLE AND SUBTITLE: VALIDATION TESTING OF NEW MECHANISMS WITH OUTDOOR CHAMBER DATA, VOLUME 3: CALCULATION OF PHOTOCHEMICAL REACTION PHOTOLYSIS RATES IN THE UNC OUTDOOR CHAMBER	5. REPORT DATE: January 1989 6. PERFORMING ORGANIZATION CODE
7. AUTHOR(S): H. E. Jeffries, K. G. Sexton, J. R. Arnold, T. L. Kale	8. PERFORMING ORGANIZATION REPORT NO.
9. PERFORMING ORGANIZATION NAME AND ADDRESS: School of Public Health, University of North Carolina, Chapel Hill, North Carolina 27514	10. PROGRAM ELEMENT NO. A101/B/63/20/6031 (FY-88) 11. CONTRACT/GRANT NO. Cooperative Agreement 813107
12. SPONSORING AGENCY NAME AND ADDRESS: Atmospheric Research & Exposure Assessment Lab., Office of Research and Development, U.S. Environmental Protection Agency, Research Triangle Park, North Carolina 27711	13. TYPE OF REPORT AND PERIOD COVERED: Final (4/86 - 9/88) 14. SPONSORING AGENCY CODE: EPA 600/09
15. SUPPLEMENTARY NOTES	

16. ABSTRACT

A new model is described for computing in-chamber actinic flux using site specific conditions that include time of day, air pressure, total column ozone, total column water vapor, relative humidity, aerosol type, aerosol optical density at 500 nm, and the spectral albedo of the ground. Included in this model are a highly accurate solar coordinate model, two broad band models for predicting the Total Solar Radiation (TSR) and Eppley Ultraviolet Radiometer irradiances, a TFE film transmission model, a total chamber transmission model, a reflective floor model, and a treatment for clouds. This model runs on MS-DOS/PC type machines. A description of how these models were used to compute the in-chamber actinic flux every 16-minutes for every day in the UNC database is given. A description is also given of how these new actinic fluxes were used with kinetic data on species absorption cross sections and quantum yields to compute the photolysis rates of 20 reactions. A separate volume contains the appendices for this document.

17. KEY WORDS AND DOCUMENT ANALYSIS		
a. DESCRIPTORS	b. IDENTIFIERS/OPEN ENDED TERMS	c. COSATI Field/Group

18. DISTRIBUTION STATEMENT: RELEASE TO PUBLIC	19. SECURITY CLASS (This Report): UNCLASSIFIED 20. SECURITY CLASS (This page): UNCLASSIFIED	21. NO. OF PAGES: 105 22. PRICE: PS2 1.95 / A6.95 MF

EPA Form 2220-1 (9-73)

PB89-159057

EPA/600/3-89/010c
January 1989

Validation Testing of New Mechanisms With Outdoor Chamber Data

Volume 3: Calculation of Photochemical Reaction Photolysis Rates in the UNC Outdoor Chamber

H. E. Jeffries, K. G. Sexton,
J. R. Arnold, T. L. Kale

Department of Environmental Sciences
and Engineering
School of Public Health
University of North Carolina
Chapel Hill, N.C. 27514

In partial fullfilment of
Cooperative Agreement 813107

Project Officer
Marcia Dodge

Atmospheric Chemistry and Physics Division
Atmospheric Sciences Research Laboratory
Research Triangle Park, N.C. 27711

ATMOSPHERIC RESEARCH AND EXPOSURE ASSESSMENT LABORATORY
OFFICE OF RESEARCH AND DEVELOPMENT
U.S. ENVIRONMENTAL PROTECTION AGENCY
RESEARCH TRIANGLE PARK, NC 27711

REPRODUCED BY
U.S. DEPARTMENT OF COMMERCE
NATIONAL TECHNICAL INFORMATION SERVICE
SPRINGFIELD, VA. 22161

DISCLAIMER

This report has been reviewed by the U. S. Environmental Protection Agency, and approved for publication. Approval does not signify that the contents necessarily reflect the views and policies of the U. S. Environmental Protection Agency, nor does mention of trade names or commercial products constitute endorsement or recommendation for use.

Abstract

This volume first describes a new model for computing the in-chamber actinic flux using site specific conditions that include: time of day, air pressure, total column ozone, total column water vapor, relative humidity, aerosol type, aerosol optical density at 500 nm, and the spectral albedo of the ground. Included in this model are a highly accurate solar coordinate model, two broad band models for predicting the Total Solar Radiation (TSR) and Eppley Ultraviolet Radiometer irradiances, a TFE film transmission model, a total chamber transmission model, a reflective floor model, and a treatment for clouds. This model runs on MS-DOS/PC type machines. A description of how these models were used to compute the in-chamber actinic flux every 16-minutes for every day in the UNC SegFile database is given.

The document then describes how these new actinic fluxes were used with kinetic data on species absorption cross sections and quantum yields to compute the photolysis rates of up to 20 reactions for each day in the UNC SegFile data base.

A separate volume contains the appendies for this document. It includes the data base of climate and solar radiation variables needed by the models, plots of broad band model predictions compared with observed site TSR and UV irradiance data for each day in the UNC data base, and selected examples of plots of the predicted in-chamber NO_2 and HCHO to radicals photolysis rates inside the chamber. A third appendix lists the molecular absorption cross sections and reaction quantum yields used. The final appendices provide complete listings of the computer code for all models and sub-models used.

Contents

1 Calculation of Actinic Flux 1

Need . . . 1

The Models . . . 4

Calculation of Solar Zenith and Azimuth Angles from Site Clock Time . . . 5

Solar Flux Models . . . 8

Inputs Needed For the Calculation of Actinic Flux . . . 20

Steps in the Calculation of Actinic Flux . . . 22

Daily Atmospheric Conditions . . . 23

- Clear Model . . . 23
- Cloudy Model . . . 23

Discussion of Step Four: the Calculation of In-chamber Irradiances . . . 26

FEP Teflon Film Transmission Model . . . 30

UNC Chamber Characteristics . . . 32

The UNC Chamber Transmission Model . . . 35

Measurement and Modeling of In-Chamber Irradiances . . . 44

- Broadband UV Irradiances . . . 45
- Spectral Irradiances . . . 47

Calculation of In-Chamber Actinic Flux . . . 52

In-chamber Actinic Flux . . . 55

In-chamber Photolysis Rates . . . 56

2 **Calculating the Rate of Photolytic Reactions** 63

Introduction 63

Idealized Spectral Quantities and Units 66

Evaluation of the Rate Equation 67

Approximation Methods 70

Interval Quantities and Units 71

Combinations of Spectrum Types 72

Computing Interval-Averaged Reaction Potential 75

Computing Double Trapezoidal Integrals 78

Problems with Sources of Photolytic Data 83

Methodology for Rate Calculation 84

Case: Reaction Potential Spectra as Bars 84
Case: Reaction Potential Spectra as Points 85

Practical Considerations 87

Data Input Formats 87
CHMRATE Program Commands 88

References 93

Tables

1. Physical characteristics of UNC chamber. 33
2. Chamber floor and walls reflectivity. 36
3. Comparison of photolysis rates calculated by Carter's procedure and by UNC's procedure. 65
4. Example of a cross section and quantum input file. 88
5. Example of a CHMRATE command file. 90
6. Example two of a CHMRATE command file. 91
7. Example of an external list file for CHMRATE. 92
8. Example of an external list file of IRRAD commands for CHMRATE. 92

Figures

1. The relative rates of selected photodissociation reactions. 2
2. Sun's position for five summer and fall months at the UNC Site 8
3. Extraterrestrial solar and surface spectrum and direct beam spectral transmission functions 10
4. Monthly averaged conditions affecting surface solar radiation for central North Carolina 11
5. Global, direct, and diffuse irradiances computed by the Dave and Halpern model and by the UNC JSPECTRA model 14
6. Diffuse spherical transmissions computed by the Peterson model and by the UNC JSPECTRA model 15
7. Licor spectroradiometer measured irradiances and JSPECTRA model predictions for two days at the UNC site 16
8. Licor spectroradiometer measured irradiances and JSPECTRA model predictions, ultraviolet portion of spectrum 17
9. Schematic showing factors affecting in-chamber radiant flux. 27
10. The Teflon Film Transmission model 32
11. Design of the UNC Dual Outdoor Smog Chamber. 35
12. Licor spectroradiometer spectra in UNC Chamber looking-up and looking-down and the ratio 37
13. Four views of the UNC dual outdoor chamber on 20-Apr-1988 38
14. Angles and areas computed by the Chamber Transmission Model 40
15. Face transmissions and weights computed by the Chamber Transmission Model 41
16. Chamber Average Transmission and the face contributions 42
17. Daily profiles of chamber direct transmission for six months months 44
18. Tower and In-chamber Eppley radiometer irradiances 46
19. Licor Spectroradiometer spectra inside and outside UNC chamber on a low aerosol day 49
20. Licor Spectroradiometer spectra inside and outside the UNC chamber 50
21. Licor Spectroradiometer spectra inside and JSPECTRA model predictions. 52
22. Global actinic flux and its components for solar noon, August 5, 1984 56
23. Ratio of global actinic flux and its components inside to outside for solar noon August 5, 1984 57

24a. Actinic Flux Spectra inside and outside UNC Chamber for morning of August 5, 1984 58

24b. Actinic Flux Spectra inside and outside UNC Chamber for afternoon of August 5, 1984 59

25. In-chamber NO_2 and HCHO photolysis rates 61
26. In-chamber O_3 photolysis rates 62
27. Comparison of Carter's and UNC's NO_2 Photolytic Data. 66
28. Illustrations of some of difficulties in evaluating the photolysis rate. 69
29. Example of a mismatch of irradiance and reaction potential intervals. 71
30. The interval components in the calculation of the NO_2 photolysis rate. 73
31. The combinations of irradiance and reaction potential spectrum types. 75
32. Example of 'hunt' algorithm for locating bounding interval in a one-way table. 77

33. The double trapezoid rule method 81
34. Comparison of trapezoid rule and double trapezoid rule 82

Acknowledgements

We very much appreciate the extra efforts of Dr. Marcia Dodge that allow us to acquire the Licor automatic scanning spectroradiometer used in this project. This instrument allowed us to make measurements that confirmed the accuracy of the model described here.

The assistance of Allen Hendler, graduate student at UNC, in clarifying the spectral transmission of clouds in the UV region is greatly appreciated.

We also thank Ken Daisy, student at UNC, for his careful efforts in performing quality assurance activities on all of our data files.

1

Calculation of Actinic Flux

Need

To operate a state-of-the-science photochemical kinetics model requires the specification of the time-dependent rates for as many as twenty photolytic reactions including the following:

$$NO_2 \xrightarrow{h\nu} NO + O \quad (1)$$

$$O_3 \xrightarrow{h\nu} O + O_2 \quad (2)$$

$$O_3 \xrightarrow{h\nu} O^{1D} + O_2 \quad (3)$$

$$HCHO \xrightarrow{h\nu} H^{\cdot} + HCO^{\cdot} \quad (4)$$

$$HCHO \xrightarrow{h\nu} H_2 + CO \quad (5)$$

$$CH_3CHO \xrightarrow{h\nu} {}^{\cdot}CH_3 + HCO^{\cdot} \quad (6)$$

These six reactions are cited because they have rates that depend upon different portions of the irradiance spectrum. Figure 1 shows the spectral photolysis rates of five of the reactions above (two pathways for HCHO). In this plot, the rates have been normalized so that the area under each curve is 1.0, thus the magnitude of the "bar" in each interval indicates the fractional contribution of that wavelength interval to the total rate for the species. For example, for reaction 3 nearly 20% of the reaction rate depends upon photons with wavelengths between 306 to 308 nm. Similarly, for HCHO photolysis to radicals, reaction 4, about 24% of the total rate depends upon photons with wavelengths between 312 and 316 nm. Essentially all of the photolysis of HCHO to radicals, all of the photolysis of O_3 to O^{1D}, and all of the photolysis of CH_3CHO occurs below 340 nm. Nitrogen dioxide, on the other

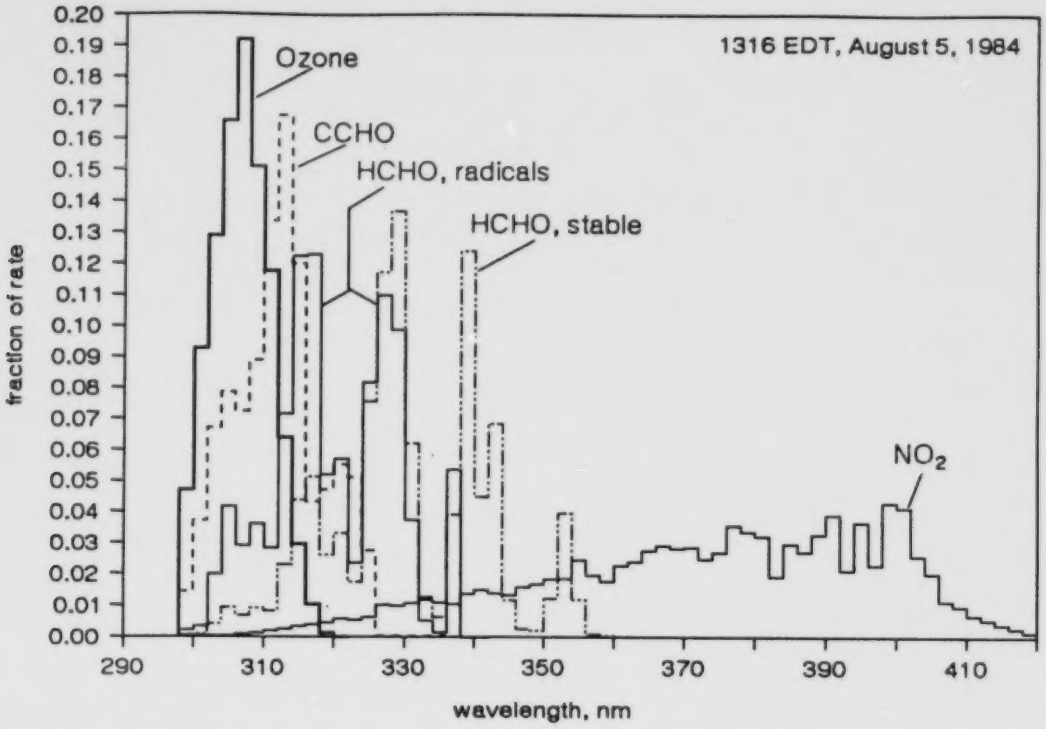

Figure 1. The relative rates of selected photodissociation reactions. The area under each curve has been normalized to 1.0.

hand, has a maximum spectral dependance of less than 5% on any given 2-nm interval between 298–410 nm, and the vast majority of the spectral rate occurs above 340 nm. These differences in spectral response are especially important in outdoor situations because, as the solar zenith angle changes throughout the day, the spectral distribution of solar flux changes. The rate of each reaction cited above, therefore, will have a unique diurnal profile, and the ratio between any two of them will not be constant.

Methods exist to measure directly the photolysis rates of reactions 1 and 3 only.[1,2] Both methods are based upon irradiating particular mixtures containing the absorbing gas in a quartz flow tube and subsequently measuring the concentration of a reaction product or the products resulting from further reactions of a primary reaction product. The rate of the primary photolytic reaction is then calculated from the time of exposure in the quartz tube, the concentration of the photoaceptor species, the concentration of the reaction product, and a formula derived from the kinetics of the over all process. These techniques require precise flows, very precise gas concentrations, precise measurement of temperature in an irradiated field, and for the present systems the measurement of low concentrations of NO or NO_2. In addition, the full spherical (three-dimensional) view of the quartz tube must be careful controlled to determine what radiant flux *is* being measured. These requirements result in expensive and difficult-to-operate instruments. Furthermore, in a situation such as the UNC outdoor chamber, the monitoring of the photolysis rates must be done in a spatial averaged manner, that is, the rates must be determined at a number of different locations spread over a volume of 156,000 liters and these must be done in a short time period so the sun's position remains the same. Finally, having measured the rates of reactions 1 and 3 does not reveal much about the rates of reactions 2, 4, 5, and 6 because of the different spectral dependances for the absorbing molecules in the different reactions.

Considering the need to specify the photolysis rate for twenty or more reactions and the ability to only measure two of these with difficulty, there exists the need to predict or calculate global spectral spherical radiant flux densities (often called "actinic flux") as a function of time, not only in the UNC outdoor chamber, but also in situations where the air quality models that use the mechanisms tested in the chamber are being applied.

Many modelers have not calculated actinic fluxes, but instead have interpolated the tables of actinic fluxes at fixed solar zenith angles (0°, 10°, 20°, ...) which were calculated by Peterson[3] for a fixed set of atmospheric conditions (*e.g.*, O_3 column, aerosol loading). Peterson calculated these tabular fluxes using a modification of the Dave radiation transfer model.[4] The flux values were calculated for just one

atmospheric condition. The Peterson calculations were done more than 13 years ago using a model more than 18 years old.

In the meantime, knowledge about many of the inputs used in the Dave and Peterson models has improved. For example, the extraterrestrial solar flux, which was somewhat uncertain in the Peterson model, has been standardize at a 2-nm resolution over most of the UV and visible spectrum.[5] The best resolution available to Peterson was 5-nm, and he used 10-nm in much of the visible spectrum. The Dave model used a very simple aerosol model with constant—and now thought to be inappropriate—optical properties, yet the aerosol related calculations consumed about 20 hours of mainframe computing time in Peterson's calculations. In the last few years, simple, but effective, parameterized models of solar radiation on horizontal surfaces have been developed.[6,7,8] Jeffries, using the general formulations in several of these simple models, has produced new parameterizations of the diffuse actinic flux at the earth's surface and tested the model's predictions against the older models and against spectral measurements taken with the UNC 2-nm spectroradiometer, both outside and inside the UNC chamber. In addition, Sexton has produced new data on the spectral transmission and reflection of 5-mil Teflon film from which Jeffries developed a mathematical model of solar radiation transmission through this commonly used reactor material. Using these tools, local meteorological conditions, and a geometrical model of the UNC chamber, we have produced a new procedure to calculate the "actinic flux" in the UNC outdoor chamber. Given these high resolution global spectral spherical radiant fluxes, the calculation of reaction rates is relatively straight forward, requiring as additional inputs only laboratory produced absorption spectra and quantum yields for each reaction. The rest of this document describes the method in operational terms; the theoretical foundations and the supporting input data are described in a separate document.[9]

The Models

We will first outline the models and their inputs, and then discuss the details of each step in applying the models in following sections. The goal is to calculate the in-chamber global spectral spherical radiant flux that probably occurred during an experiment conducted on a particular day.

The models are:

- a spectral radiation transfer model (JSMODEL) that needs as inputs:
  - the extraterrestrial solar spectral flux at the appropriate earth-sun distance;

- spectral absorption coefficients for ozone, water vapor, uniformly mixed gases (CO, CO_2, CH_4)
- zenith angle of the sun;
- air pressure;
- total atmospheric column ozone;
- total atmospheric column water vapor;
- the selection of one of three aerosol optical properties models (AEROMOD);
- optical density at 500 nm associated with the lower atmospheric aerosol loading and an associated relative humidity;
- optical density at 500 nm associated with the stratospheric aerosol loading;
- if the user selects the special aerosol model, then he must also specify the wavelength dependance of aerosol scattering above and below 500 nm, the single scattering albedo for the aerosol, and the scattering asymmetry parameter;
- the spectral regional albedo of the surrounding ground;
- the relative humidity temporal profile for the aerosol model;

▷ two broadband radiation transfer models (BBMODEL), one for TSR and one for UV, that are derived from the spectral model above and that need the same inputs as the spectral model;

▷ a high-accuracy program (SOLCALC) to calculate solar coordinates as a function of local standard times;

▷ a mathematical model (FLMTRAN) of the spectral transmission, absorption, and reflection properties of 5-mil FEP Teflon film;

▷ a mathematical model (CHMMODEL) of spectral transmission of the UNC chamber;

▷ a mathematical model (CLDTRAN) of the spectral transmission of clouds.

Each of these models has been implemented as a module of computer code, *i.e.*, the names given above, that can be incorporated into various programs. In addition there is an integrated model that includes all the features of JSMODEL and BBMODEL with a simple command driven interface and extensive output features including the terms that are used to compute the transmissions, the transmissions, and various forms of irradiance. This model is good for single event simulations—a spectroradiometer scan in the chamber—or for diagnosing results. This model is called JSPECTRA.

Calculation of Solar Zenith and Azimuth Angles from Site Clock Time

To calculate the theoretical actinic flux for a given run you must be able to calculate the sun's zenith angle, θ_0, and azimuth, ψ_0, as a function of local daylight time. Such calculations require as input:

- the site location (*i.e.*, latitude, Λ, and longitude, M, in radians), and the time zone displacement, z, in hours;
- three items related to the date:
  - the solar declination, δ, in radians,
  - the value of the equation of time, E, in hours,
  - the relative solar radius, r_υ, unitless.

The last item will not be used until later in the calculations.

The UNC site is located at:

Latitude	35.7083 degrees
Longitude	79.1085 degrees

and the time zone displacement for Eastern Daylight Time is 4.0 hours.

There are many algorithms for computing the solar declination and equation of time, each with varying accuracy. The most accurate methods are those published by the U.S. Naval Observatory, but each formula is only accurate for a single year. At the other extreme are "average" formulas that do not require the year to estimate declination, equation of time, and solar radius. We recommend a procedure described by Barkstrom[10] that is most accurate for years 1970-1995. We have tested this procedure against the "Almanac for Computers," by the U.S. Naval Observatory and found that it was accurate to about 0.15% for solar declination and to about 40 seconds of arc for local hour angles, depending upon the particular day.

The Barkstrom procedure has been used to compute solar declination at true solar noon, the equation of time at noon, and other items related to time for every UNC SegFile run. As described above, these are included in the SOLCLIM database. The Barkstrom procedure has also been implemented as a program module SOLCALC and this is used in each program to calculate the values of δ and E when needed in each main program.

The basic operation of SOLCALC requires as initial input:

Λ –the latitude in radians,

M –the longitude in radians,

z –the local time zone displacement in hours,

and the subroutine SOLARORBIT is used to calculate:

δ –the solar declination in radians,

E –the equation of time, expressed in hours

Once this has been done for a given location and day, then, using the following symbols:

h –local time, hours,

t –true solar time, hours,

ω –hour angle, radians,

ϕ_0 –solar altitude, radians,

the conversion of h into θ_0 and ψ_0 is accomplished by first correcting the local time to true solar time,

$$t = h + z - \left(\frac{12\,M}{\pi}\right) + E$$

and then using the true solar time to find the local hour angle,

$$\omega = (12.0 - t)\left(\frac{15\,\pi}{180}\right).$$

Once the local hour angle is known, the zenith angle can be calculated as

$$\mu = \sin\delta \sin\Lambda + \cos\delta \cos\Lambda \cos\omega$$
$$\theta_0 = \cos^{-1}\mu.$$

The solar altitude is the complement of the solar zenith angle,

$$\phi_0 = (\pi/2) - \theta_0.$$

Once the solar altitude is known, the solar azimuth can be calculated by

$$\nu = \frac{(\sin\phi_0 \sin\Lambda - \sin\delta)}{\cos\phi_0 \cos\Lambda}$$
$$\psi_0 = \cos^{-1}\nu.$$

If $\omega < 0$, $\psi_0 = -\psi_0$. That is, the solar azimuth is positive to the east and negative when the sun is to the west. Figure 2 is a polar diagram showing the sun's path at the UNC site for five summer and fall months. Superimposed on the five arcs are constant local time lines. These lines are "s"-shaped because of the equation of time. Looking at this diagram, we can see that true solar noon occurs at the site between 1300 and 1325 EDT over the course of the summer and fall.

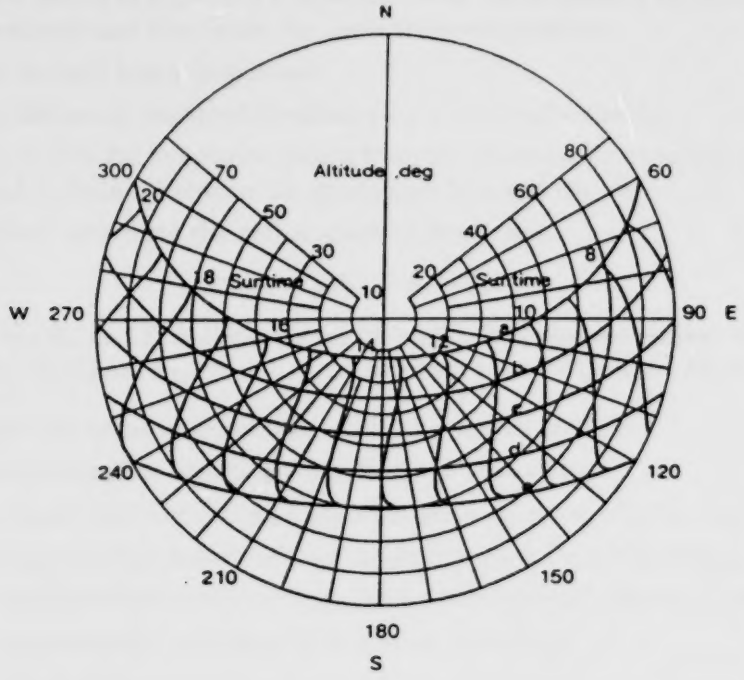

Figure 2. The sun's position for five summer and fall months: a–June 22, b–August 24, c–September 23, d–October 24, e–December 22

Solar Flux Models

We have written four interdependent radiant flux density models which all start with the extraterrestrial solar irradiance, $\mathcal{H}_{0\lambda}$, the radiant flux density outside the earth's atmosphere. We have adopted the World Radiation Center (WRC) extraterrestrial spectrum that was reported in Iqbal.[5] The $\mathcal{H}_{0\lambda}$ values are for the *mean* earth-sun distance. The calculated irradiances must be corrected for the effect of the changing earth-sun distance. This is done by

$$\mathcal{H}_{\lambda} = \frac{\mathcal{H}_{0\lambda}}{r_v^2}$$

where r_v is the *relative earth-sun radius* as discussed in the section above. Values of r_v for all UNC run days are given in the SOLCLIM data base, but, in the programs, they are calculated from the Barkstrom algorithm.

The first model is a spectral irradiance model using spectral transmission functions to attenuate and distribute $\mathcal{H}_{0\lambda}$ into three components:

- $\mathcal{N}_\lambda$–the normal beam irradiance;
- $\mathcal{S}_\lambda$–the diffuse or scattered irradiance on a horizontal surface;
- $\mathcal{R}_\lambda$–the horizontal irradiance arising from the downward component of multiple-reflected radiation between the ground surface and the sky;

which together constitute the global spectral irradiance,

$$\mathcal{G}_\lambda = \mu \mathcal{N}_\lambda + \mathcal{S}_\lambda + \mathcal{R}_\lambda \tag{1}$$

where $\mu = \cos \theta_0$, and θ_0 is the solar zenith angle. It is also convenient to define the direct beam irradiance as, $\mathcal{D}_\lambda = \mu \mathcal{N}_\lambda$. The usual units of $\mathcal{G}_\lambda$ are watt-m^{-2}-nm^{-1}.

The spectral transmission functions in this model include:

$\tau_{r\lambda}$ —transmission resulting from Rayleigh scattering,

$\tau_{w\lambda}$ —transmission resulting from absorption by total column water vapor,

$\tau_{g\lambda}$ —transmission resulting from uniformly-mixed gas absorption,

$\tau_{o\lambda}$ —transmission resulting from absorption by total column ozone,

$\tau_{as\lambda}$ —transmission resulting from aerosol scattering,

$\tau_{aa\lambda}$ —transmission resulting from aerosol absorption.

These functions depend upon sub-models of various atmospheric processes which in turn need values such as Rayleigh scattering coefficient of air, Mie scattering and absorption functions for aerosols, and absorption coefficients for ozone, water vapor, and carbon dioxide.

As an example of the magnitude and effect of these transmission functions, Figure 3 compares the measured UV and visible extraterrestrial solar spectrum and the direct beam surface spectrum predicted by the JSPECTRA model. Also shown in the figure are the calculated transmissions resulting from various absorption and scattering processes that occur in the atmospheric path.

In the upper right plot of Figure 3, water vapor and carbon dioxide absorption are the dominate features over the usual total solar radiation spectrum (TSR) of 0.28—2.8 $m\mu$, and the total water vapor column is a major factor in determining how much TSR is received at the surface. Figure 4 shows the long-term average monthly conditions of column ozone, column water vapor, and aerosol optical density for both absorption and scattering for central North Carolina. As would be expected, the maximum water vapor column and aerosol extinction occurs in the late summer. The maximum total column ozone, however, occurs in the spring.

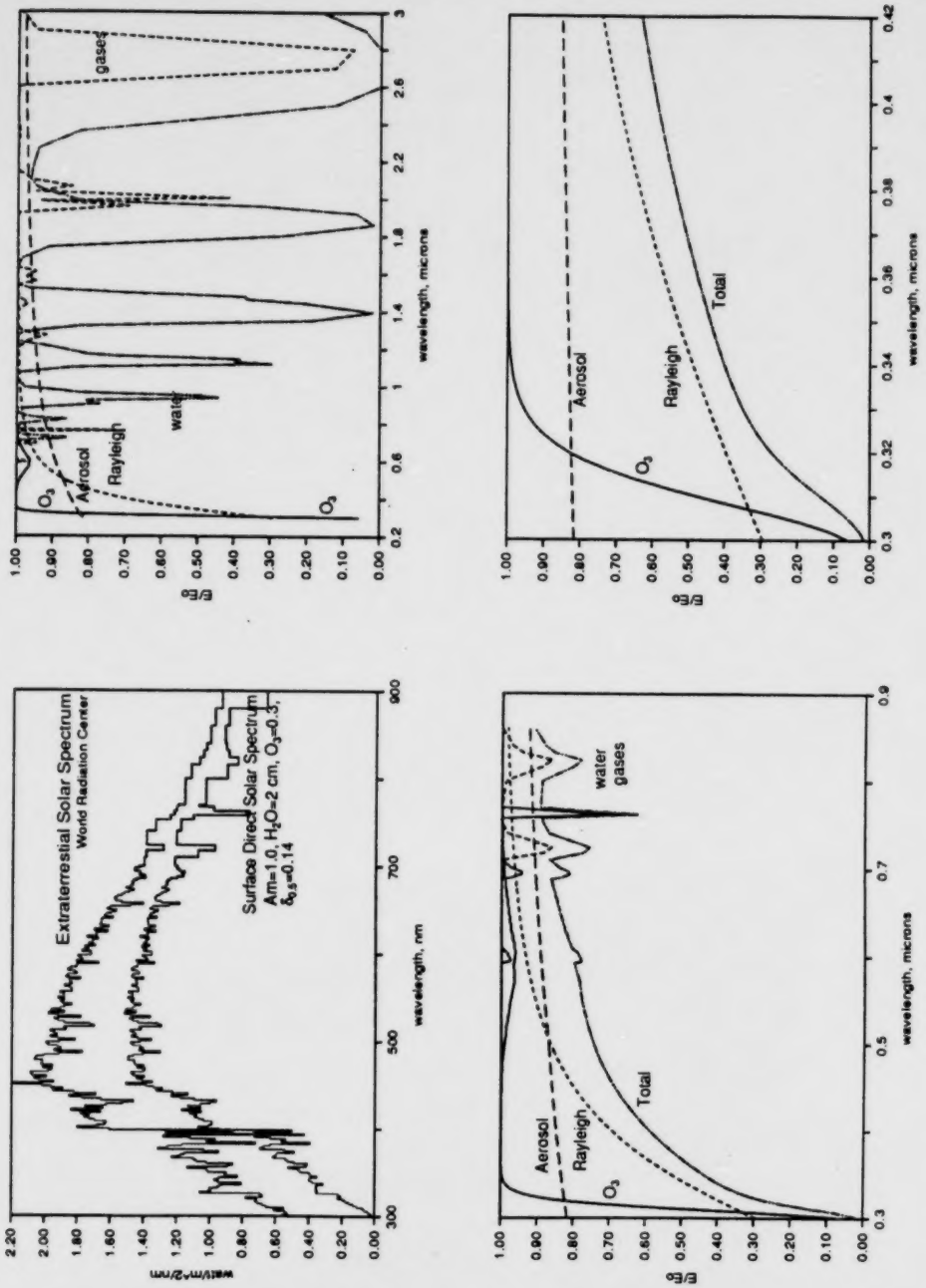

Figure 3. Extraterrestrial solar and surface spectrum and direct beam spectral transmission functions.

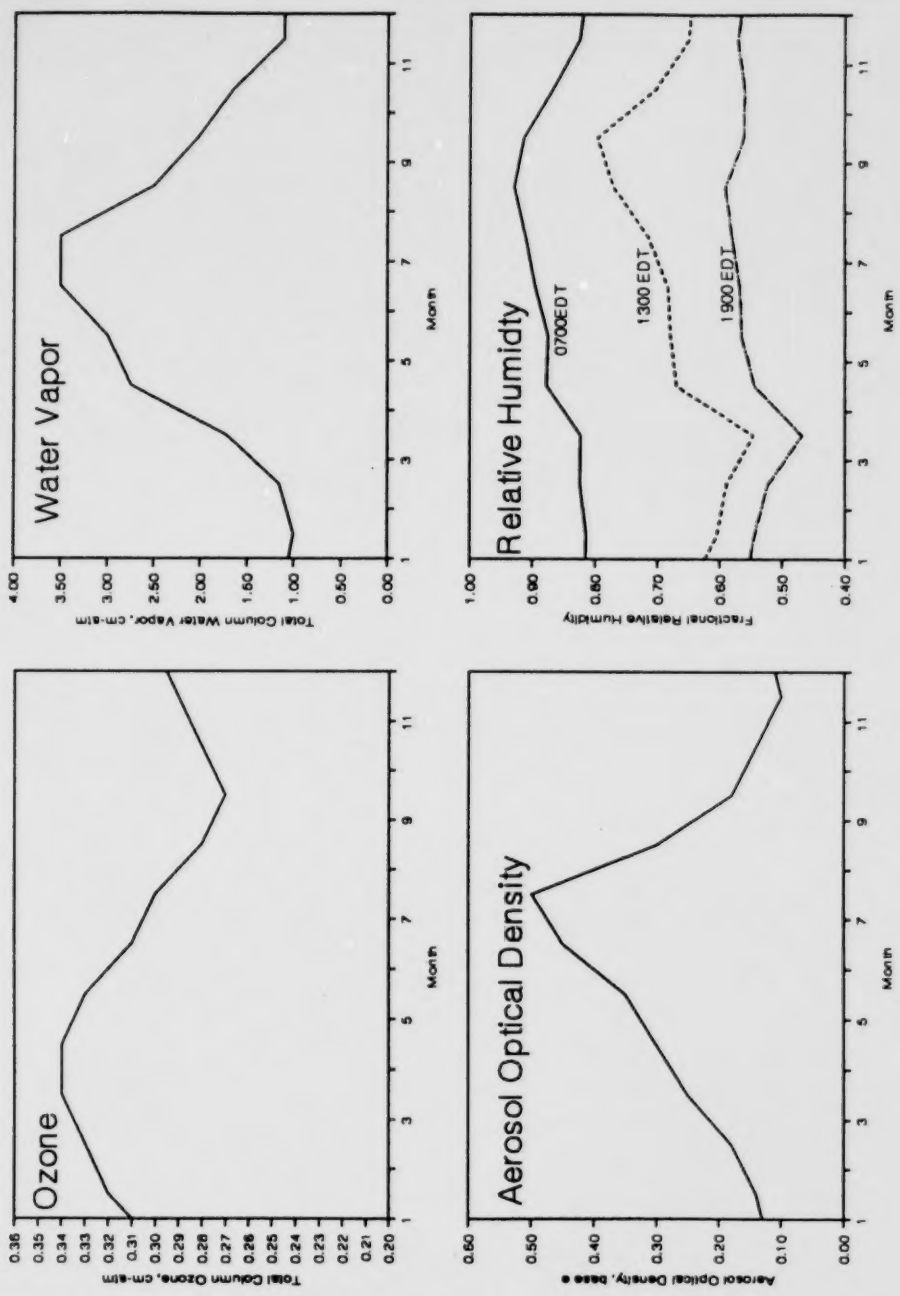

Figure 4. Monthly averaged conditions affecting surface solar radiation for central North Carolina.

In the lower left of Figure 3, the transmissions in the visible and UV region are shown in more detail. Except near the red or longer wavelength end of the spectrum, the total transmission is mostly the result of Rayleigh and aerosol scattering, with some ozone absorption contributing in the 0.5–0.7 $m\mu$ region.

Near the surface, the most important atmospheric photoacceptor species absorb in the UV—below about 420 nm. In the lower right of Figure 3, we can see that the transmission of solar radiation to the surface in the UV region is controlled by three major processes:

- Rayleigh scattering of air molecules;
- aerosol absorption and scattering;
- total column ozone absorption.

The conditions used in the calculation of the transmissions shown in Figure 3 were for a very low turbidity condition such as might occur in October (see Figure 4), and thus in this example, Rayleigh scattering is the dominate attenuation process over most of the UV spectrum. Below 340 nm, however, ozone column absorption becomes more and more important until below 310 nm it is the most attenuating process. Total column ozone absorption *is* the process that determines the lower limit of solar radiation at the earth's surface which is usually considered to be about 295 nm. The total column ozone value selected for this example calculation was approximately the annual average from Figure 4.

The proper application of the model for a particular day requires that input values that are day specific be supplied. The choice of these values will be described below.

The second model is a spectral *spherical* irradiance model using spectral transmission functions as above and which also calculates three components:

- ▷ $\mathcal{N}_\lambda$–the normal beam irradiance which is the same as above;
- ▷ $\widetilde{\mathcal{S}_\lambda}$–the spherical diffuse irradiance which would occur on a spherical surface;
- ▷ $\widetilde{\mathcal{R}_\lambda}$–the spherical irradiance which arises from multiple-reflected radiation between the ground surface and the sky;

and which together constitute the global spherical spectral irradiance,

$$\widetilde{\mathcal{G}_\lambda} = \mathcal{N}_\lambda + \widetilde{\mathcal{S}_\lambda} + \widetilde{\mathcal{R}_\lambda} \tag{2}$$

The spectral "actinic flux," $\mathcal{A}_\lambda$, in units of photons-cm^{-2}-sec^{-1}-nm^{-1} is computed from $\widetilde{\mathcal{G}_\lambda}$, which has units of watt-m^{-2}-nm^{-1} by

$$\mathcal{A}_\lambda = 3.02 \times 10^{13}\, \lambda\, \widetilde{\mathcal{G}_\lambda}$$

Notice that Equation 2 has no explicit dependance on the solar zenith angle, whereas in Equation 1 the normal component is weighted by the cosine of the solar zenith angle.

The transmission functions for spherical diffuse irradiance have a different parameterization than those for a horizontal receiver. It is not possible to calculate $\mathcal{S}_\lambda$ by a cosine weighting of $\widetilde{\mathcal{S}_\lambda}$, which would require assuming a particular hemispherical distribution of the sky radiance. In our model no assumption of isotropic sky conditions is made. These newly derived parameterizations were tested against predictions from complex models such as the Dave[4] and Peterson[2] models. Although these older models have out-of-date representations for aerosol characteristics and used older values for $\mathcal{H}_{0\lambda}$ causing the values predicted by them to not be suitable for our direct use, they can be used to test the functional form of our transmission functions. Figure 5 shows, for four solar zenith angles, the irradiance transmissions computed by the Dave model in the region most affected by total column ozone and the predicted transmissions of the JSMODEL. In performing the tests of the spherical diffuse transmission functions, we first partitioned Peterson's actinic flux into direct and diffuse components using the model formulations given in his computer code, and using his 0% albedo and 5% albdeo actinic fluxes, into multiple reflected components; we then converted these values to transmissions to avoid using the older $\mathcal{H}_{0\lambda}$. It was also necessary to adopt the older aerosol models for the purpose of comparison with the Peterson transmissions. Figure 6 shows, at six solar zenith angles, the diffuse spherical irradiance transmissions computed from the Peterson model and the predicted transmissions of the JSMODEL. The new aerosol models we use are based upon the work of Shettle and Fenn[11] and include the effects of composition, the effects of changing relative humidity, and use a two dimensional parameterization of the backscatter fraction.

To demonstrate the impact that natural variations in aerosols can have on spectral irradiance and the ability of the JSPECTRA and JSMODEL to simulate these conditions, we show spectroradiometer data and model predictions for two days at the UNC site. These were only 15 days apart, but they show essentially the extremes of aerosol conditions. September 15, 1987 was a very hot, extremely hazy day with a "white" sky, more typical of late August. On October 1, 1987, the first cool, Canadian air mass of the year moved rapidly through the U.S. and through N.C., bringing a deep blue sky with no clouds and low total water vapor. The spectroradiometer data and model predictions are shown in Figure 7 and Figure 8. On Sept. 15, the irradiance in the UV portion of the spectrum was 70–90% diffuse, while on Oct, 1, it was only 20–50% diffuse. This difference was almost entirely due to a difference in the aerosol characteristics on the two days.

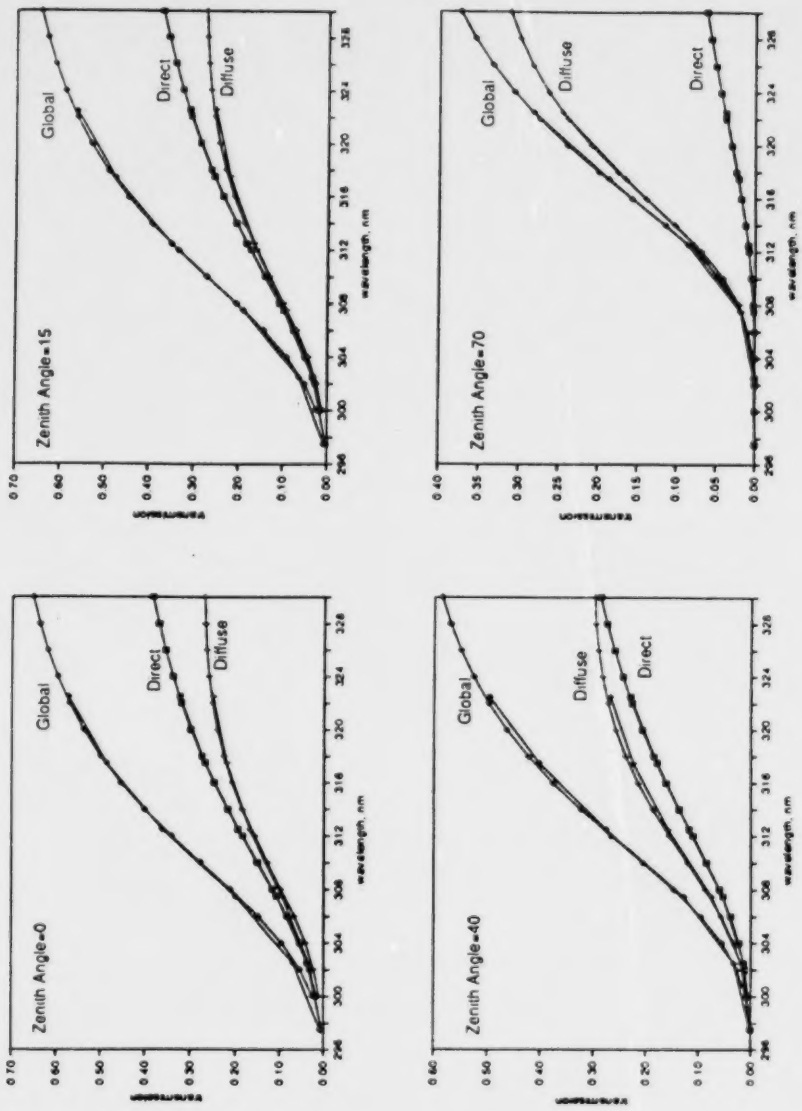

Figure 5. Global, direct, and diffuse irradiances computed by the Dave and Halpern model and by the UNC JSPECTRA model at four solar zenith angles.

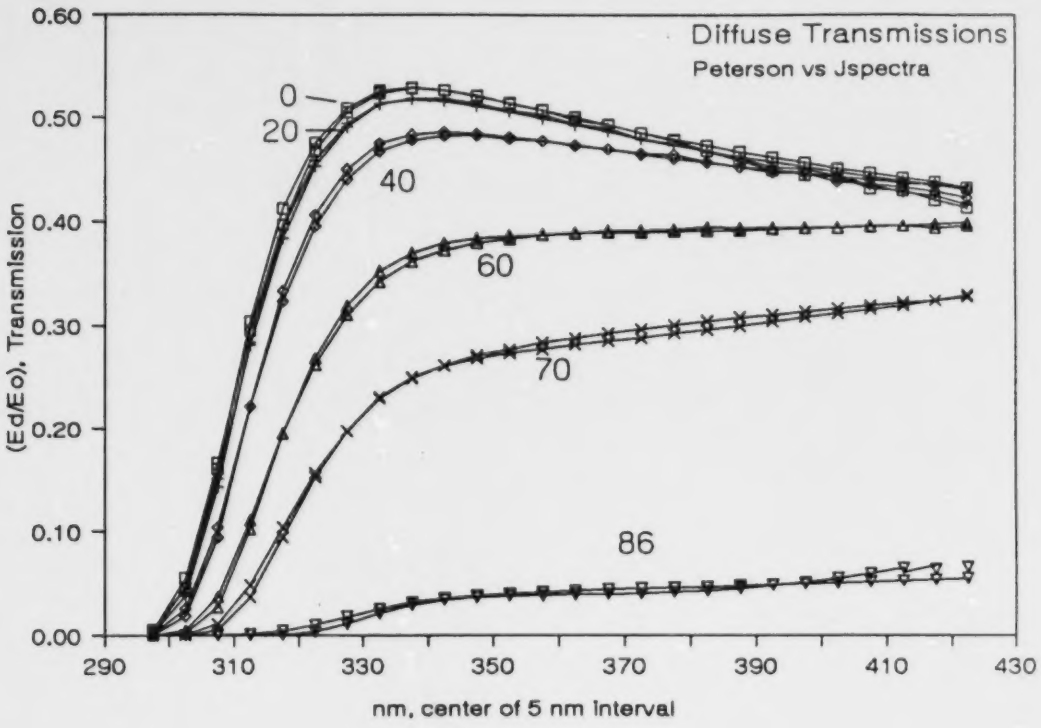

Figure 6. Diffuse spherical transmissions computed by the Peterson model and by the UNC JSPECTRA model at six solar zenith angles.

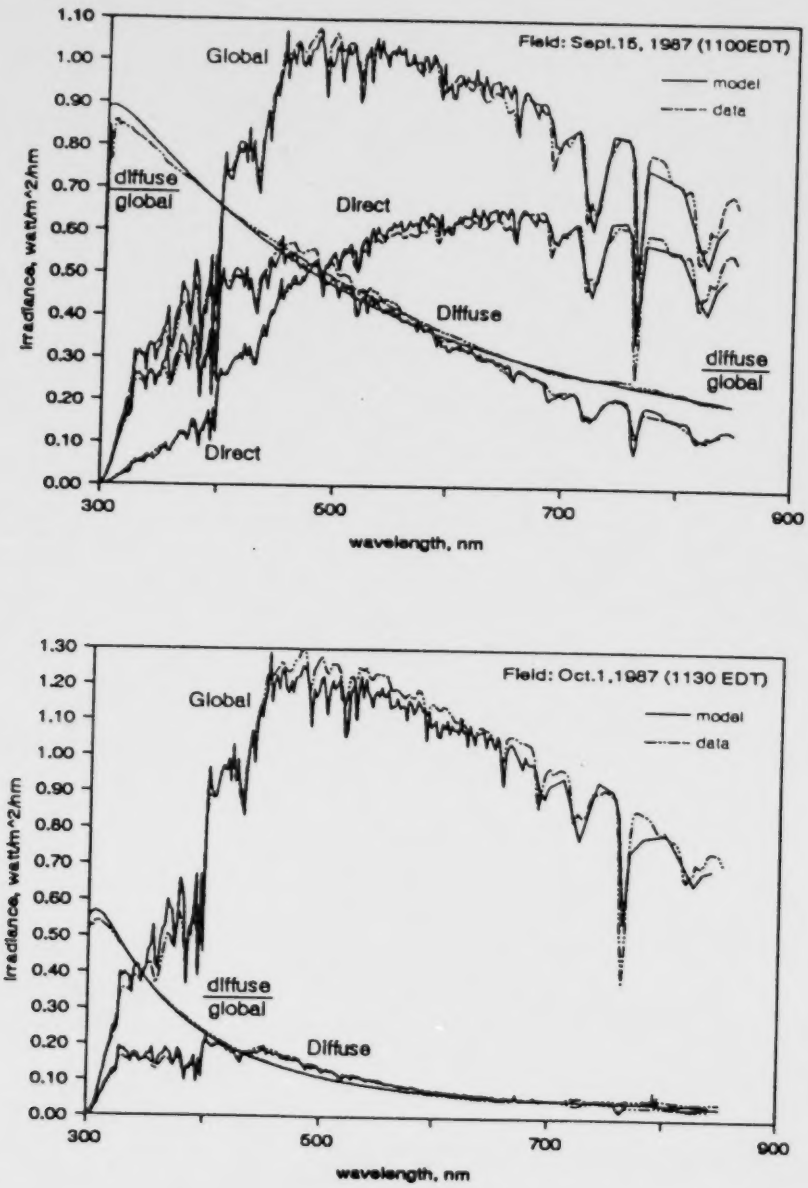

Figure 7. Licor spectroradiometer measured irradiances and JSPECTRA model predictions (2 nm) for two days at the UNC site.

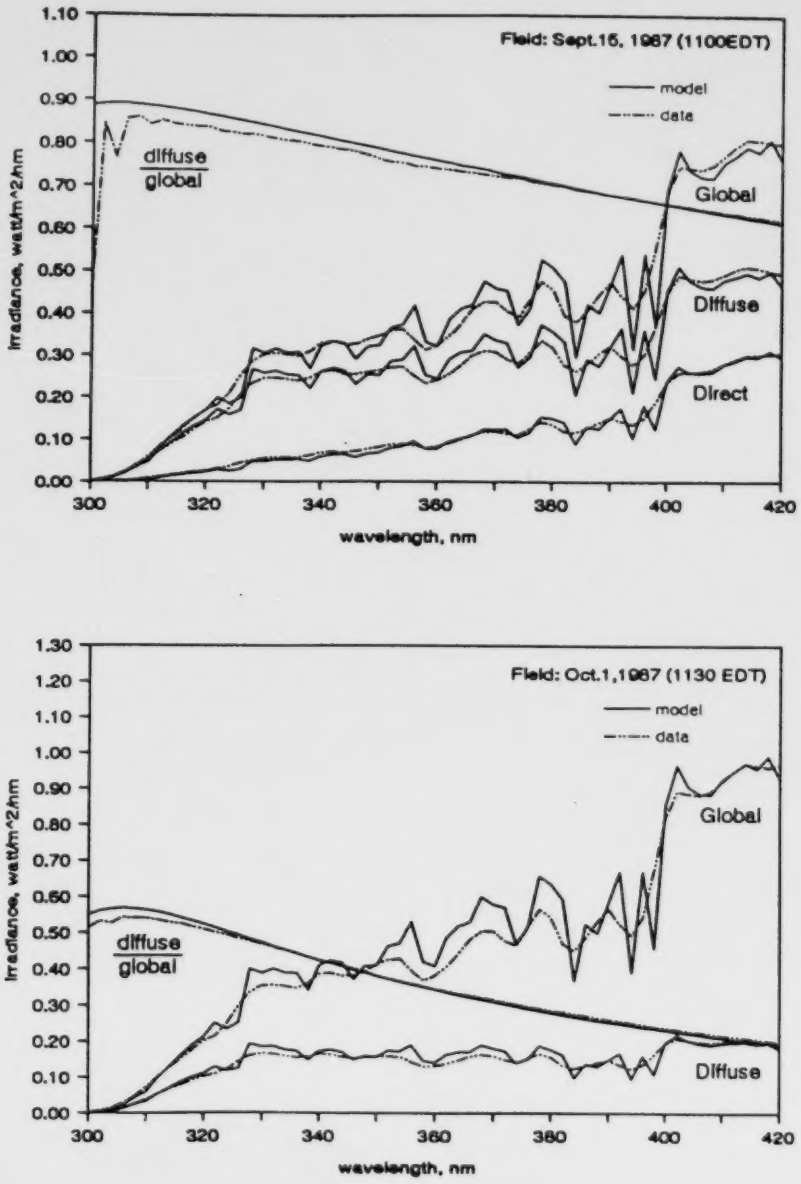

Figure 8. Licor spectroradiometer measured irradiances and JSPECTRA model predictions (2 nm) for two days at the UNC site. Ultraviolet portion of spectrum. Licor slit width is 4 nm, but readings are reported every 2 nm.

The third interdependent model is a broadband (0.3–2.8 $m\mu$) or "total solar" irradiance (TSR) model that of necessity uses a different set of transmission functions for the major scattering and absorbing processes than those in the first two models. These transmission functions, however, are consistent with, and use the same constants and atmospheric parameters as the spectral functions in the first two models. This broadband model also computes three components:

- ▷ $\mathcal{N}$–the normal beam irradiance in the 0.3–2.8 $m\mu$ spectral region;
- ▷ $\mathcal{S}$–the diffuse irradiance on a horizontal surface in the 0.3–2.8 $m\mu$ spectral region;
- ▷ $\mathcal{R}$–the diffuse irradiance on a horizontal surface that arises from the downward component of multiple-reflected radiation between the ground surface and the sky in the 0.3–2.8 $m\mu$ spectral region;

and which together constitute the global broadband TSR irradiance,

$$\mathcal{G} = \mathcal{D} + \mathcal{S} + \mathcal{R} \tag{3}$$

where $\mathcal{D} = \mu\mathcal{N}$ and $\mu = \cos\theta_0$.

The fourth model is a broadband (300-385 nm) ultraviolet irradiance (UV) model that includes the characteristics of the Eppley Laboratory UV radiometer. This radiometer is used at the UNC site to monitor the short wavelength irradiance. The UV model uses yet a different set of transmission functions for the major scattering and absorbing processes than those in the first three models. Like the TSR broadband model, however, the broadband UV transmission functions are consistent with, and use the same constants and atmospheric parameters as the spectral functions in the first three models. This broadband model also computes three components:

- ▷ $\widehat{\mathcal{N}}$–the normal beam irradiance in the 300-385 nm spectral region;
- ▷ $\widehat{\mathcal{S}}$–the diffuse irradiance on a horizontal surface in the 300-385 nm spectral region;
- ▷ $\widehat{\mathcal{R}}$–the diffuse irradiance on a horizontal surface arising from the downward component of multiple-reflected radiation between the ground surface in the 300-385 nm spectral region;

and which together constitute the global broadband UV irradiance,

$$\widehat{\mathcal{G}} = \widehat{\mathcal{D}} + \widehat{\mathcal{S}} + \widehat{\mathcal{R}} \tag{4}$$

where, as above, $\widehat{\mathcal{D}} = \mu\widehat{\mathcal{N}}$.

The major advantage of the broadband TSR and UV models is that they are compact compared to the spectral models and thus are suitable for inclusion into programs such as one that plots observed TSR and UV vs. the broadband model predictions to estimate the local site aerosol and cloud conditions for a given day.

In all these models, the reflected component is dependent upon the other two components and upon the ground albedo and the sky "reflectivity." The form of this dependance is

$$\mathcal{R}_\lambda = \frac{(\mathcal{D}_\lambda + \mathcal{S}_\lambda)\rho_\lambda \rho_{a\lambda}}{1 - \rho_\lambda \rho_{a\lambda}} \tag{5}$$

for irradiance and

$$\widetilde{\mathcal{R}_\lambda} = \frac{2(\mathcal{D}_\lambda + \mathcal{S}_\lambda)(\rho_\lambda + \rho_\lambda \rho_{a\lambda})}{1 - \rho_\lambda \rho_{a\lambda}} \tag{6}$$

for spherical irradiance, where ρ_λ is the spectral albedo of the ground and $\rho_{a\lambda}$ is the reflectivity of the atmosphere for upwelling radiant flux back toward the surface. The value of $\rho_{a\lambda}$ is dependent upon Rayleigh scattering, aerosol characteristic, and other gas absorption. Thus the computation of $\mathcal{R}_\lambda$ or $\widetilde{\mathcal{R}_\lambda}$ is trivial after $\rho_{a\lambda}$ has been calculated. Therefore, the real third component calculated by all four models is $\rho_{a\lambda}$ for the spectral model and ρ_a for the broadband models.

For the ground albedo in the spectral models, we used the same values as Peterson[3]. These were:

λ, nm	280	380	400	430	500	700	780	4000
albedo	0.05	0.05	0.06	0.08	0.10	0.08	0.25	0.25

and for the TSR and UV broadband albedos we used 0.20 and 0.05.

Inputs Needed For the Calculation of Actinic Flux

The day specific data that are available to run the models are:

- ▷ 4-minute values of Eppley UV and Eppley TSR radiometer readings;
- ▷ interpolated total atmospheric column ozone data from the World Ozone Sounding Network;
- ▷ general meteorological data from the Raleigh-Durham weather station.

The Eppley UV and TSR radiometer data are included in the SegFiles for the 281 fully processed experiments in the dual outdoor smog chamber. The remaining day specific data have been abstracted into a data base called SOLCLIM. SOLCLIM has one row for every run in the SegFile data set, in chronological order. A printout of selected columns of this data base are included as Appendix A.

Each row in SOLCLIM contains:

- run directory and date-based SegFile name (columns A, B, C) and the run date in various forms (columns D, E, F, G; these and other columns are hidden in the printout);
- a section of flags indicating if a run had been modeled by UCR/ERT (column H), modeled by SAI (column I), and whether the data file contains UV radiation measurements (column J) (and all three columns are hidden in the printout);
- a column (K) giving the time correction to add to the sometimes inaccurate clock times reported in the data files;
- a section with climatological data which includes:
  - ▷ atmospheric pressure (column L),
  - ▷ total ozone column (column M),
  - ▷ total water vapor column (column N),
  - ▷ a code number for one of three "lower" aerosol models (*i.e.*, special, rural, or urban models) (column O),
  - ▷ the "upper" or stratospheric aerosol optical density at 500 nm (column P),
  - ▷ the "lower" or surface aerosol optical density at 500 nm (column Q),
  - ▷ the "lower" aerosol single scattering albedo (column R),
  - ▷ ambient relative humidities at 0700, 1000, 1300, 1600 EDT) (columns T, U, V, W);

- five sets of ending times and interval averaged broadband transmissions for TSR and UV radiation (columns X to AL); these data will be described in more detail below ;
- a section on solar coordinates and times of events (in the second printout) which includes:
  - ▷ the run date (column AP),
  - ▷ solar declination in degrees (column AQ),
  - ▷ the correction, in minutes, to the mean sun time from the equation of time (column AR),
  - ▷ the relative earth-sun radius (column AS),
  - ▷ the UNC site EDT time of civilian twilight in hours (column AT),
  - ▷ the UNC site EDT time of sun rise, noon, and sun set in hours (columns AU, AV, AW); and
  - ▷ the UNC site EDT time of sun rise and noon in hours and minutes (columns AX and AY).

The sections from column O to column W are inputs to the aerosol model AEROMOD which produces the optical density for aerosol scattering and absorption as a function of wavelength for both the JSMODEL and BBMODEL.

A second printout listing solar conditions (*e.g.*, declination, equation of time, and relative earth orbit radius) and times of solar events (*e.g.*, twilight, sunrise, noon, and sunset) for each of the SegFiles is also included in Appendix A. Our programs use the SOLCALC module to compute the solar related information shown in this table, and the table is therefore included just for the reader's information.

Steps in the Calculation of Actinic Flux

The general strategy for calculating the in-chamber actinic flux is to first calculate the irradiance components outside the chamber (*i.e.*, the ambient direct beam, diffuse, and multiple reflection irradiance) taking into account the local meteorological conditions, and then to transform these irradiance components to inside chamber values using film transmissions, chamber geometry, and floor and wall reflectivities.

The actual computations occur in several stages:

1) use the BBMODEL with SOLCLIM inputs to predict TSR and UV radiometer data, and confirm the conditions given in SOLCLIM by demonstrating good agreement between model and data using plots for each day (these are both high resolution color graphics screen plots and laser printer hardcopy plots);
2) calculate the ratio of the integral of BBMODEL predictions and TSR and UV radiometer data over five variable-width intervals that are about 3 hours each; the actual interval widths are selected for the specific cloud conditions on each day; the calculated ratios, which for clear days should be near 1.00, are used to correct subsequent model predictions for cloud effects; tabulate the time intervals and the ratios in columns X to AL of SOLCLIM data base;
3) re-calculate the TSR and UV model predictions in step 1, using the "cloud" transmissions (ratios) calculated in step 2 to verify the quality of fits for each day using both screen and hard copy plots;
4) use the JSMODEL and the inputs from SOLCLIM (including the "cloud" transmissions calculated in step 2) to compute the irradiance and spherical irradiance components outside the chamber at 16 minute intervals; use CHMMODEL to compute the spectral transmission of the chamber walls for the solar zenith and azimuth angles at each 16 minute time; compute the in-chamber global irradiance from the outside irradiance components and the chamber transmissions, and using the chamber floor and wall reflectivity, compute the multiple reflection component for inside the chamber; compute the in-chamber direct beam and spherical diffuse component from outside values and the chamber transmissions; compute the in-chamber global spectral spherical irradiance (actinic flux) as the sum of all the components; store the actinic flux values in a file for each day;
5) using input tables of absorption cross-sections and quantum yields for each photolytic reaction and the files of actinic flux on 16 minute intervals for each day, compute the photolysis rates of the reactions and store in a file for each day; document the calculated photolysis rates for NO_2 and HCHO by plotting the observed UV radiometer and calculated photolysis rates for each day.

Daily Atmospheric Conditions

Clear Model

To estimate the daily atmospheric conditions needed to adjust the calculated fluxes for cloudy conditions, we first modeled the observed UV and observed TSR profiles for all 281 days from 1977 to 1986 in the UNC SegFile dataset using the broadband versions of the models described above and "cloudless" conditions. This program was called SEGBBMOD. The model inputs, listed in the SOLCLIM data base, were mostly based upon the Raleigh-Durham weather station climatological data. Daily averaged values of total column ozone and total column water vapor for this region were taken from Iqbal.[5] At first, daily values of averaged aerosol optical densities at 500 nm (the turbidity) were estimated from Peterson and Flowers[12] 8-year, least-squares fit to measurements at Raleigh. Later, in several cycles of revisions, these values were up-dated within the range of values reported by Peterson and Flowers to improve the model predictions for each day. The stratospheric aerosol optical density[13] was constant within a year, but was larger in 1982 and decayed thereafter to approximate the effect of volcanic ash injected by large eruptions in 1982. Linear interpolation between the four values of relative humidity in SOLCLIM was used to estimate relative humidities at intermediate local times for each day modeled.

A few example plots of the "clear"-BBMODEL TSR and UV predictions vs. SegFile radiometer data are given in Appendix B, Part I.

Cloudy Model

Clouds can have two effects on irradiance received at the earth's surface: if the cloud blocks the direct beam, the irradiance is *reduced* over totally clear sky conditions, but if cumulus clouds occupy the sky opposite the sun's location, the irradiance is *increased* over the totally clear sky condition. This is caused by the cloud reflecting more radiation back than the clear sky and thus raising the diffuse radiation at the surface. Of course, the exact amount of increase or decrease is a complex function of the cloud type and location and it is certainly not possible to calculate directly these effects for our SegFile data set. Instead of a direct calculation we will approximate the effects by calculating "cloud correction factors" to be applied to the BBMODEL and, later, the JSMODEL predictions.

The solution methods for solving differential equations arising from chemistry use past history of the solution to predict the values at the next time step; these initial estimates are then corrected until some error tolerance is achieved. Such methods do not perform well when input parameters to the system are suddenly

changed: then the prediction fails and the method must fall back to using very small time steps. The time profiles for major species in the chamber are essentially smooth even when the sunlight is changing very rapidly as with clouds. From an examination of our experimental results, it appears that clouds which block the sun need to do so for more than one-half hour to cause an obvious change in the time profile slope for a species in the chamber. The need to minimize the frequency of abrupt change and the tendency of the real chemical system to "smooth" changes suggests that we do not have to follow the fine structure in cloud effects in our cloudy model. Based on these considerations, we modified the program SEGBBMOD (which was "cloudless") to calculate the integral of the BBMODEL predictions and the integral of the SegFile TSR and UV radiometer measurements over a sequence of 3-hour time intervals. We then formed the ratio of the model predicted integrals and the data integrals. That is,

$$\tau_c(t_2) = \frac{\int_{t_1}^{t_2} \mathcal{G}\, dt}{\int_{t_1}^{t_2} \mathsf{TSR}\, dt} \quad \text{and} \quad \widehat{\tau_c}(t_2) = \frac{\int_{t_1}^{t_2} \widehat{\mathcal{G}}\, dt}{\int_{t_1}^{t_2} \mathsf{UV}\, dt}$$

where in this case, TSR and UV represent the readings from the tower radiometers and are the values reported in the SegFiles. The values t_2, τ_c, and $\widehat{\tau_c}$ were written to a file with a line for each SegFile. This program was called SEGINTMOD. Initially SEGINTMOD was run with the first t_1 being sunrise and t_2 = 0900 EDT, then t_1 = 0900 EDT and t_2 = 1200 EDT, and so forth every 3 hours. Then SEGBBMOD was modified to read the sets of t_2, τ_c, and $\widehat{\tau_c}$ for each day and use them to "correct" the model predictions. A new set of plots for the model and data were produced and upon examination, the values of t_2 in all the intervals for a day were adjusted if needed to more closely align the model integral intervals with the time of onset of clouds. Then the program SEGINTMOD was run again with the new times to produced new τ_c and $\widehat{\tau_c}$ values, which were in turn used by SEGBBMOD to make new plots of the model predictions and the observed data. Three such cycles were needed before the times were considered satisfactory. The final values of the five sets of

$$t_2, \quad \tau_c, \quad \widehat{\tau_c}$$

are included in the SOLCLIM data base in columns X to AL in the listings in Appendix A.

Because these fits are the basis of the later calculation of photolysis rates, all the plots of the "cloudy" version of SEGBBMOD TSR and UV predictions vs. SegFile radiometer data are given in Appendix B, Part II. In addition, this plot set allows a modeler to assess the relative quality of sunlight for a particular day in contrast to another day and thus is a data resource independent of the quality of the SEGBBMOD fits.

Although we have spectral transmission data for clouds which will allow the conversion of the broadband transmissions estimated from the UV radiometer and model ratios into spectral transmissions, we are not including this refinement at this time. The cloud spectral transmissions are reasonably flat for broadband transmissions greater than 0.6 (*e.g.*, a 40% depletion in clear sky values) and so the use of spectral transmissions would be effective only in those cases of moderate to heavy cloud cover. These situations are likely to be poorly modeled by the chemical kinetics modules even if we used spectral transmission functions.

Discussion of Step Four: the Calculation of In-chamber Irradiances

We have demonstrated that we can calculate the broad band quantities,

$$\mathcal{D}, \quad \mathcal{S}, \quad ,\mathcal{R}, \quad \text{and} \quad \mathcal{G}$$

and

$$\hat{\mathcal{D}}, \quad \hat{\mathcal{S}}, \quad ,\hat{\mathcal{R}}, \quad \text{and} \quad \hat{\mathcal{G}}$$

as well as estimate the effects of clouds using site radiometer data to compute τ_c and $\hat{\tau}_c$. We can also calculate the spectral quantities

$$\mathcal{N}_\lambda, \quad \mathcal{S}_\lambda, \quad ,\mathcal{R}_\lambda, \quad \text{and} \quad \mathcal{G}_\lambda$$

and, as shown in Figure 6, we can compute $\widetilde{\mathcal{S}_\lambda}$ as good as Peterson's tablulated values. Likewise our computed values of $\widetilde{\mathcal{R}_\lambda}$ show excellent agreement with the difference between Peterson's tabulated values for 0% albedo and 5% albedo. The computation of $\widetilde{\mathcal{G}_\lambda}$ is a simple sum, $\mathcal{N}_\lambda + \widetilde{\mathcal{S}_\lambda} + \widetilde{\mathcal{R}_\lambda}$, from which values of $\mathcal{A}_\lambda$ are calculated by a change of units.

Now we discuss the process for calculating the in-chamber irradiance values. Figure 9 is a schematic of the chamber to illustrate some of the factors involved in calculating the in-chamber flux.

Theoretically, the 'outside' components should pass through the Teflon film and become 'inside' components, perhaps attenuated somewhat by the film. 'Inside' chamber values will be shown in brackets, for example,

$$\text{inside normal beam} = \text{film trans.} \times \text{outside normal beam}$$
$$\langle \mathcal{N}_\lambda \rangle = \tau_{f D_\lambda} \mathcal{N}_\lambda$$

where $\tau_{f D_\lambda}$ is the spectral film transmission for the direct beam component and $\tau_{f S_\lambda}$ will be used for the diffuse component.

The calculation of the in-chamber irradiances is therefore

$$\langle \mathcal{N}_\lambda \rangle = \tau_{f D_\lambda} \mathcal{N}_\lambda$$
$$\langle \mathcal{D}_\lambda \rangle = \mu \langle \mathcal{N}_\lambda \rangle$$
$$\langle \mathcal{S}_\lambda \rangle = \tau_{f S_\lambda} (\mathcal{S}_\lambda + \mathcal{R}_\lambda)$$
$$\left\langle \widetilde{\mathcal{S}_\lambda} \right\rangle = \tau_{f S_\lambda} (\widetilde{\mathcal{S}_\lambda} + \mathcal{R}_\lambda).$$

The in-chamber diffuse components are the result of both the outside diffuse component and the *downward* component of the outside reflective component, therefore

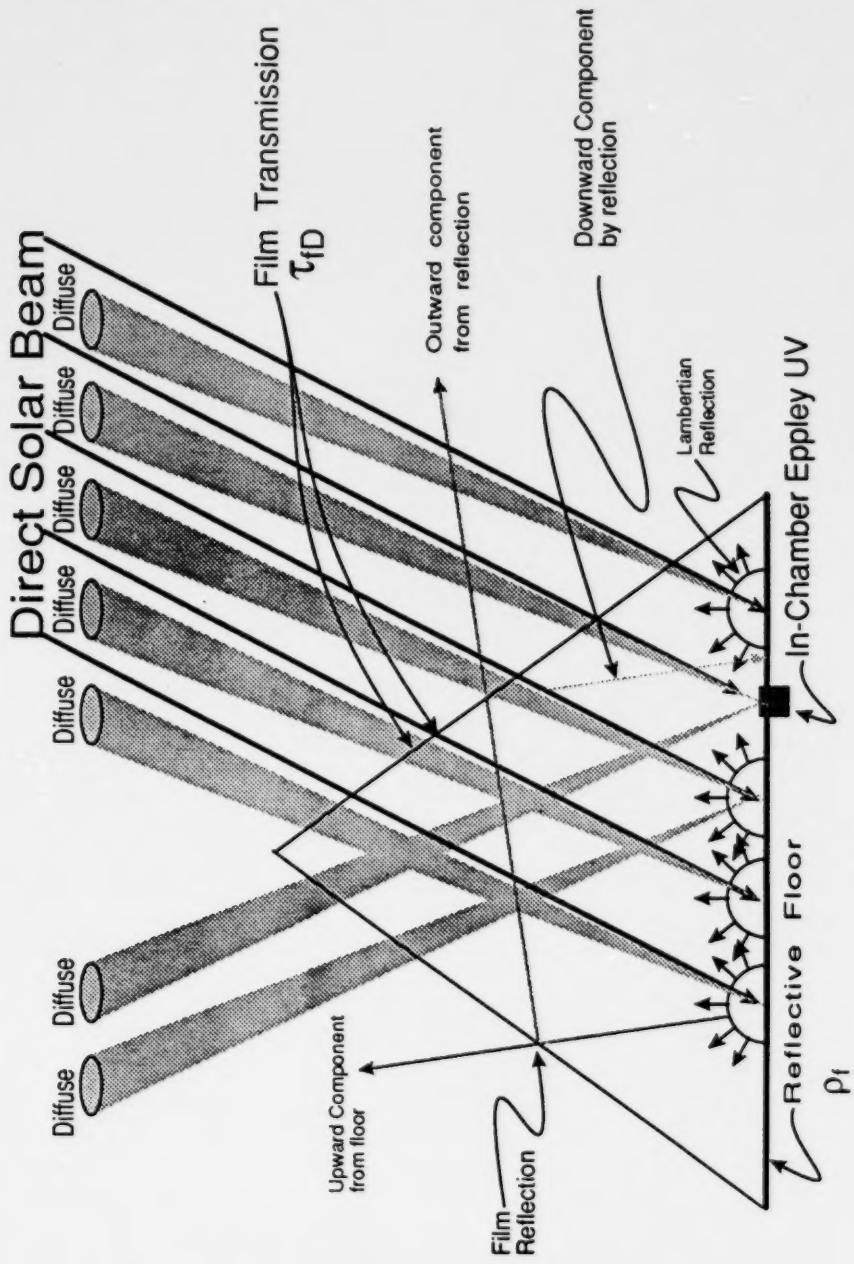

Figure 9. Schematic showing factors affecting in- chamber radiant flux.

$\mathcal{R}_\lambda$ is used even for the calculation of $\widetilde{\mathcal{S}}_\lambda$. The in-chamber multi-reflected irradiance from the chamber floor upward and from the chamber walls back down for both a horizontal and spherical receiving surface, is[5,3]

$$\langle \mathcal{R}_\lambda \rangle = \frac{(\langle \mathcal{D}_\lambda \rangle + \langle \mathcal{S}_\lambda \rangle) \left\langle \rho_{f\lambda} \rho_{w\lambda} \right\rangle}{1 - \left\langle \rho_{f\lambda} \rho_{w\lambda} \right\rangle}$$

$$\left\langle \widetilde{\mathcal{R}_\lambda} \right\rangle = \frac{2(\langle \mathcal{D}_\lambda \rangle + \langle \mathcal{S}_\lambda \rangle)(\left\langle \rho_{f\lambda} \right\rangle + \left\langle \rho_{f\lambda} \rho_{w\lambda} \right\rangle)}{1 - \left\langle \rho_{f\lambda} \rho_{w\lambda} \right\rangle}$$

where $\left\langle \rho_{f\lambda} \right\rangle$ and $\langle \rho_{w\lambda} \rangle$ are the chamber floor and chamber wall reflectivities. The spherical surface not only sees the downward reflective flux, it sees the upward flux also. Finally, the global spectral spherical radiant flux density is

$$\left\langle \widetilde{\mathcal{G}_\lambda} \right\rangle = \langle \mathcal{N}_\lambda \rangle + \left\langle \widetilde{\mathcal{S}_\lambda} \right\rangle + \left\langle \widetilde{\mathcal{R}_\lambda} \right\rangle$$

and the "actinic flux" in the chamber is

$$\langle \mathcal{A}_\lambda \rangle = 3.02 \times 10^{13} \lambda \left\langle \widetilde{\mathcal{G}_\lambda} \right\rangle .$$

The "missing pieces" in this process are, therefore, the chamber transmissions,

$$\tau_{fD_\lambda} \quad \text{and} \quad \tau_{fS_\lambda},$$

and the chamber floor and wall reflectivities,

$$\left\langle \rho_{f\lambda} \right\rangle \quad \text{and} \quad \langle \rho_{w\lambda} \rangle .$$

Our first approximation, based upon initial comparison of in-chamber and tower UV radiometer readings, was that the film transmission was constant at about 0.68. Our first attempt at spectral measurements, however, revealed that beam incidence angle was critical in determining how much light was transmitted through the film. Thus we had to undertake the development of a Teflon Film Transmission Model, TFTM. This will be described in its own section below. While the TFTM will describe the optics of a single sheet of Teflon, the chamber volume is often illuminated through three different Teflon faces, each with a different orientation to the sun. Because the air inside the chamber is stirred, both by mixing fans as well as thermal motion, it experiences radiation through all film faces. Therefore, we must use the chamber geometry and the TFTM to calculate an "average" transmission. This will be described in another section below.

If the diffuse components in the radiant fluxes is viewed as a "field of direct beams," then the process described above for the direct beam components could logically be applied to the diffuse components as well. Because τ_{fD} differs with different beam incident angles, the *distribution* of the diffuse field might be important, and therefore, there might be a different value for the film diffuse transmission, τ_{fS} than for τ_{fD}. Special in-chamber measurements were needed to evaluate this condition and these will be described below as well.

To calculate the reflective component in the chamber, the reflectivity (*i.e.*, spectral albedo) of the floor and chamber walls must be characterized. These results also will be presented along with the chamber characteristics below.

FEP Teflon Film Transmission Model

The Teflon Film Transmission Model (TFTM) is based on measurements we performed using a special apparatus we constructed which uses solar radiation as the light source, new or used film, and both broadband and spectral sensors to accurately determine broadband and spectral film transmission as a function of radiation beam incidence angle.

In creating the TFTM, we made several assumptions. First, we assumed that all light that impinges on the film is either transmitted through the film, τ_f, absorbed by the film, a_f, or reflected from the surface, r_f. Therefore,

$$1 = \tau_f + a_f + r_f$$

Second, we assumed that when the angle between the light beam and the normal to the film plane, ϑ (analogous to the solar zenith angle), is zero, then reflection would be zero, *i.e.*, $r_f = 0$. Therefore,

$$a_f = 1 - \tau_f \quad \text{when} \quad \vartheta = 0$$

Third, we assumed that absorption in the film, a_r, is independent of ϑ. Therefore,

$$r_f = (1 - a_f) - \tau_f \quad \text{when} \quad \vartheta > 0$$

Thus, a_f was determined from measured τ_f when $\vartheta = 0$ and r_f was determined from measured τ_f and calculated a_f when $\vartheta > 0$. In actual practice, we found that a_f does vary slightly with the incidence angle and a parameterization to account for the effect was found using τ_f at several ϑ values.

Let

ℓ_o be a reference wavelength beyond the visible spectrum;

ν be $\cos\vartheta$, which is 1 when the solar beam is normal to the film;

$\tau_f(1;\ell_o)$ be the film transmission when the solar beam is normal to the film ($\nu = 1$) and at the reference wavelength;

λ be the wavelength at which the transmission is desired;

$\tau_f(\nu;\lambda)$ be the film transmission at an incident angle $\cos^{-1}\nu$ and at wavelength λ

α_o be a wavelength variation factor;

λ_o be a wavelength offset factor;

n_o, n_1, n_2 be constants.

The film transmission model is

$$\tau_f(1;\lambda) = \tau_f(1;\ell_o) - \exp[-\alpha_o(\lambda - \lambda_o)]$$
$$\tau_f(\nu;\ell_o) = \left[2\tau_f(1;\ell_o)^2\nu - \tau_f(1;\ell_o)^2\nu^2\right]^{1/2}$$
$$\alpha = n_o + n_1\nu + n_2\nu^2$$
$$\tau_f(\nu;\lambda) = \tau_f(\nu;\ell_o) - \exp[-\alpha(\lambda - \lambda_o)]$$
$$r_f(\nu;\lambda) = \tau_f(1;\lambda) - \tau_f(\nu;\lambda)$$

The exponential term in the first equation describes the effect of the change in film absorption, a_f, as a function of wavelength for a light beam normal to the film: absorption increases (and transmission decreases) as the wavelength decreases from 900 nm to 300 nm. The second equation describes the change in film transmission as a function of incidence angle at the reference wavelength, ℓ_o: reflection from the surface of the film results in a decrease in film transmission as the angle between the beam and the film normal increases. The transmission as a function of incidence angle at a fixed wavelength was accurately described by an elliptical function. The third equation describes the effect of changes in a_f as a function of beam incidence angle. The fourth equation describes the film transmission as a function of wavelength at a particular incidence angle. The last equation describes the reflection as a function of wavelength and incidence angle; because the two terms have similar wavelength dependencies, reflection is essentially only dependent upon the incidence angle and not the wavelength.

The values of the parameters of the model are:

ℓ_o = 900 nm
λ_o = 110 nm
$\tau_f(1;\ell_o)$ = 0.895
α_o = 0.008563
n_o = 0.010538
n_1 = -0.00685
n_2 = 0.004875

Also note that $\alpha_o = n_o + n_1 + n_2$.

The accuracy of this model is shown in Figure 10 which shows both the measured transmission and model predictions.

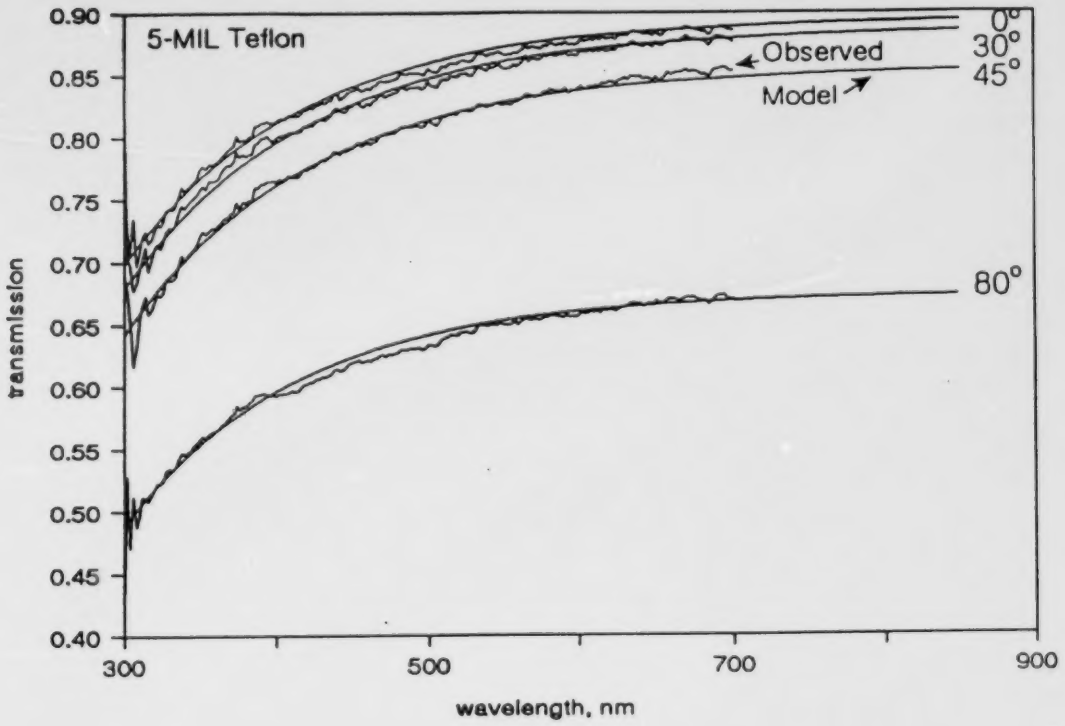

Figure 10. Teflon Film Transmission Model predictions and film transmission measured with the SMUTT apparatus and the Licor 1800 spectroradiometer. The "Observed" lines are the ratio of the 6° view solar spectrum without and with 5-mil Teflon film at the indicated incidence angle (angle between a normal to the film plane and the sun).

UNC Chamber Characteristics

As shown in Figure 11, the UNC Chamber has five major Teflon film surfaces identified as: Blue End, Field Side, Red End, Lab Side, and Floor. Table 1 gives the orientation (zenith angle and azimuth of the normal) of each film surface, and the areas of each chamber face.

Table 1. Physical Characteristics of UNC Chamber.

Item	Value	Units
Face Azimuth		
Blue End	153	degrees
Field Side	63	degrees
Red End	-27	degrees
Lab Side	-117	degrees
Face Tilt		
Blue End	90.0	degrees
Field Side	52.7	degrees
Red End	90.0	degrees
Lab Side	52.7	degrees
Face Area		
Blue End	23.50	m^2
Field Side	102.84	m^2
Red End	23.50	m^2
Lab Side	102.84	m^2

The vertical side members of the chamber are called rafters and the horizontal side members are called perloins. The sides consists of sheets of film, attached *inside* adjacent rafters, and beginning on the floor of the Field Side and continuing over the top of the chamber and down to the floor on the Lab Side. These sheets are *not* attached to the perloins. The Floor and Ends are each one heat-sealed piece of Teflon. For the purposes of discussion, the side panels of the chamber are designated with numbers for areas between rafters and with letters for areas between perloins, therefore, panel B2 is between the second and third rafter and the first and second perloin on the RED chamber half. This designation will be useful in subsequent discussion of in-chamber irradiance.

To the west of the chamber is the sampling laboratory. Near the west end of the laboratory is a 7 meter radiometer tower with a cross on the top to hold the TSR and UV radiometers. The top of the tower is higher than the top of the chamber. Directly under the third perloin on the Field Side of the RED chamber, mounted in the floor, is an Eppley UV radiometer. This is labeled UV in Figure 13.

When the chamber was built, the floor was first covered in aluminum foil, dull side up, and then this was overlaid with one heat-sealed piece of 5-mil Teflon. The aluminum floor was added to reduce the heat absorption of the chamber floor by reflecting infrared radiation back through the transparent chamber walls. This reduced the floor temperature and thus the air temperature in the chamber. The floor, of course, also effects other wavelengths of radiation and partially compensates for the transmission losses through the chamber walls. To understand the effect of the aluminum floor on the radiant flux in the chamber, we conducted a number of experiments with the spectroradiometer both on the chamber floor and in a support webbing at 2 meters above the floor from which the spectroradiometer could look down at most of the floor of the RED chamber. Figure 12 shows, on the top, one example of the measurement of the spectral reflectivity of the chamber floor. On the bottom of Figure 12, the effects of the wall back-reflectivity are shown. The mean of several measurements of the chamber floor reflectivity is given in the first column of Table 2; the second column gives values of the wall back-reflectivity based on October 1, 1988 measurements. Other days have similar values *e.g.*, ± 0.02. Those spectra taken with the black floor have $\rho\rho_w$ values that are low *i.e.*, 0.010–0.058, between 300–850 nm.

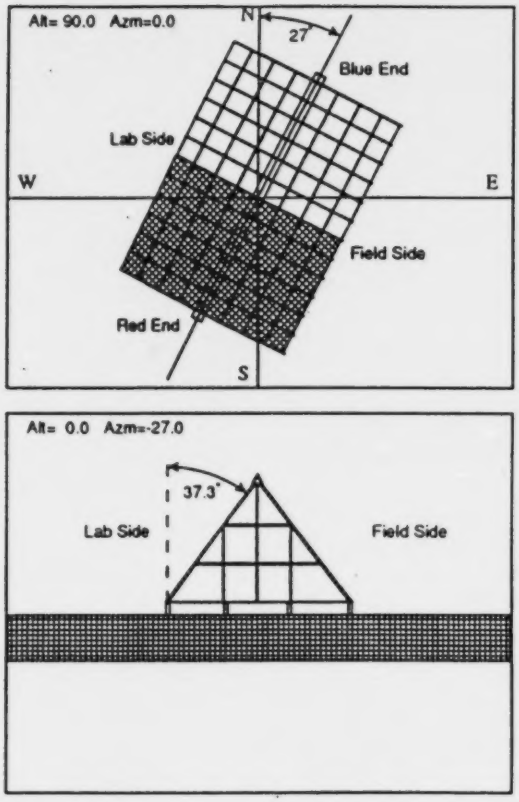

Figure 11. Design of the UNC Dual Outdoor Smog Chamber. Top: direct overhead view; ridge line is at 27° heading, shaded floor is in Red chamber half. Bottom: end view looking along ridgeline from Red End.

Table 2. Chamber Floor and Walls Reflectivity.

λ, nm	ρ_f	$\rho\rho_w$
300	0.570	0.048
380	0.593	0.060
400	0.599	0.072
430	0.607	0.096
500	0.624	0.100
550	0.674	0.100
700	0.698	0.101
780	0.686	0.101
850	0.686	0.102
2000	0.700	0.120

ρ_f is floor reflectivity,
$\rho\rho_w$ is wall back reflectivity.

The UNC Chamber Transmission Model

The UNC Chamber Transmission Model (CTM) seeks to apply the Teflon Film Transmission Model to the chamber film surfaces and to combine the calculated transmissions in a manner that approximates the net effect of the film on the in-chamber flux for a given solar zenith angle and azimuth.

Figure 13 shows four views of the chamber on April 20, 1988. Data from this day will be discussed in detail in a subsequent section. Here we wish to illustrate that the number and orientation of the directly visible faces changes in a predictable manner throughout a day. (Although Figure 13 is for April 20 and September 1 is used as the example in this section, the solar azimuth and altitude on these two days is nearly identically because the solar declination is nearly identical; however, the sun is moving up in the sky each day in April and is moving down in the sky each day in September). Viewed from the sun, the chamber appears to rotate counterclockwise throughout the day.

The first operation in CTM is to compute the solar beam incidence angle on each of the chamber film surfaces by

$$\mu_f = \cos\beta_f \cos\theta_0 + \sin\beta_f \sin\theta_0 \cos(\psi_0 - \psi_f)$$
$$\theta_f = \cos^{-1}\mu_f$$

where

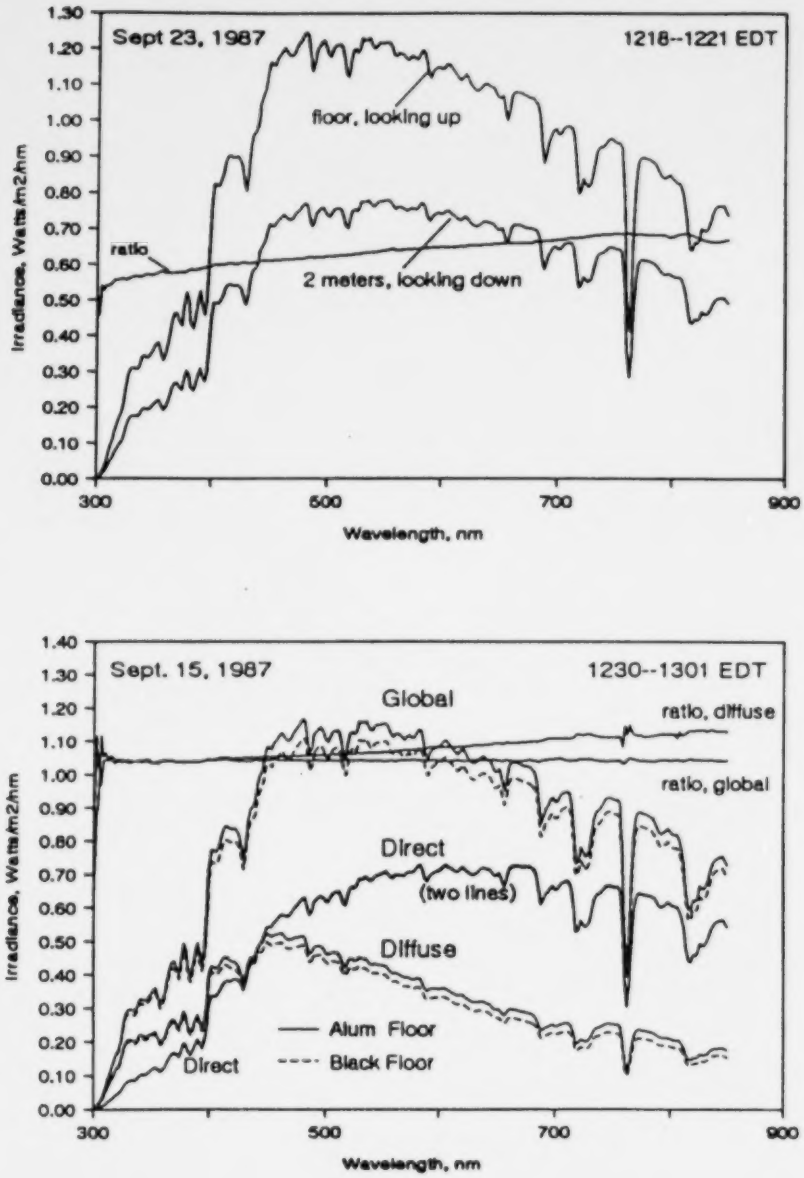

Figure 12. Top: Licor spectroradiometer spectra in UNC Chamber looking-up and looking-down and the ratio. Bottom: Licor spectroradiometer spectra in UNC Chamber with normal aluminum floor and with black plastic floor and the ratio.

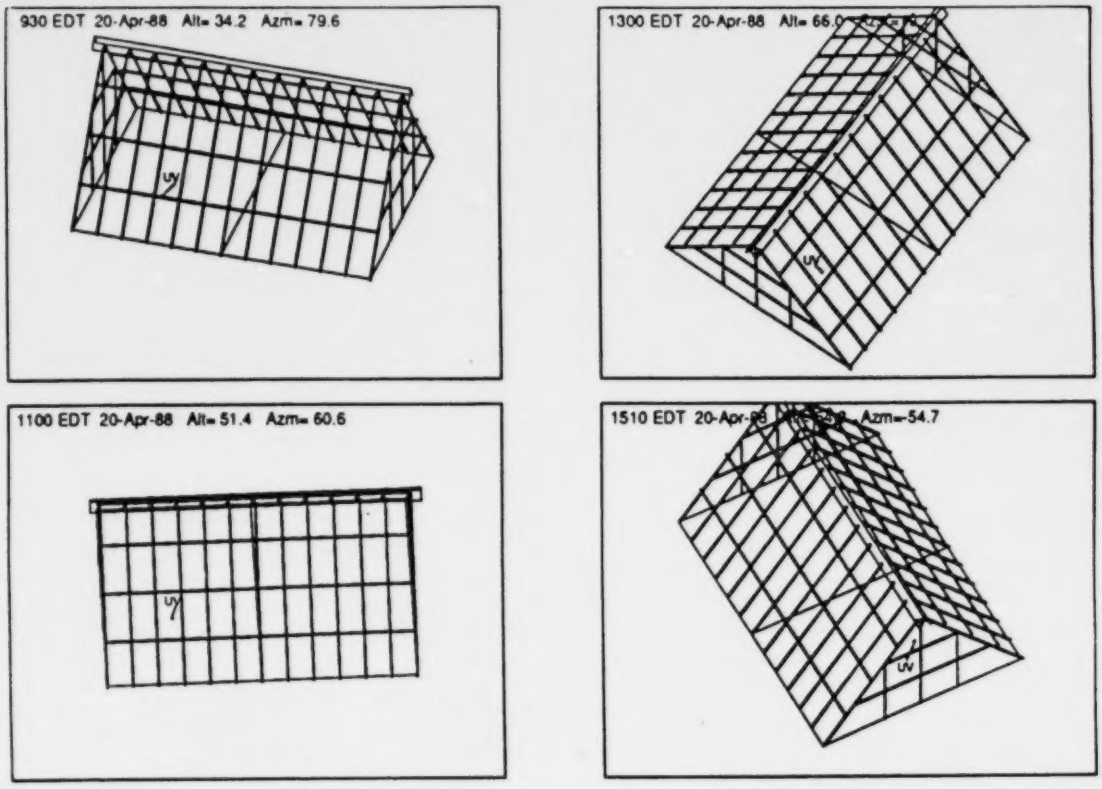

Figure 13. Four views of the UNC dual outdoor chamber on 20-Apr-1988. The viewpoint is on a line between the in-chamber Eppley radiometer position on the chamber floor (shown by a dot) and the sun. The viewing distance is 3500 meters from the chamber, but the view has been magnified by 150. The time, solar altitude, and azimuth are given at the top of each view.

β_f —film tilt angle, angle between film normal and zenith;

ψ_f —film azimuth angle, angle between film normal and due south;

θ_f —sun-film incidence angle, angle between solar beam and film surface;

θ_0 —solar zenith angle;

ψ_0 —solar azimuth angle.

Figure 14 shows, at the top, the cosines of the positive incidence angles for Sept. 1, 1988. The outside of the Blue End is not visible to the sun after 1030 EDT, but the outside of the Red End, which was not visible before 1030 EDT is visible the rest of the day. The outside of the Field Side is not visible after 1610 EDT.

These angles are used to project each directly illuminated film area on to the earth's surface, that is, the "effective" area receiving radiation is computed for each visible film face and these are converted to a weight by dividing by the total effective area. Figure 14 shows at the bottom the "effective" and total areas for April 20, 1988, while the bottom plot in Figure 15 shows the normalized areas or "weights" computed by dividing each effective area by the total area. This process is an approximation for an otherwise very complex calculation: determining the chamber volume that is seen through each outside face. The evaluation of the latter would require three dimensional integrations among three or four planes for each view. The area projection calculation method assumes that the chamber depth below each projected surface is the same, which is not the case in the actual chamber, but nevertheless the method is a reasonable first order approximation of the way in which the chamber volume is irradiated.

The next step in the CTM is to used the face incidence angles, *e.g.*, the values shown in the top of Figure 14, as input to the Teflon Film Transmission Model and to compute transmissions for each visible chamber face. Actually, what is calculated is the transmission at two wavelengths, 350 nm, and 900 nm for each face. Weights are applied to each transmission to produce an average chamber transmission at each of these wavelengths (see Figure 16). An average wavelength dependance factor ($\bar{\alpha}$) is computed from these two average transmissions. The 900 nm average direct film transmission, which we will denote as $\tau_{fD_{\lambda_o}}$ and the value of $\bar{\alpha}$ are sufficient to calculate the average chamber transmission at any wavelength less than 900 nm by,

$$\tau_{fD_\lambda} = \tau_{fD_{\lambda_o}} - \exp[-\bar{\alpha}(\lambda - \lambda_o)].$$

Figure 17 shows the average chamber transmission at 350 nm for a number of days between June 1 and November 1. The minimum transmissions between 1400

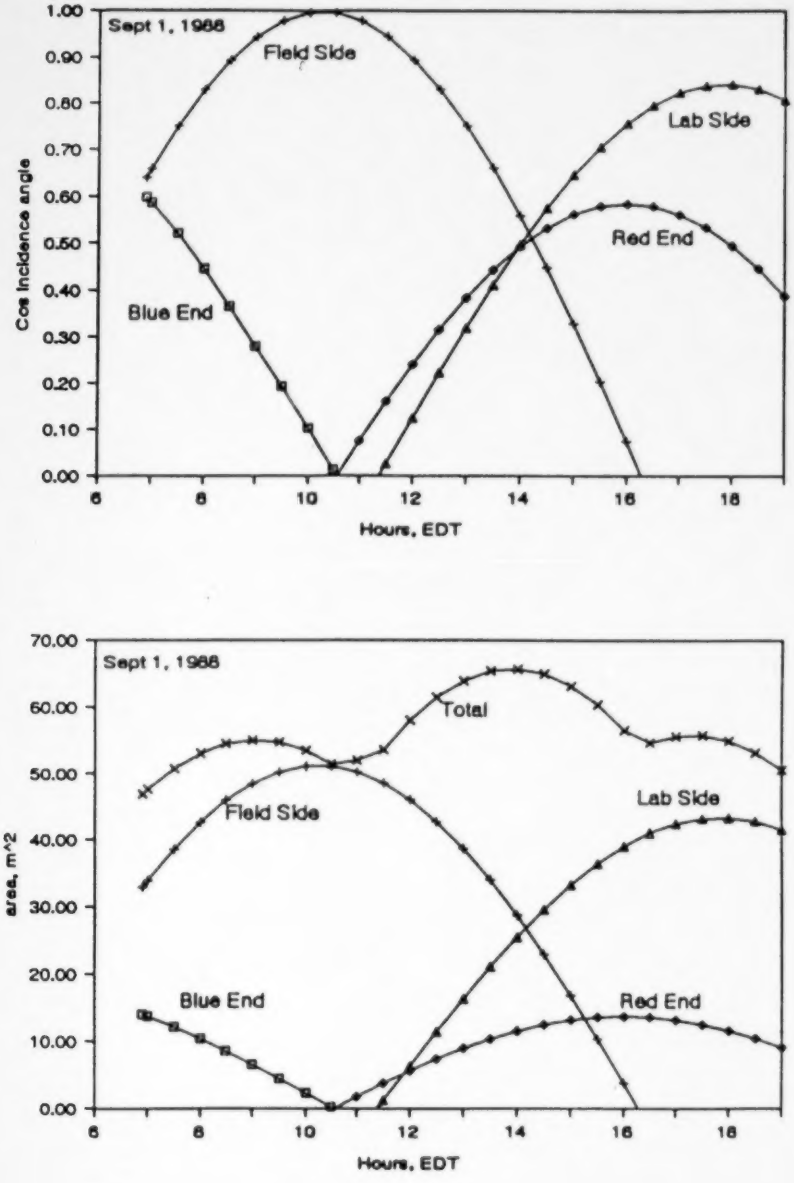

Figure 14. Angles and areas computed by the Chamber Transmission Model. Top: cosines of angle between sun and a normal to each of the faces of the chamber. Bottom: effective areas of the faces of the chamber and the total area.

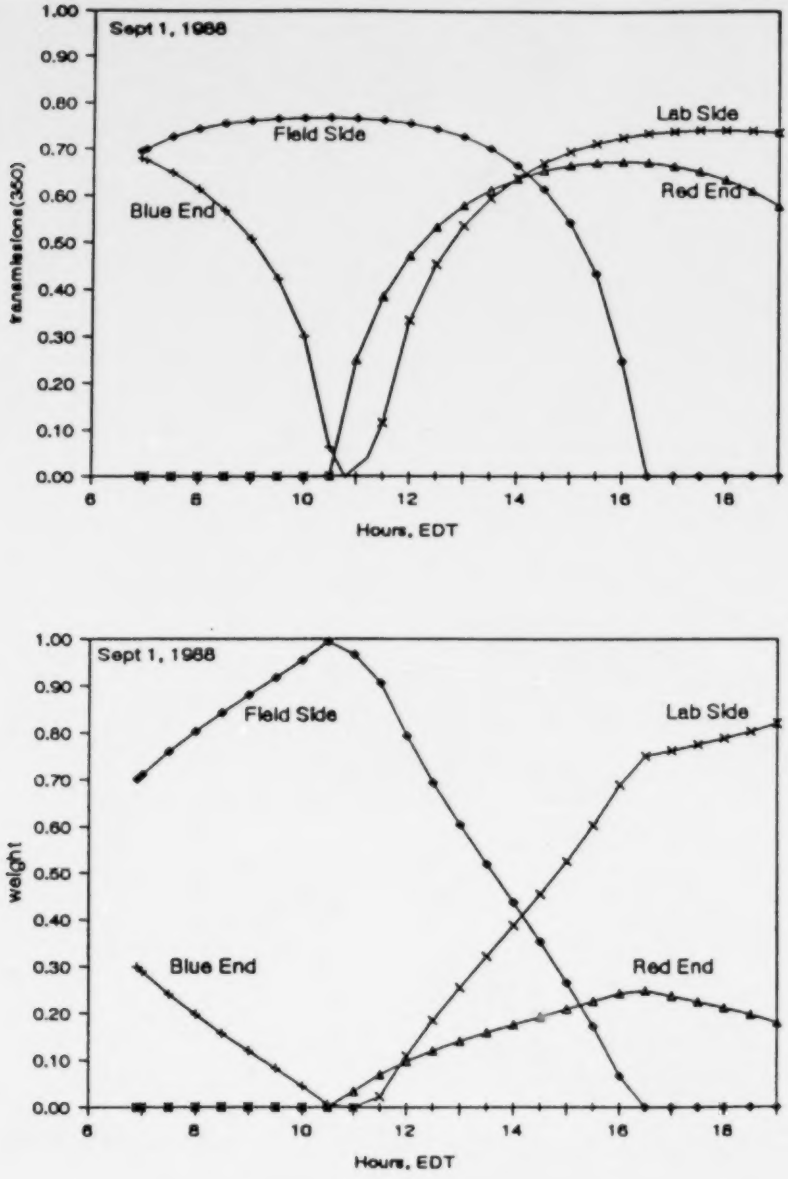

Figure 15. Face transmissions and weights computed by the Chamber Transmission Model. Top: The Teflon film model transmissions for each chamber face. Bottom: Weight applied to each face transmission to compute the total transmission. These are based on the areas in Figure 14, bottom.

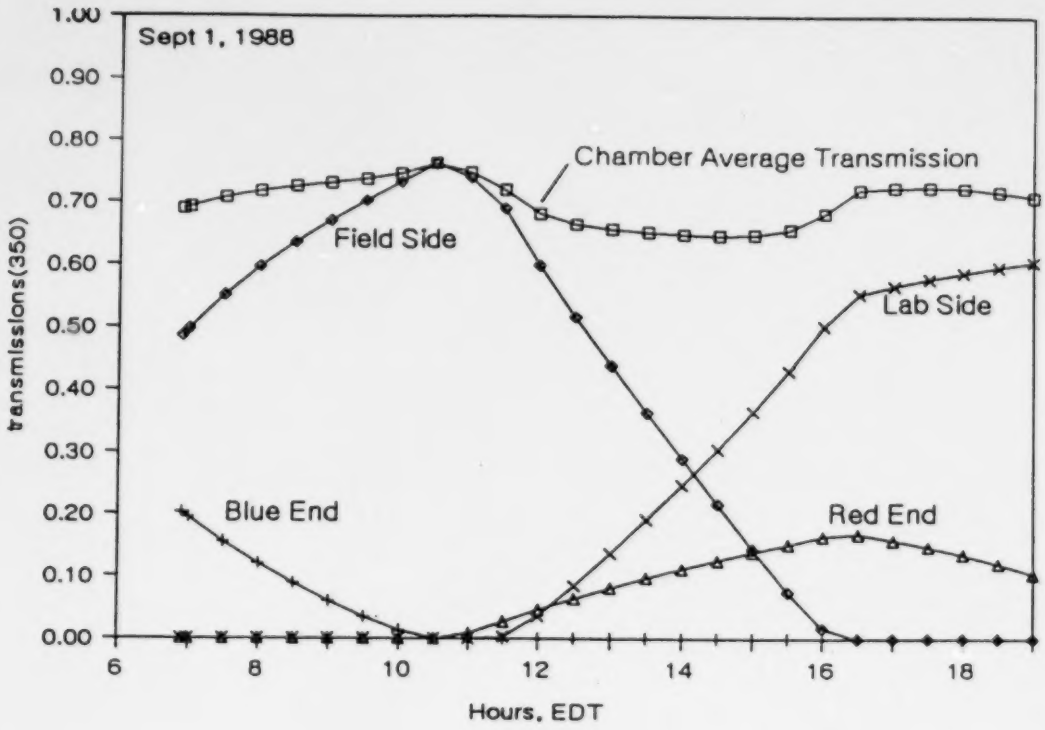

Figure 16. Chamber Average Transmission (at 350 nm) and the face contributions to the average.

and 1600 EDT occur when the sun's azimuth is in line with the Red End (*i.e.*, the view is down the long axis of the chamber). The maximum transmissions occur for a short time in the mornings between 0900 and 1100 EDT and after August 1 when the sun's azimuth is 63° and the altitude is 53°, which results in the Field Side being normal to the solar beam (see 1100 EDT in Figure 12). Before August 1, the sun is never in-line with the normal to the Field Side, that is, the solar altitude is higher than 53° when the azimuth is 63°, and both the Field Side and Lab Side are visible at the same time, lowering the average transmission.

For the average chamber diffuse transmission, a Monte Carlo approach was used with the TFTM to produce a distribution of transmissions. That is, 5000 transmissions were computed from random positions in the full sky hemisphere, and in a second test, 3000 transmissions were computed from random southern views. These transmissions were plotted in two and three dimensions as a function of the view zenith angle and view azimuth. The transmissions formed a reasonably smooth surface as a function of the view position. Based upon measured angular distributions of sky diffuse radiance[14] it is reasonable to assume that most of the diffuse radiation comes from a part of the sky near the sun's position, and therefore, we can take a "wide-area" average of the 3000 random surface and index it by the sun's position. This assumption is also confirmed by a number of ratios of "field" spectra to "tower" spectra on very clear days: the ratios are very nearly 0.98–1.0 from 300–850 nm, suggesting that the part of the sky blocked by trees is not contributing much to the spectral irradiance in the field.

Thus the Chamber Transmission Model for diffuse radiation consists of a look-up table of average transmissions as a function of view zenith and azimuth angles that is interpolated by solar zenith angle and solar azimuth. This average diffuse chamber transmission, $\tau_{fs_{t_o}}$, is computed at 900 nm and, as in the direct beam case, $\bar{\alpha}$ is used to compute the transmission at other wavelengths by,

$$\tau_{fs_\lambda} = \tau_{fs_{t_o}} - \exp[-\bar{\alpha}(\lambda - \lambda_o)].$$

A routine is also included in the Chamber Transmission module to interpolate the value of the chamber floor reflectivity and the chamber walls back reflectivity as a function of wavelength. This routine uses the data in Table 2.

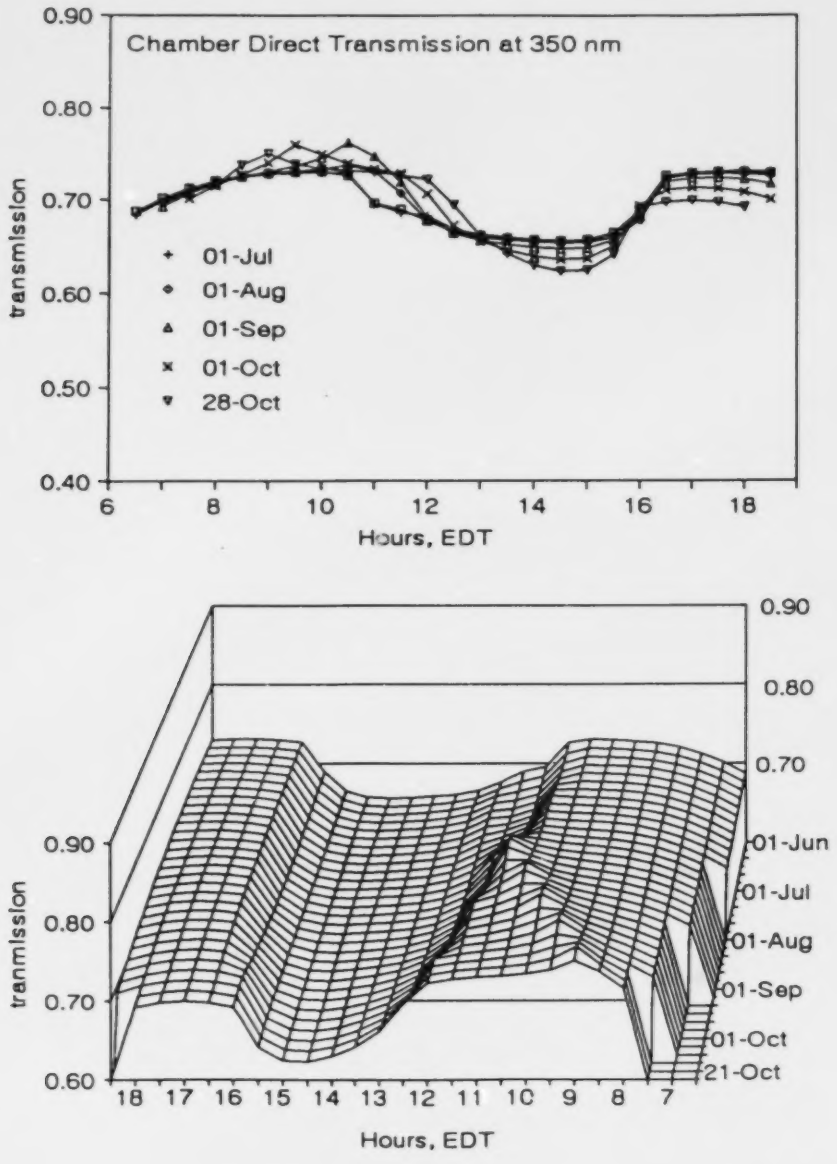

Figure 17. Daily profiles of chamber direct transmission for six summer and fall months months.

Measurement and Modeling of In-Chamber Irradiances

To assist in understanding the in-chamber irradiance, both an Eppley total solar radiation sensor and an Eppley UV radiometer are operated inside the chambers. In addition, on many days in 1986, 1987, and 1988 extensive measurements were made inside and outside the chamber with the Licor spectroradiometer.

Broadband UV Irradiances

Figure 18 shows two days of tower and in-chamber Eppley UV radiometer irradiances. (Note:The outside Eppley signals had interference in the form of noise spikes that resulted in the instantaneous samples collected by the computer having the appearance of not being from clear days; these were very clear days.) In Figure 12, the location of the in-chamber UV radiometer is shown as a "dot" on the floor of the RED chamber. Thus, in Figure 12, at 0930 EDT, the in-chamber radiometer was just visible in through panel B4. Previously, it was in panel A4, and thus, as the radiometer data suggests, the radiometer was in a shadow just before 0930 EDT on 20-Apr-1988. Other chamber structural members are responsible for the other "dips" in the in-chamber radiometer data in Figure 18. During these periods, the direct beam of the sun is blocked and the radiometer is effectively reporting the diffuse and reflective components only.

Also shown in Figure 18 are two transmission curves in each plot, which were computed from the Chamber Transmission Model, but by different methods. The ones marked "Chamber Average Transmission" were computed as described above. Inspection of the Eppley data in these plots, however, shows that the Chamber Average Transmission does not describe the difference between the outside and inside Eppley UV data. This is because the in-chamber Eppley is at a fixed location in the chamber, it is not moving around like the air, and therefore it is not experiencing the "average" irradiant conditions. Instead, the in-chamber sensor is viewing the sun though specific panels with particular transmissions at given times (see Figure 12). To account for this fixed location in the chamber transmission model, additional geometrical information was added (the location of the sensor and the co-ordinates of the Red End) and a routine that used projective geometry to determine when the Eppley sensor was visible through either chamber side or through the Red End panel. Using this information, the routine assigns as the chamber transmission for the Eppley sensor only the film transmission for the face that includes the view of the in-chamber sensor and only for the wavelength 350 nm, which is the peak of the Eppley response curve. This transmission is called the "Eppley Transmission" in Figure 18 and will be denoted as τ_{JDE} in discussions below.

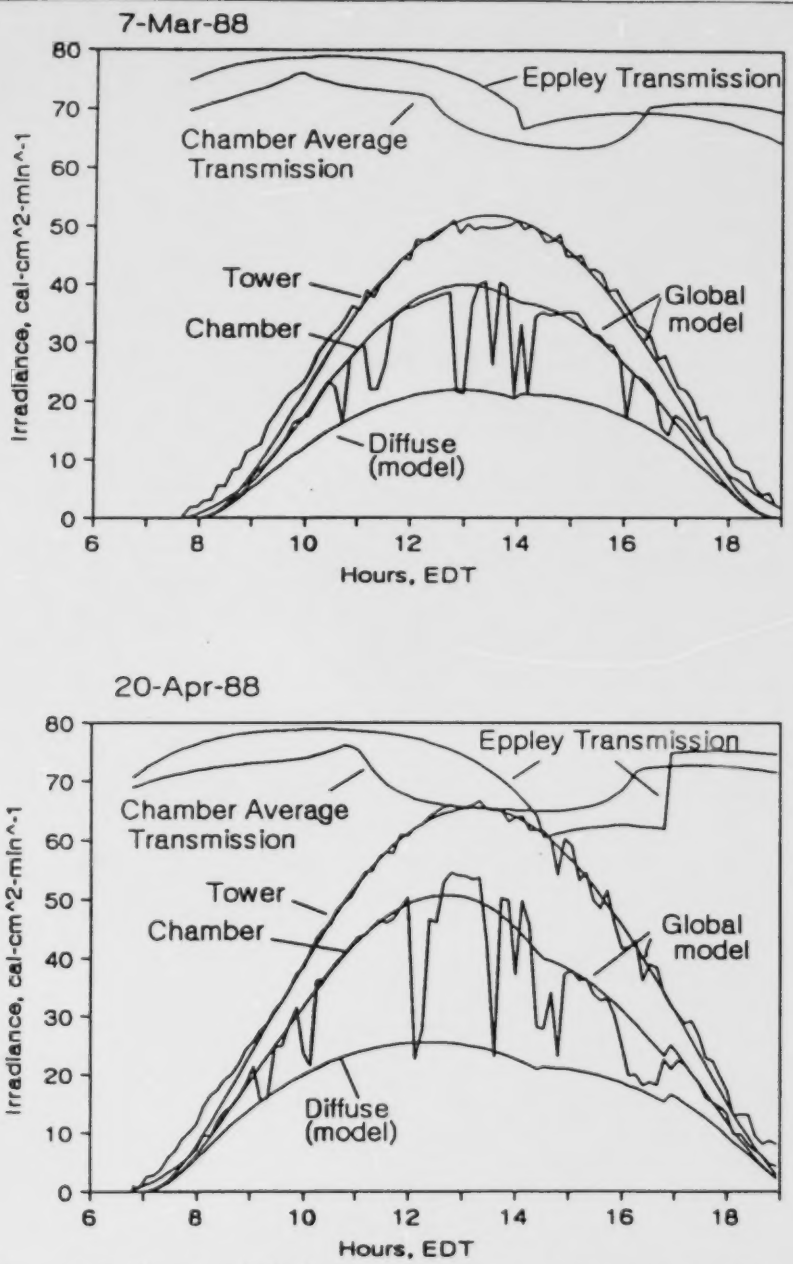

Figure 18. Tower and In-chamber Eppley UV radiometer irradiances and the UNC Chamber Transmission Model and broad band UV model predictions. Also shown are the computed chamber transmissions.

On March 7, 1988, a beam from the sun to the in-chamber Eppley radiometer never went through the Red End, but at 1320 EDT, the beam switched from the Field Side to the Lab Side. On April 20, 1988, a beam from the sun to the in-chamber Eppley crossed into the upper Red End panel at 1430 EDT (see Figure 12) and crossed into the Lab Side at 1500 EDT. The transmission through the Red End was significantly lower than the transmission through either side.

The model data shown in Figure 18 were produced by

1) using SOLCALC and BBMODEL to calculate the tower or outside values

$$\mathcal{D}, \quad \mathcal{S}, \quad \mathcal{R}, \quad \text{and } \mathcal{G};$$

2) using the Chamber Transmission Model (*e.g.*, CHMMODEL) to calculate the Eppley transmissions, τ_{fDE} and τ_{fSE};
3) using the following equations to compute the in-chamber values,

$$\begin{aligned}
\langle \mathcal{D} \rangle &= \tau_{fDE} \mathcal{D} \\
\langle \mathcal{S} \rangle &= \tau_{fSE} (\mathcal{S} + \mathcal{R}) \\
\langle \mathcal{R} \rangle &= \frac{0.04(\langle \mathcal{D} \rangle + \langle \mathcal{S} \rangle)}{(1 - 0.04)} \\
\langle \mathcal{G} \rangle &= \langle \mathcal{D} \rangle + \langle \mathcal{S} \rangle + \langle \mathcal{R} \rangle
\end{aligned}$$

4) plotting $\mathcal{G}$, $\langle \mathcal{G} \rangle$, and $(\langle \mathcal{S} \rangle + \langle \mathcal{R} \rangle)$.

The best agreement between the model and the data occurred when

$$\tau_{fSE} = \tau_{fDE}$$

that is, when the diffuse transmission was the same as the direct beam transmission. The measured angular distributions of sky diffuse radiance performed by Hay[14] also suggests that most of the diffuse radiation *does* come from the sky near the sun.

Spectral Irradiances

Another way to evaluate the general form of the in-chamber irradiance model is shown in Figure 19. The top plot shows outside and inside chamber spectroradiometer spectra for direct and diffuse components. A ratio of the two direct components (the direct transmission) is also shown with predictions from a model of the form

$$\tau_\lambda = 0.875 - \exp[-0.00849(\lambda - 110)].$$

These values are very consistent with the CTM parameters which were determined with the SMUTT apparatus, thus it appears that the SMUTT- based model does describe the chamber film. The "Diffuse and Reflective" spectra at the bottom of the top plot show that above 400 nm the chamber *does* have a higher non-direct irradiance caused by the floor and walls.

The bottom plot in Figure 19 is a test of the *form* of the in-chamber model, in that outside measured values are transformed to inside values (as opposed to using outside model-predicted values). That is, the in-chamber model curves were computed from

$$\langle \mathcal{D}_\lambda \rangle = \tau_{fD_\lambda}(\text{Direct})$$
$$\langle \mathcal{S}_\lambda \rangle = \tau_{fD_\lambda}(\text{Diffuse and Reflective})$$
$$\langle \mathcal{R}_\lambda \rangle = \rho\rho_{w\lambda}(\langle \text{Global} \rangle)$$

where $\rho\rho_{w\lambda}$ was given in Table 2 and $\langle \mathcal{D}_\lambda \rangle$ and $(\langle \mathcal{S}_\lambda \rangle + \langle \mathcal{R}_\lambda \rangle)$ are the values labeled "Model" in the figure. Note that the last equation is just a transformation of the original form, that is,

$$\mathcal{R}_\lambda = \rho_\lambda \rho_{a\lambda} \mathcal{G}_\lambda$$
$$\mathcal{R}_\lambda = \rho_\lambda \rho_{a\lambda} (\mathcal{D}_\lambda + \mathcal{S}_\lambda + \mathcal{R}_\lambda)$$
$$\mathcal{R}_\lambda = \rho_\lambda \rho_{a\lambda} (\mathcal{D}_\lambda + \mathcal{S}_\lambda) + \rho_\lambda \rho_{a\lambda} \mathcal{R}_\lambda$$
$$\mathcal{R}_\lambda = \frac{\rho_\lambda \rho_{a\lambda} (\mathcal{D}_\lambda + \mathcal{S}_\lambda)}{1 - \rho_\lambda \rho_{a\lambda}}$$

Another example, calculated in the same manner, is shown in Figure 20. Here again we see the expected form of the direct transmission and that the inside diffuse and reflected component is less than that outside below 400 nm. Again as above, the inside diffuse and reflected component can be calculated by applying the direct transmission to the outside diffuse and reflected component and adding the chamber reflected component calculated by $\rho\rho_{w\lambda} \langle \mathcal{G}_\lambda \rangle$ (slightly lower values of $\rho\rho_{w\lambda}$ than are given in Table 2 were needed to give the fit in Figure 20).

Finally, Figure 21 shows model calculations for all components of the model. That is, the computed spectral components for the outside model shown in Figure 7 were used along with the following equations to compute the inside model irradiances,

$$\tau_{fD_\lambda} = 0.800 - \exp[-0.00849(\lambda - 110)]$$
$$\langle \mathcal{D}_\lambda \rangle = \tau_{fD_\lambda} \mathcal{D}_\lambda$$
$$(\langle \mathcal{S}_\lambda \rangle + \langle \mathcal{R}_\lambda \rangle) = \tau_{fD_\lambda} (\mathcal{S}_\lambda + \mathcal{R}_\lambda) + \rho\rho_{w\lambda} \langle \mathcal{G}_\lambda \rangle$$
$$\langle \mathcal{G}_\lambda \rangle = \langle \mathcal{D}_\lambda \rangle + \langle \mathcal{S}_\lambda \rangle + \langle \mathcal{R}_\lambda \rangle$$

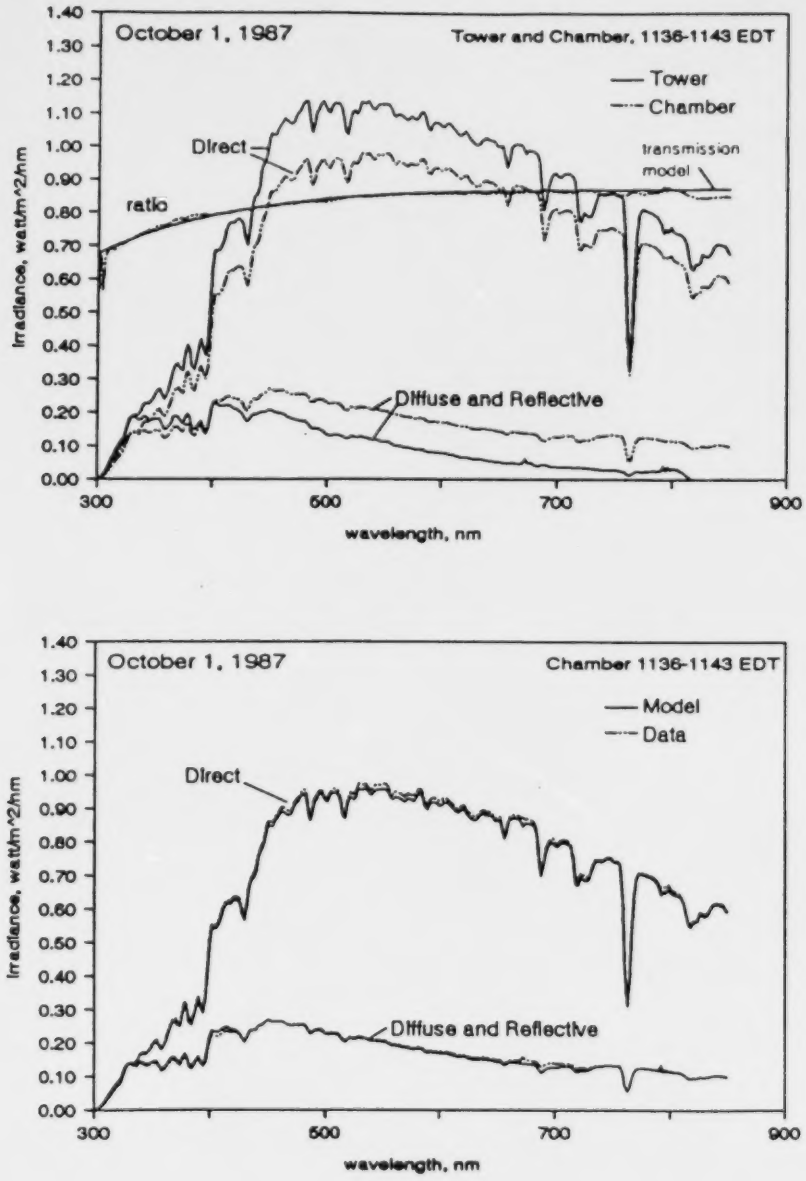

Figure 19. Top: Licor Spectroradiometer spectra inside and outside UNC chamber on a low aerosol day. Bottom: "model" of inside using outside spectra and transmission and reflection factors.

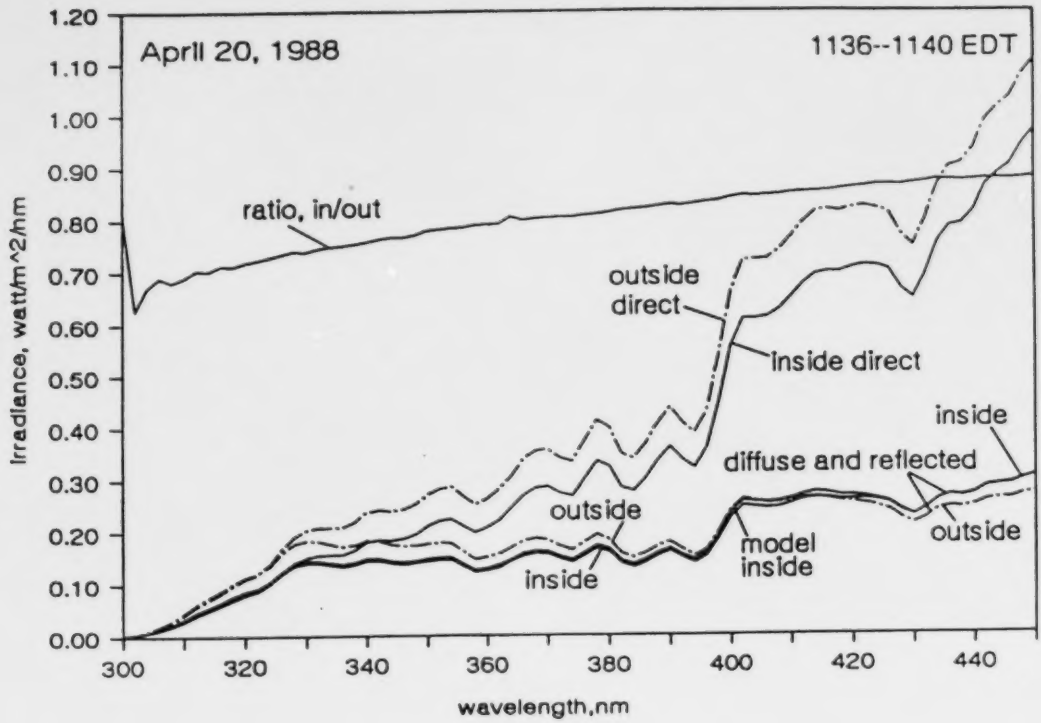

Figure 20. Licor Spectroradiometer spectra inside and outside the UNC chamber. 'Model' of diffuse uses outside spectra, transmissions, and reflections.

and because $\langle \mathcal{G}_\lambda \rangle$ appears on both sides of these equations, iteration is needed to solve the system; about 5 cycles of evaluation is sufficient to reach convergence. Notice again that the direct transmission can be applied to both the direct and diffuse components.

These examples of measured and modeled irradiances illustrate that the general approach to calculate in-chamber irradiances works well. Furthermore, the modeling tools *do* produce good agreement with measured conditions for in-chamber irradiances and we have reason to believe that they will work well in the next extension to the computation of spherical irradiances or actinic flux in the chamber.

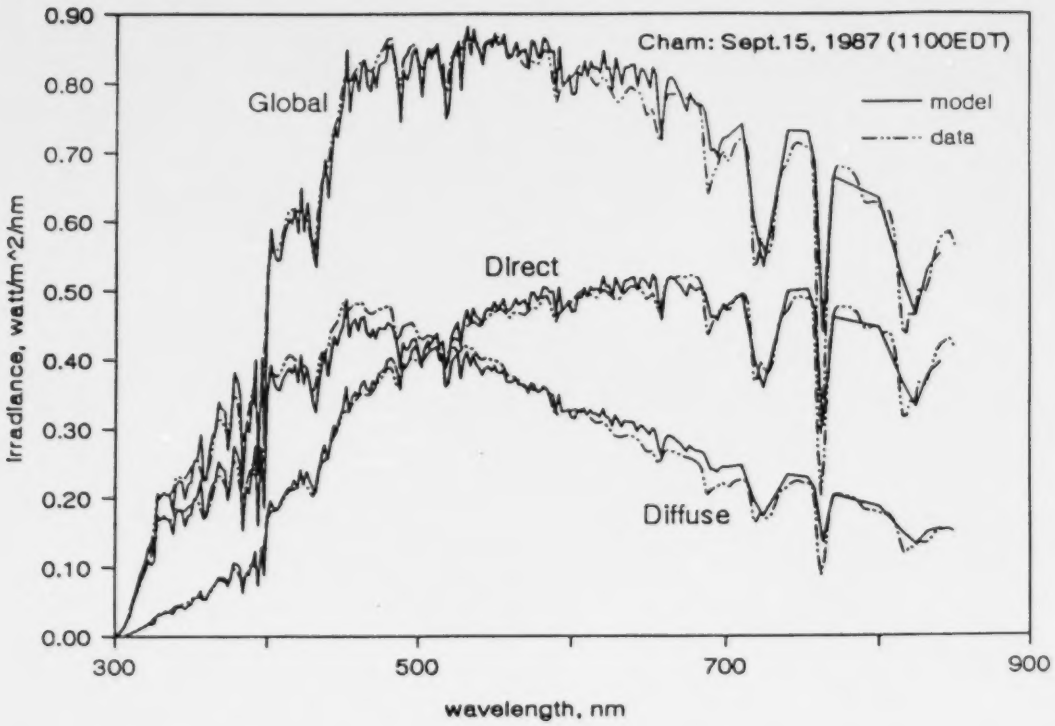

Figure 21. Licor Spectroradiometer spectra inside the UNC chamber and model predictions using JSPECTRA model predictions of outside spectra, transmissions, and reflection factors.

Calculation of In-Chamber Actinic Flux

In this step, we will describe CHMJSMOD which computes the in-chamber actinic flux for every day in the data base SOLCLIM. The program uses this data base as the source of all the inputs needed for the aerosol model and for other inputs for the spectral transmission functions in JSMODEL. These are the same as for the BBMODEL used above in the TSR and UV modeling steps. In addition, we will use the "cloud correction factors," τ_c and $\widehat{\tau_c}$, that were computed in the earlier step and stored in SOLCLIM. We will apply $\widehat{\tau_c}$ to wavelengths below 400 nm and τ_c to wavelengths above 400 nm.

For each time CHMJSMOD calculates the actinic flux, CHMMODEL (which contains the Chamber Transmission Model) is used to calculate

$\tau_{fD_{\ell_o}}$ –the *average* chamber transmission for direct beam radiation at the reference wavelength, $\ell_o = 900$ nm;

$\tau_{fS_{\ell_o}}$ –the *average* chamber transmission for diffuse radiation at the reference wavelength, $\ell_o = 900$ nm;

$\bar{\alpha}$ –the *average* wavelength variation factor for this time.

From these, CHMJSMOD computes the chamber transmission at wavelengths below 900 nm by

$$\tau_{fD_\lambda} = \tau_{fD_{\ell_o}} - \exp[-\bar{\alpha}(\lambda - \lambda_o)]$$
$$\tau_{fS_\lambda} = \tau_{fS_{\ell_o}} - \exp[-\bar{\alpha}(\lambda - \lambda_o)]$$

In addition, the CHMMODEL is used to interpolate Table 2 for the chamber floor reflectivity, $\rho_{f\lambda}$ and for the wall-floor back reflection, $\rho\rho_{w\lambda}$.

JSMODEL is called to calculate the outside irradiance components

$$\mathcal{N}_\lambda, \quad \mathcal{S}_\lambda, \quad \widetilde{\mathcal{S}_\lambda}, \quad \text{and} \quad \mathcal{R}_\lambda.$$

CHMJSMOD then transforms the outside flux components to inside the chamber. The horizontal irradiance *inside* the chamber is needed, because that is what is reflected from the floor, so all outside flux components are brought into the chamber by applying the average chamber transmissions and the "cloud correction factors"

to the outside fluxes. The operations are

$$\begin{aligned}
\langle \mathcal{N}_\lambda \rangle &= \tau_{fD_\lambda} \tau_c \mathcal{N}_\lambda \\
\langle \mathcal{D}_\lambda \rangle &= \mu \langle \mathcal{N}_\lambda \rangle \\
\langle \mathcal{S}_\lambda \rangle &= \tau_{fS_\lambda} \tau_c (\mathcal{S}_\lambda + \mathcal{R}_\lambda) \\
\left\langle \widetilde{\mathcal{S}_\lambda} \right\rangle &= \tau_{fS_\lambda} \tau_c (\widetilde{\mathcal{S}_\lambda} + \mathcal{R}_\lambda) \\
\left\langle \widetilde{\mathcal{R}_\lambda} \right\rangle &= \frac{2(\langle \mathcal{D}_\lambda \rangle + \langle \mathcal{S}_\lambda \rangle)(\rho_{f\lambda} + \rho\rho_{w\lambda})}{1 - \rho\rho_{w\lambda}} \\
\left\langle \widetilde{\mathcal{G}_\lambda} \right\rangle &= \langle \mathcal{N}_\lambda \rangle + \left\langle \widetilde{\mathcal{S}_\lambda} \right\rangle + \left\langle \widetilde{\mathcal{R}_\lambda} \right\rangle \\
\langle \mathcal{A}_\lambda \rangle &= 3.02 \times 10^{13} \lambda \left\langle \widetilde{\mathcal{G}_\lambda} \right\rangle .
\end{aligned}$$

The $\mathcal{H}_\lambda$ values and the absorption coefficients used by JSMODEL are at 2 nm steps from 300 to 850 nm (275 intervals) and there are another 5 intervals from 850 to 1040 nm. This is too many data items to save at each time of day we need actinic flux, so, after the flux is calculated, it is combined into 92 intervals

λ_e	size, nm	number
300–420	2	61
430–560	10	14
580–760	20	10
800–1040	40	7

Actinic fluxes are calculated every 16 minutes beginning 8 minutes after sunrise. They are written to a binary file for each day. These files have names of the form

mmddyy.FIB

where .FIB is from Flux Inside Binary.

CHMJSMOD can also store outside actinic flux values in files named .FOB for Flux Outside Binary.

In-chamber Actinic Flux

Figure 22 shows the calculated flux components for 1316 EDT on August 5, 1984 (solar noon). While the flux inside and outside the chamber appear to be very similar in magnitude in the UV portion of the spectrum, the flux is about 40% higher inside than outside in the visible portion of the spectrum. The reason for this result is presented somewhat clearer in Figure 23. Here we see that the diffuse and normal beam components are always reduced in the chamber compared to outside values, but, in the UV portion, the reflective component is 40–80% higher, and in the visible portion, it is 180% higher inside than outside the chamber. The attenuation and amplification of the different components nearly balance in the UV portion, resulting in little change in the total actinic flux and species with only UV absorption spectra will photolyze nearly the same inside as outside. Those species with absorption spectra in the visible spectrum, however, will photolyze at a significantly faster rate inside the chamber.

Figure 24a,b shows inside and outside actinic flux for four different times on August 5, 1984. In the morning, the inside flux is higher than the outside flux for all wavelengths. Later in the day the chamber transmission at wavelengths below 330 nm is low enough that the floor reflection can not compensate and the chamber actinic flux at these wavelengths is less than outside. As time increases, the cross over point at which the inside flux is less than the outside flux increases to 350 and then 360 nm. In the visible spectrum, however, the actinic flux is significantly higher inside the chamber at all times.

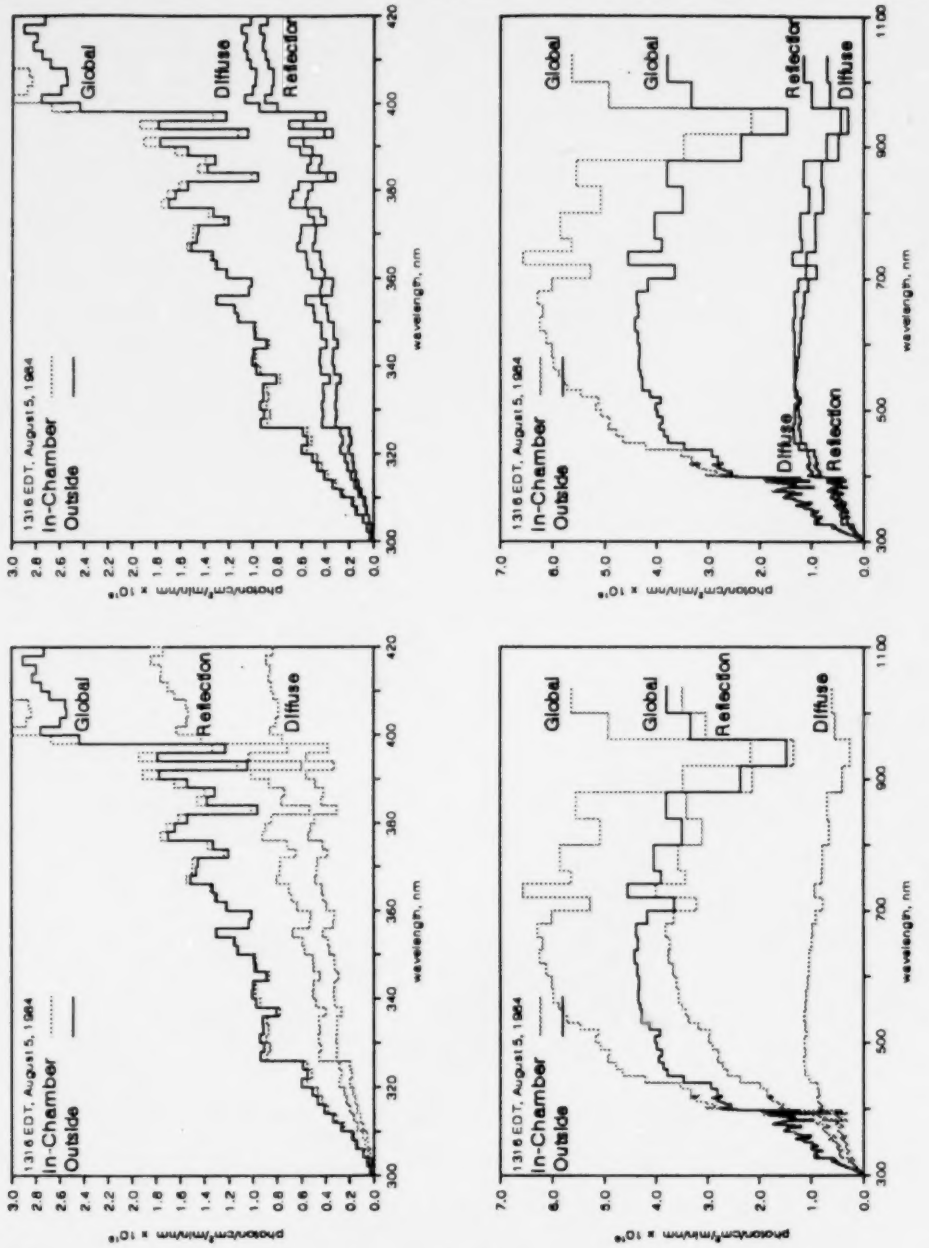

Figure 22. Global actinic flux and its components for solar noon, August 5, 1984. Top: spectral range 330–420 nm. Bottom: spectral range 300–1100 nm. Bold lines: *outside* values; Light lines: *inside* chamber values. Left: the components for inside the chamber; Right: the components for outside.

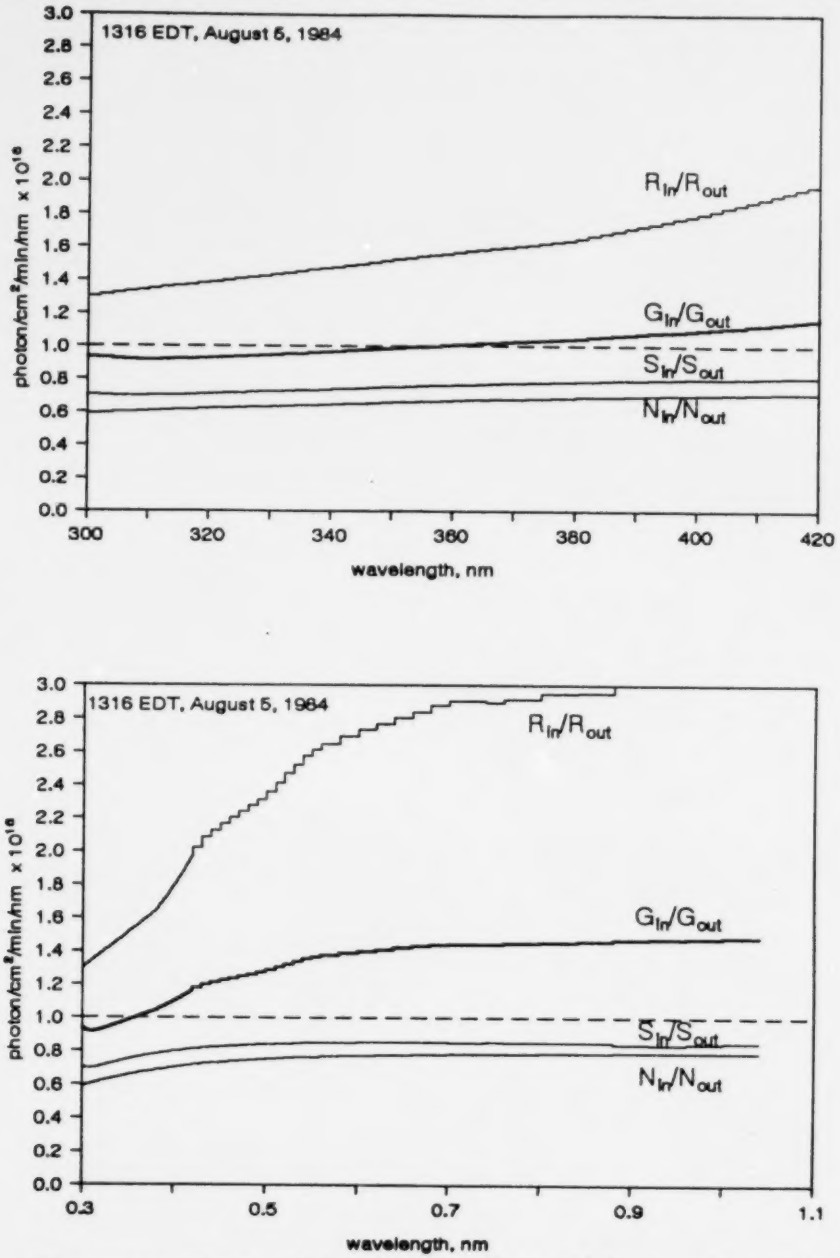

Figure 23. Ratio of global actinic flux and its components inside to outside for solar noon August 5, 1984. G–global ratio; R–reflected component ratio; S–diffuse component ratio; N–normal component ratio.

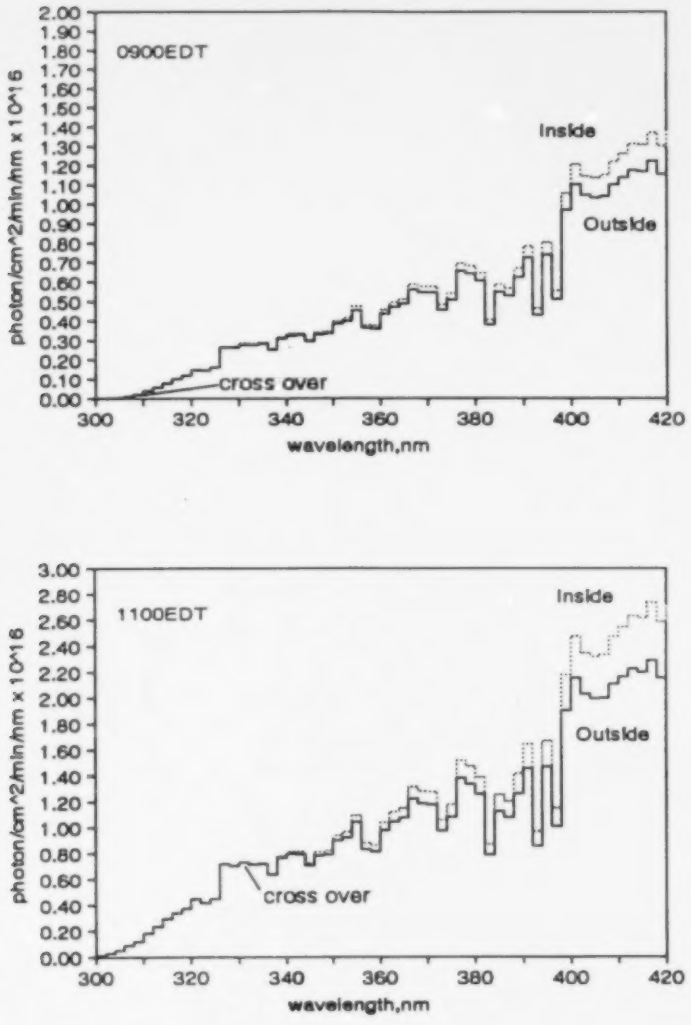

Figure 24a. Actinic Flux Spectra inside and outside UNC Chamber for morning of August 5, 1984.

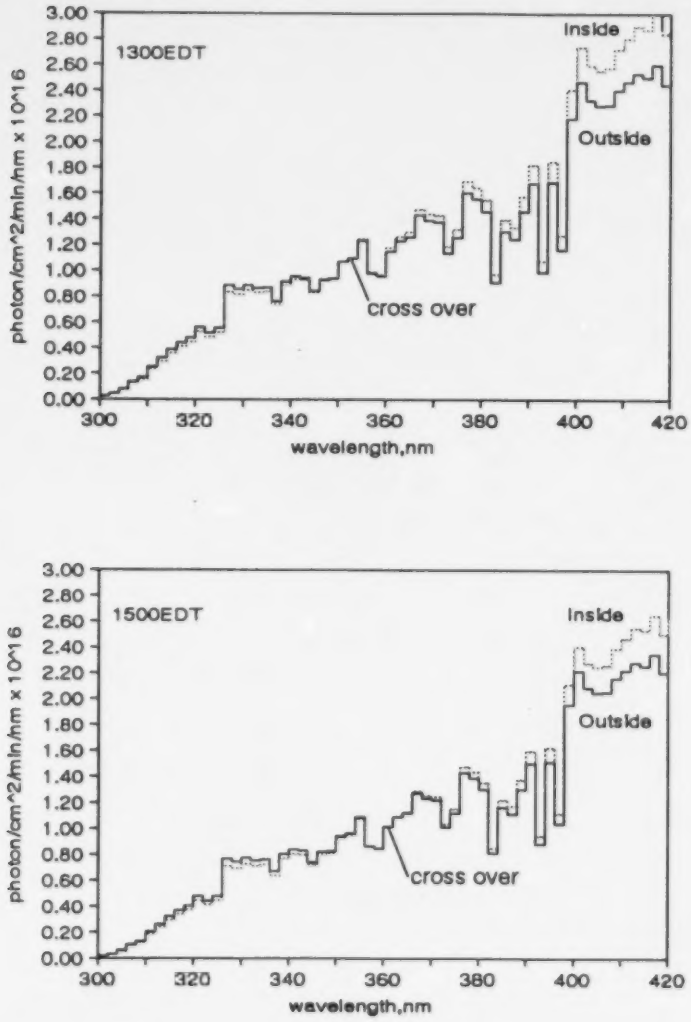

Figure 24b. Actinic Flux Spectra inside and outside UNC Chamber for afternoon of August 5, 1984.

In-chamber Photolysis Rates

In the last step, the actinic flux at each 16 minute time is used with species absorption cross sections and reaction quantum yields to compute reaction rates. The exact description of how this is done is given in the next chapter. Selected results are described here.

Figure 25 compares the NO_2 photolysis rate inside and outside the chamber for August 5, 1984. The absorption cross section for NO_2 extends from 300 nm to 410 nm. As expected from the conditions shown in Figure 24, therefore, the NO_2 rate is nearly the same for the inside and outside in the morning, but by mid-day it is higher inside than outside. Also note that in Figure 24a the difference is largest at 1100 EDT as is the rate.

The product of the absorption cross section and quantum yield for HCHO's reactions is greater than zero only below 360 nm. This portion of the spectra in both the outdoor and indoor situations are nearly identical until near mid-day when the inside actinic fluxes below 360 nm are lower than the outside fluxes. Therefore, in Figure 25 at the bottom, the photolysis rates for HCHO are either the same inside and outside or are lower inside.

Figure 26 shows the photolysis rates for ozone. Ozone has two absorption regions, one below 320 nm and one above 500 nm. Because the actinic flux below 320 nm is essentially always less inside than outside, the O_3 photolysis to produce O^{1D} is always less inside than outside. In the case of O_3 photolysis to produce O, however, the actinic flux above 500 nm is always significantly larger inside than outside and therefore the inside rate is much larger than the outside rate. Also note that there were different corrections for the predominantly TSR wavelengths (>400 nm) than for the mostly UV wavelengths (<400 nm) and thus there was an afternoon correction for the O photolysis that did not occur for the O^{1D} photolysis.

As a final check, a program SEGUVNO2 plots the SegFile UV radiometer data, the NO_2 photolysis rate, and the HCHO radical photolysis rates for each day in the SOLCLIM data base. A selection of these plots are included in Appendix B, Part III.

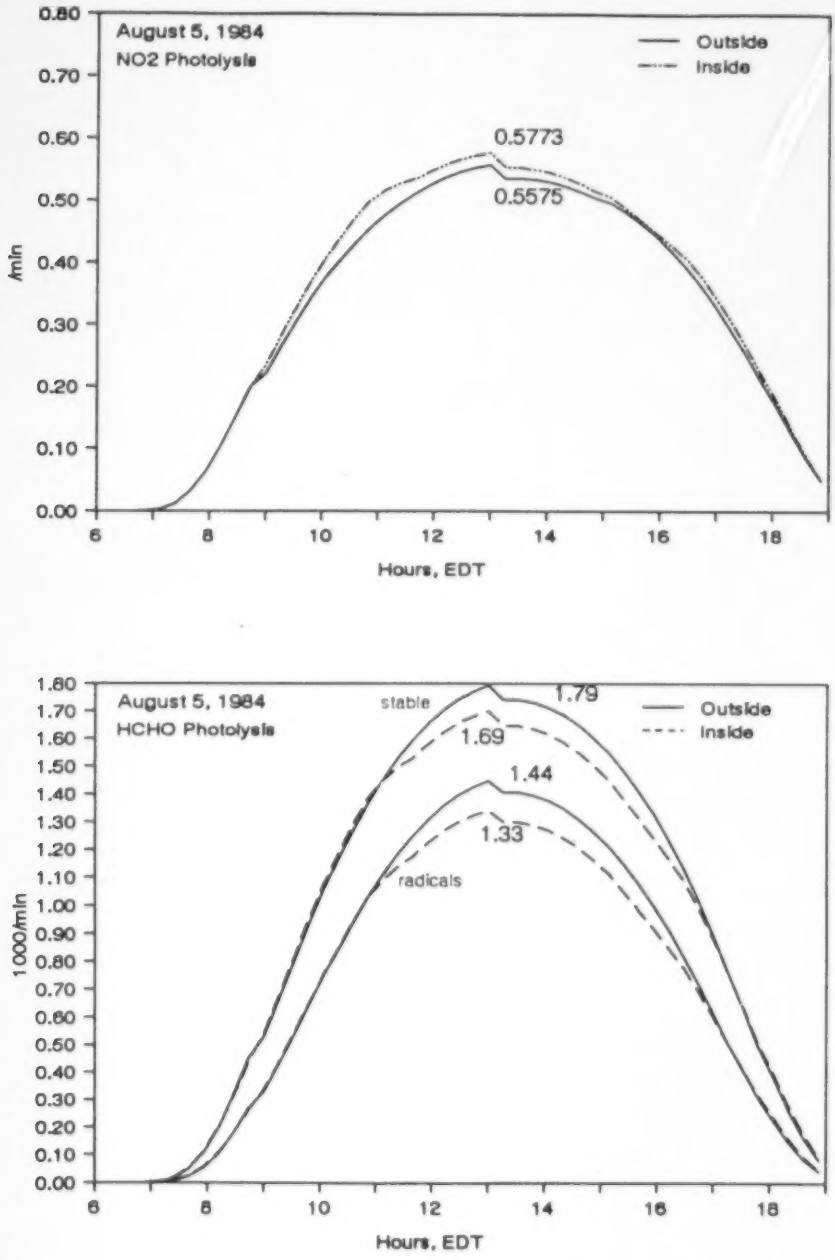

Figure 25. Top: In-chamber and outside NO_2 photolysis rate for August 5, 1984. Bottom: In-chamber and outside stable (dark line) and radical photolysis rates for HCHO.

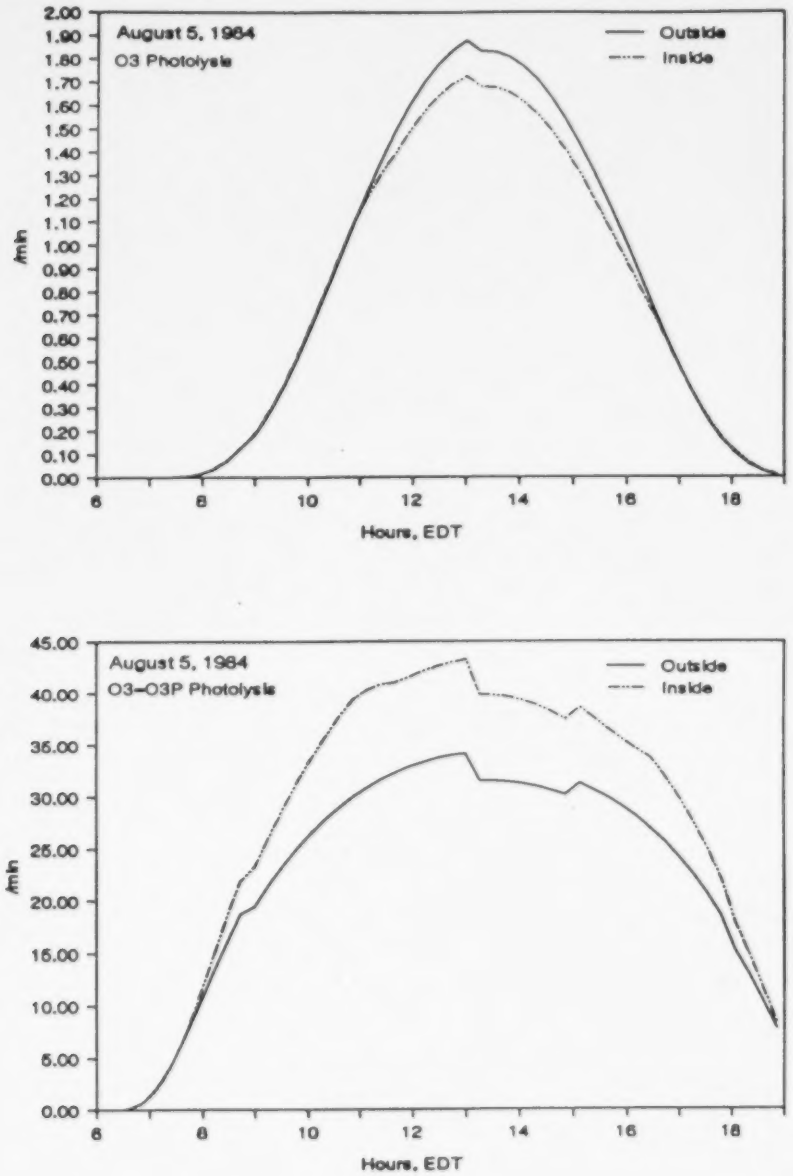

Figure 26. Top: In-chamber and outside O_3 to O^{1D} photolysis rate for August 5, 1984. Bottom: In-chamber and outside O_3 to O photolysis rates.

2

Calculating the Rate of Photolytic Reactions

Introduction

It would seem that given the actinic flux, the calculation of the photolysis rates for photodissociation reactions would be straightforward. Like many other parts of the mechanism production activity, however, when there are choices to be made, different mechanisms builders often make different choices. For example, Carter mostly used the cross sections (σ_λ) and quantum yields (Φ_λ) that appear in the NASA evaluations,[15] while Gery often used σ_λ and Φ_λ from the literature sources which were sometimes cited in the NASA review, but which frequently had data that do not necessarily appear in the NASA document, for example, large tables of higher resolution spectra. Our comparison of the choices made by Carter and by Gery have revealed some "procedural" problems, and certainly have revealed interpretational issues that lead to some differences in predictions.

As an example of this point, in Carter's calculation method all input spectra, cross-sections, and quantum yields are treated as "points" at the given wavelength. He 'connects' the points by straight lines and computes the integral of the product of the equations of the two line segments as needed. For NO_2 for example, Carter uses the values given in a table in the NASA recommendations in which the cross-sections are given every 5 nm. The NASA text states, however,

> "Table 10 lists a sample of the recommended absorption cross sections of nitrogen dioxide, taken from the work of Bass, *et al.*, who report extinction coefficients every 1/8 nm between 185 and 410 nm at 298 K. For atmospheric photodissociation calculations which require cross sections values averaged over appropriate wavelength intervals the original literature report should be consulted."

No definition of "sample" is given in the NASA discussion.

Gery used the original Bass 1/8 nm cross-section data for NO_2 and averaged it every 1 nm. In our calculations we too have used integral averaging of the 1/8 nm data to calculate average NO_2 cross-sections in 1 nm wide intervals from 298 nm to 420 nm. Comparison of the cross sections in the NASA table with Bass's original data shows that the NASA data *are* the 1/8 nm values that occurred at the cited wavelenths. Above 340 nm, however, the NO_2 spectrum shows significant structure that is not well represented by the 5 nm spaced points. Figure 27a compares the values used by Carter and the 1 nm averaged cross-sections computed by UNC. As shown in Figure 27b, a difference in the NO_2 photolysis rate arises when these two sets of cross-sections are used. Table 3 shows that other differences also occur, mostly due to differences in treatment of the same literature sources (*i.e.*, using 'points' vs. average intervals), but sometimes the difference was due to choosing one source of kinetics data over another source (*e.g.*, HCHO rates).

To help resolve some of these procedural questions, a complete discussion of the calculation of photolysis rates, beginning with definitions of quantities, and proceeding to descriptions of methods for performing the calculations will be presented in the rest of this chapter.

Table 3. Comparison of photolysis rates calculated by Carter's procedure and by UNC's procedure for in-chamber conditions at 1316 EDT, August 5, 1984. All the differences except HCHO are due to different treatment of the reaction potential spectra. For HCHO, Carter uses an average of Moortgat and Bass σ_λ and UNC uses only Bass's σ_λ.
(units are min^{-1}, except * which are $1000 \times min^{-1}$)

Reaction	Carter	UNC	% diff.
NO2	0.5474	0.5346	2.4
NO3=NO2	15.4815	14.8760	4.1
O3O1D*	1.7324	1.7209	0.7
O3=O3P*	42.2818	40.2601	5.0
HCHO,R*	1.4624	1.2616	15.9
HCHO,M*	2.1889	1.5920	37.5
RCHO*	1.0147	0.9697	4.6
KETONE*	0.0750	0.0714	5.0
GLYOXAL*	2.2361	2.1842	2.4

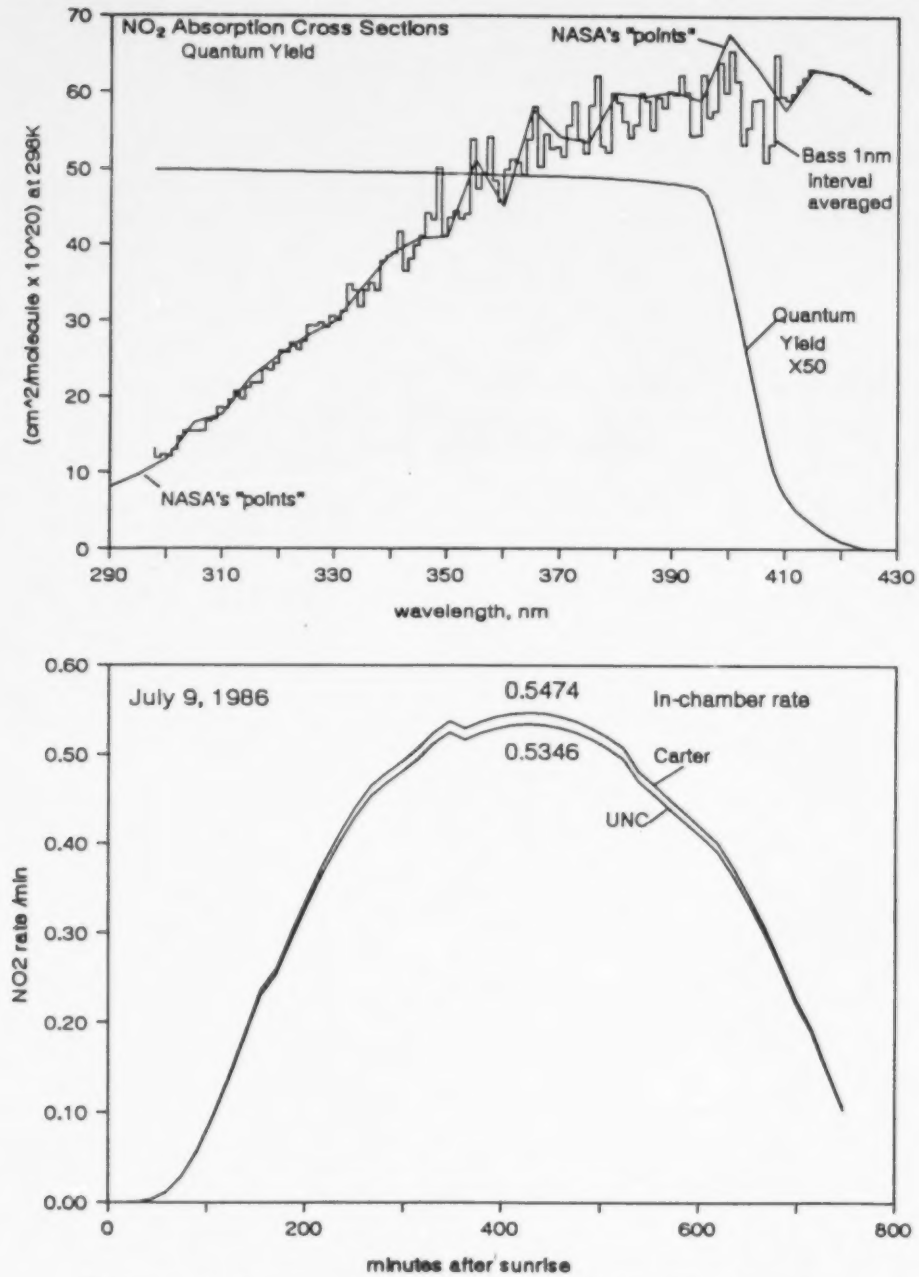

Figure 27. Comparison of Carter's and UNC's NO_2 absorption cross-sections (a, top) and resulting photolysis rates for a selected day in the UNC chamber (b, bottom).

Idealized Spectral Quantities and Units

Spectral quantities are limiting point values, that is, they give the magnitude at a point on the wavelength line. Thus they have no wavelength "width" and the units include "per nm". In this dicusssion, spectral quantities will have λ subscripts. The names, symbols, and units of the quantities we will use are:

a) *spectral spherical irradiance* or spectral actinic flux, $\mathcal{A}_\lambda$, is a radiant flux density and has units of photons-cm^{-2}-sec^{-1}-nm^{-1} (or photons-cm^{-2}-min^{-1}-nm^{-1})

b) molecular *absorption cross-section*, σ_λ, is unique for each photolytic species and has units of cm^2-molecule^{-1}

c) process *quantum yield*, Φ_λ, is the fraction of the absorbing molecules at λ that proceed by a particular *reaction* pathway; Φ_λ is unitless;

d) *spectral reaction potential*, $\mathcal{P}_\lambda$, is the product of σ_λ and Φ_λ;

e) *spectral photolysis rate*, j_λ, is the product of spectral actinic flux and spectral reaction potential,

$$j_\lambda = \mathcal{A}_\lambda \mathcal{P}_\lambda = \mathcal{A}_\lambda \sigma_\lambda \Phi_\lambda$$

and has units of sec^{-1}-nm^{-1};

f) the *photolysis rate*, j, for a particular reaction is the integral of spectral rate over that range where $j_\lambda > 0$,

$$j = \int_{\lambda_m}^{\lambda_n} j_\lambda \, d\lambda = \int_{\lambda_m}^{\lambda_n} \mathcal{A}_\lambda \sigma_\lambda \Phi_\lambda \, d\lambda$$

where $j_\lambda > 0$ between λ_m and λ_n. The units of j are sec^{-1} (or min^{-1}).

Evaluation of the Rate Equation

While the mathematical definition of the photolysis rate is straightforward, the evaluation of the integral in (f) above is not. If the quantities $\mathcal{A}_\lambda$, σ_λ, and Φ_λ were available at a series of co-located wavelengths with wavelength spacing smaller than any details in either the flux or the cross-section spectrum, simple numerical integration would suffice for the calculation of photolytic rates. Unfortuately, such conditions are rarely the case.

First, $\mathcal{A}_\lambda$ can only be measured over a finite spectral width—the "slit-width"—and therefore, each $\mathcal{A}_\lambda$ has an associated wavelength interval, $\Delta\lambda$. Efforts to make the slit width smaller are limited by decreasing signal-to-noise ratios and too small a slit means that the signal becomes lost in the noise. Wide slits allow more energy to reach the detector, but limit the resolution—two peaks that are closer than the slit

width will be seen as one peak. This finite wavelength interval means that we can only state the spectral quantities as values averaged over each interval, and, even for spectral quantities, the spectrum is correctly represented as stair-like curves. The World Radiation Center extraterrestrial spectrum used in the JSPECTRA model is given as the irradiance (watt-m^{-2}) in a 2-nm interval defined by giving the ending wavelength. To state this spectrum in spectral irradiance units (watt-m^{-2}-nm^{-1}), the interval irradiance must be divided by the interval width to produce an average spectral value in each interval. These spectral values can be associated with the interval wavelengths in one of three ways:

1. by giving the beginning interval wavelength,
2. by giving the mid-point or center interval wavelength, or
3. by giving the ending interval wavelength.

Because of the types of calculations we will perform below, the third method—ending interval wavelength—has some advantages and is the preferred method here.

Occasionally irradiance spectra *are* represented as 'points,' for example, the spectral distributions measured in the EC chamber at UCR. That is, the spectrum is described by narrowband measurements which are only reported at widely spaced wavelengths. The wavelength abscissas most likely are at the inflection points on a spectrometer stripchart and do not have to be equally spaced. In the case of these 'points' spectra, it is common to assume that a straight line connects the points and that the area under this poly-line for any wavelength interval of any width is proportional to the spectral actinic flux in that interval. The top plot in Figure 28 compares two EC chamber spectral distributions, which are characteristic of 'points'-type specta, with the stair or 'bar'-type spectrum calculated for the UNC chamber using the JSPECTRA model. Note that in the 'points'-type spectrum, it is not possible to discern the actual resolution of the spectrum (*i.e.*, what was the slit width used in the measurement). It is *assumed* in Carter's calculation method to be infinitely small so that the curve can be interpolated to any degree desired.

A second difficulty in evaluating the photolysis rate is shown in the bottom of Figure 28: σ_λ and Φ_λ are sometimes measured with high-resolution compared to the measurement of $\mathcal{A}_\lambda$. For example, Bass's formaldehyde cross-section data were reported at steps of 0.025 nm. The entire spectrum has over 3000 points. In other cases, with less structure in the spectrum, larger and perhaps variable width intervals may be used. Or, in some cases, σ_λ may also be approximated by widely spaced 'points,' *i.e.*, narrow-band estimates located at widely spaced wavelengths. In any case, these cross-section intervals are rarely in alignment with the irradiance spectrum intervals, and therefore some form of interval matching

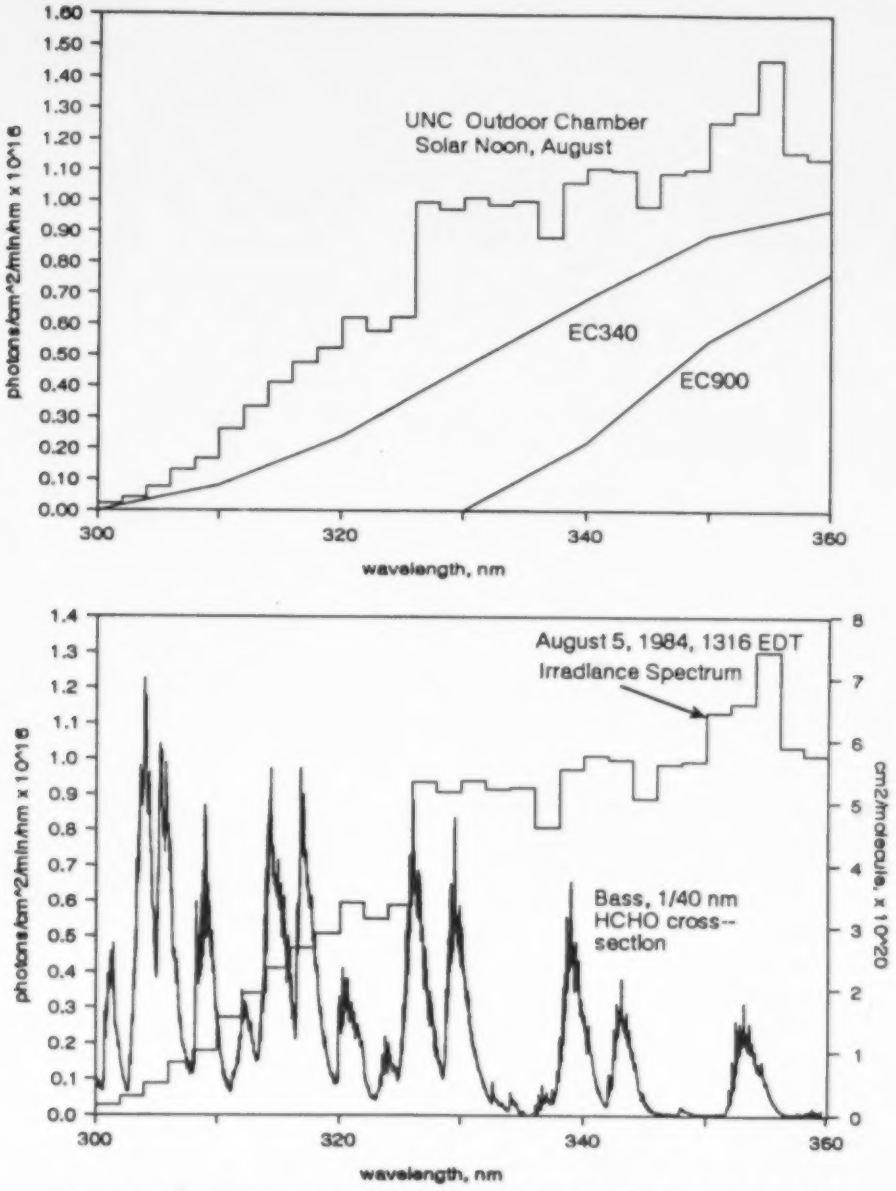

Figure 28. Illustrations of some of difficulties in evaluating the photolysis rate. Top plot: Irradiance spectra that are represented as 'bars' and as 'points' connected by lines. Bottom Plot: A mismatch in resolution between irradiance spectrum and cross-section spectrum.

must be performed between the actinic flux spectrum and most σ_λ and Φ_λ spectra. Such a case is illustrated in Figure 29 which shows the 10 nm wide intervals of RCHO's averaged reaction potential plotted over the 2-nm actinic flux. The upper and lower boundary of the reaction potential interval that is centered at 310 nm falls in the middle of an irradiance 'bar.' Clearly, something has to be divided in this case: should the irradiance interval at 314–316 nm be divided into two 1-nm 'bars' or should the reaction potential spectrum be divided into 2-nm 'bars' to match the irradiance spectrum? These questions will be examined in more detail below.

Approximation Methods

A common approximation used in evaluation of the photolysis rate integral is based upon the Mean Value theorem:

> If $f(x)$ is continuous in the interval $a \leq x \leq b$, and if the interval is divided into sub-intervals, $s_1, s_2, \ldots s_n$ by the points $x_0, x_1, \ldots x_{n-1}$, and if we denote the length of the sub-interval s_k by $\Delta_k x = x_k - x_{k-1}$ then
>
> $$\lim_{n\to\infty} \sum_{k=1}^{n} f(x_k)\Delta_k x = \int_a^b f(x)\,dx$$
>
> and similarly, upon the 'Theorem of Bliss'
>
> $$\lim_{n\to\infty} \sum_{k=1}^{n} f(x_k)g(x'_k)\Delta_k x = \int_a^b f(x)g(x)\,dx$$

Using these relationships, the integrals in the section above can be converted into summations of functions evaluated in each interval. In practice, however, we do not know the value of x_k (or x'_k) that make these relationships exact. The most common value of $f(x_k)$ used in these equations is the average of the function's end points in each interval (*i.e.*, $(f(x_k) + f(x_{k-1}))/2$)—thus the integration method becomes the trapezoid rule. We do not know of studies on how the choice of n (*e.g.*, size of $\Delta_k\lambda$) affects the accuracy of calculated photolysis rates using these approximations. Clearly attempting to represent such complex spectra as shown for HCHO in Figure 28 by 10 nm intervals, as was recommended in the NASA85 document, is likely to result in large errors when compared to smaller intervals, especially for varying irradiance spectra as occurs in outdoor situations.

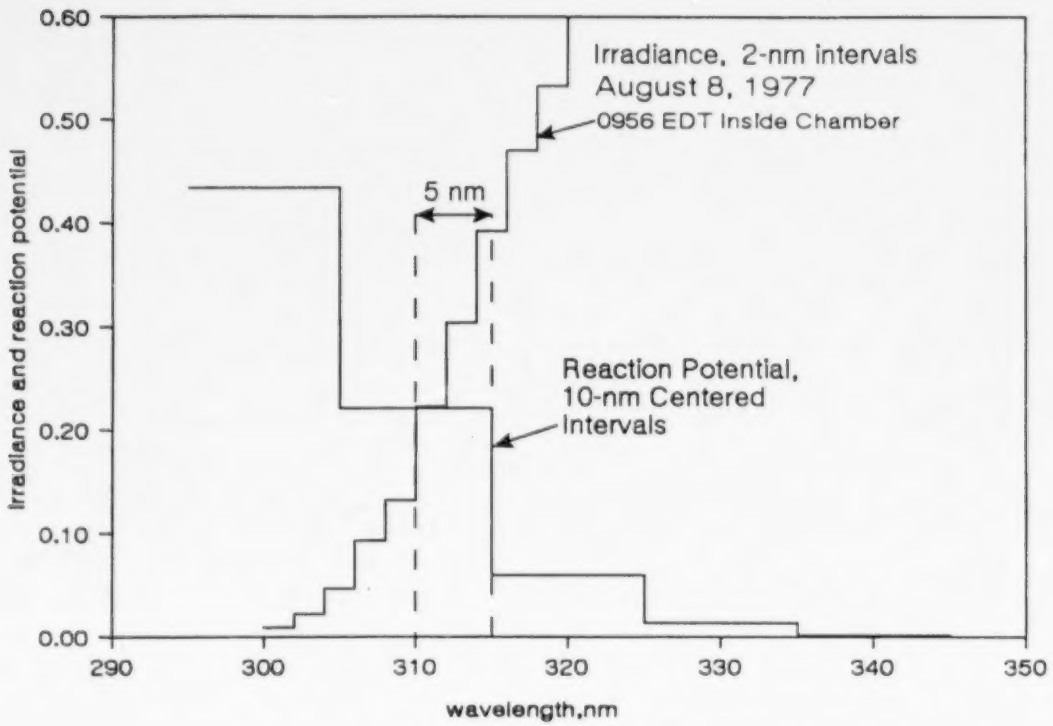

Figure 29. Example of a mismatch of irradiance and reaction potential intervals (product of cross section and quantum yield). The reaction potential is 10-nm average for RCHO.

Interval Quantities and Units

An interval quantity is a total value or an average value over some finite wavelength interval. In subsequent discussion, $\Delta_k\lambda = \lambda_k - \lambda_{k-1}$. Names and units of the interval quantities we use are:

a) *interval actinic flux*, $\overline{\mathcal{A}_\lambda}\Delta_k\lambda$, has units of photons-cm^{-2}-sec^{-1} and is defined for the k^{th} interval as

$$\overline{\mathcal{A}_\lambda}\Delta_k\lambda = \int_{\lambda_{k-1}}^{\lambda_k} \mathcal{A}_\lambda \, d\lambda$$

b) *interval averaged reaction potential*, $\overline{\mathcal{P}_{\Delta_k\lambda}}$, has units cm^2-molecule^{-1} and is defined for the k^{th} interval as

$$\overline{\mathcal{P}_{\Delta_k\lambda}} = \frac{\int_{\lambda_{k-1}}^{\lambda_k} \sigma_\lambda \Phi_\lambda \, d\lambda}{\Delta_k\lambda}$$

c) *interval photolysis rate*, $j_{\Delta_k\lambda}$, for the k^{th} interval is

$$j_{\Delta_k\lambda} = \overline{\mathcal{A}_\lambda}\Delta_k\lambda\overline{\mathcal{P}_{\Delta_k\lambda}} \approx \int_{\lambda_{k-1}}^{\lambda_k} \mathcal{A}_\lambda \sigma_\lambda \Phi_\lambda \, d\lambda$$

and it has units of sec^{-1} (or min^{-1})

d) therefore, an alternative definition of photolysis rate is

$$j = \sum_{k=m}^{n} j_{\Delta_k\lambda}$$

where m is the first interval and n is the last in which $j_{\Delta_k\lambda} > 0$.

If spectral irradiances are plotted as in plot A of Figure 30, the *area* in each interval is directly proportional to the total irradiance in the interval. If each irradiance area is weighted by an average $\sigma_\lambda\Phi_\lambda$ (*i.e.*, the *height* in each interval of plot B is proportional to the average) for the *same* intervals as in plot A of Figure 30, then each product bar's area becomes proportional to the interval rate, $j_{\Delta_k\lambda}$ as in plot C of Figure 30, and the total area under all the bars would be proportional to the total photolysis rate, as in plot D of Figure 30. Thus, the task of evaluating the rate integral becomes one of matching intervals between the irradiance spectrum and the reaction potential spectrum. This must be done differently for different combinations of spectrum types.

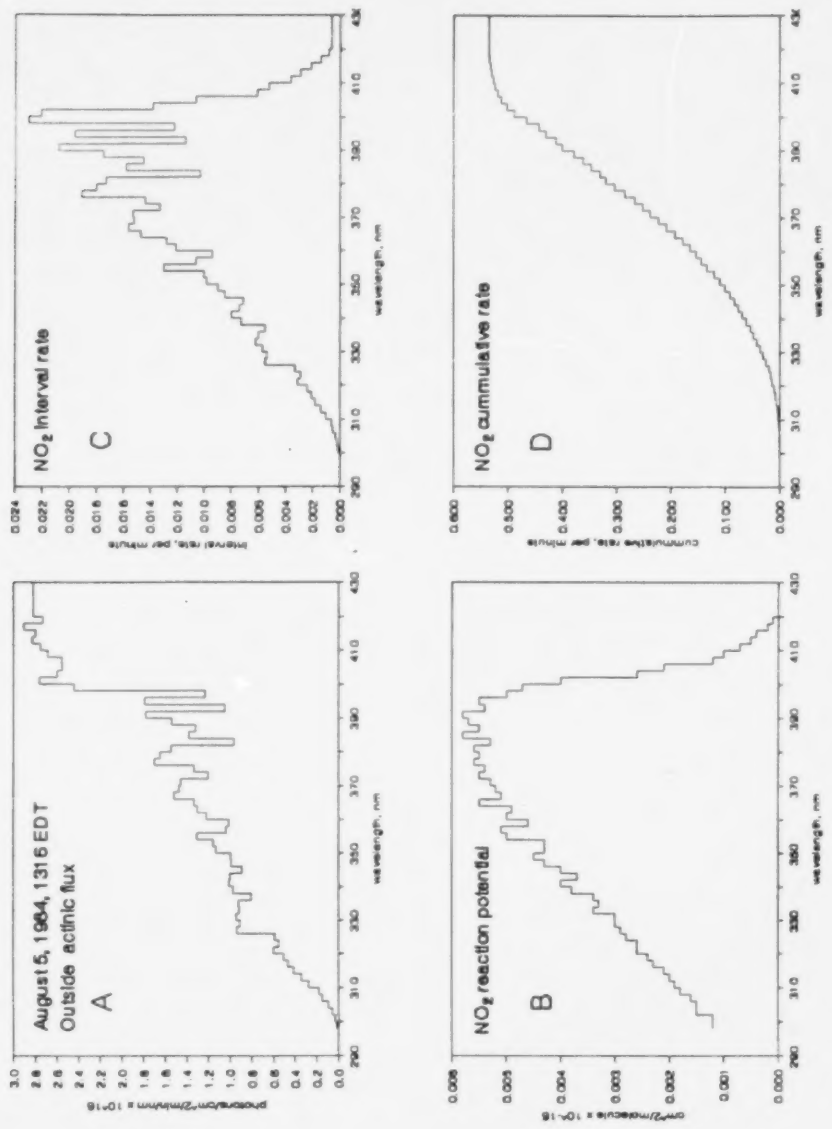

Figure 30. The interval components in the calculation of the NO_2 photolysis rate. A: the surface spectral spherical irradiance spectrum; B: the interval averaged NO_2 reaction potential spectrum at the same intervals as A; C: the interval photolysis rate; D: the cummulative sum of C which is the NO_2 photolysis rate for this time and location.

Combinations of Spectrum Types

There are four combinations of irradiance spectra types and reaction potential spectra types; these are shown in Figure 31. Here we are mainly concerned for the cases in which the irradiance spectra are 'bar'-type spectra. This is because, as described in the previous chapter, the main output from the in-chamber actinic flux program is a table of ending-interval wavelengths, λ_k, and variable-width, interval actinic fluxes, $\overline{\mathcal{A}_\lambda}\Delta_k\lambda$ (units of photons-cm^{-2}-min^{-1}), that is the total actinic flux from λ_{k-1} to λ_k. The interval widths are variable from 2-nm in the ultraviolet to 10, 20, and 40-nm over the visible and near infrared. Thus, for UNC in-chamber calculations, we need only be concerned with 'bar-bar' and 'bar-line' combinations shown in Figure 31.

We will assume that the resolution of the irradiance spectrum is always the limiting factor (*i.e.*, calculation at a finer resolution than the irradiance spectrum would result in no change in the final rate), and, thus 'bar'-type reaction potential spectra, either of higher resolution or lower resolution, will be interpolated to agree with the irradiance intervals. That is, the reaction potential interval boundaries must be re-interpolated to coinside with the interval boundaries of the irradiance spectrum. This process of computing interval averages on arbitary boundaries is easier if 'bar'-type input reaction potential spectra are first integrated as a function of wavelength. Then new interval-average reaction potential 'bars'—aligned with the irradiance 'bars'—can be readily calculated by a difference in linearly interpolated values of the integrated function at any pair of wavelengths divided by the interval width.

The other three combinations shown in Figure 31 all require a form of double trapezoid integration (which we will derive below). This procedure is applied to trapezoidal panels created by the union of the inflection points from both spectra. The only case we are concerned with here, however, is the irradiance 'bar' and reaction potential 'line' case. For these conditions, 'bar'-type spectra are treated as if an inflection point occurs at each end of each 'bar' and a degenerate form of the double trapezoid rule can still be applied.

First, we will describe the interval averaging technique, then the double trapezoid rule.

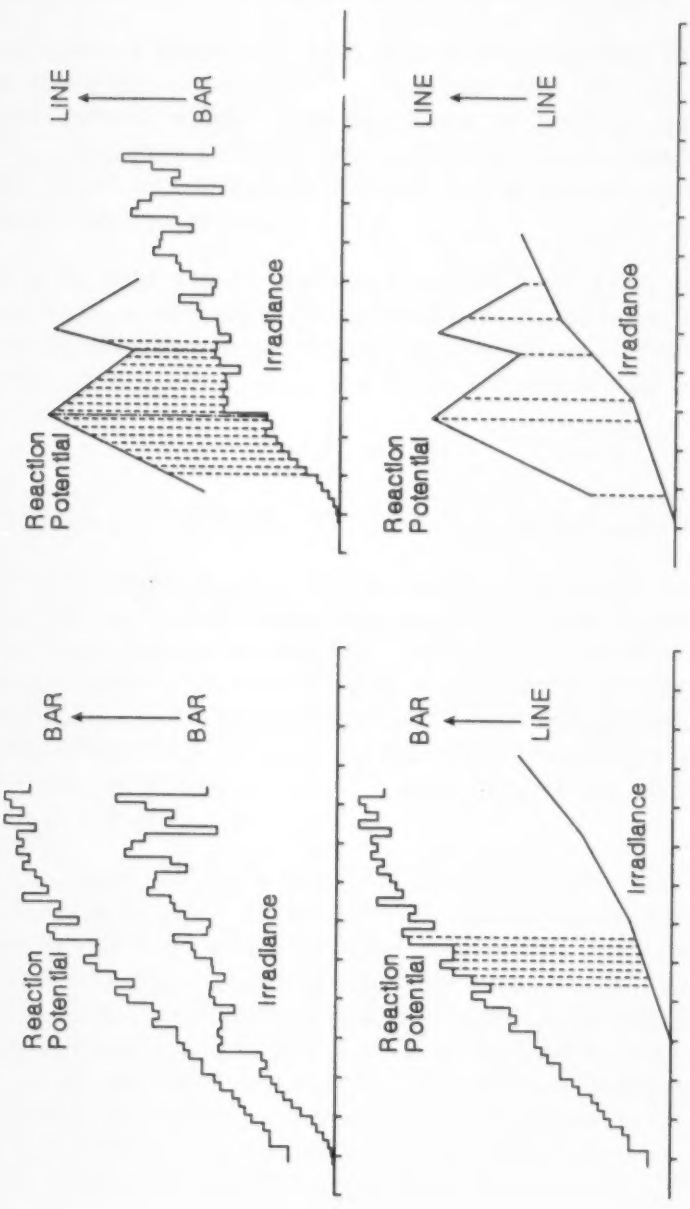

Figure 31. The combinations of irradiance and reaction potential spectrum types. The dashed lines indicate that interpolation of the line spectra is needed.

Computing Interval-Averaged Reaction Potential

This section describes a simple and rapid method for computing $\overline{\mathcal{P}_{\Delta_k\lambda}}$ at variable $\Delta_k\lambda$, or even where the cross-section and quantum yield intervals are at ad-hoc wavelengths and interval widths. Two algorithms are used to compute $\overline{\mathcal{P}_{\Delta_k\lambda}}$: a variable-method integration technique, and a rapid-search interpolation routine for use when a table must be searched many times and the abscissa each time is close to its value on the previous search.

The σ_λ and Φ_λ data may be available in several forms (*e.g.*, point-values, or interval-averaged values with one of the three different ways of specifying the wavelengths associated with the average, beginning, centered, or ending). In the 'bar' type calculations, all input forms of σ_λ and Φ_λ are converted to an integrated form

$$I_\lambda = \int_0^\lambda \sigma_\lambda \Phi_\lambda \, d\lambda$$

and stored as a table of (λ, I_λ) pairs. The units of I_λ are cm^2-molecule^{-1}-nm.

Slightly different methods are needed to calculate the integral in this equation, depending upon the input form (beginning, centered, ending intervals) of σ_λ and Φ_λ. For all 'bar' cases, first the product $\sigma_\lambda\Phi_\lambda$ is formed (*i.e.*, we assume that σ_λ and Φ_λ are compatible within each interval), then a rectangular-rule (height×interval-width) is used to perform the panel integration. The wavelength values associated with each I_λ are always the λ values at the end of the interval. For λ less than the first λ in the input, we assume $I_\lambda = 0$. The upper-limit of the (λ, I_λ) table is the first λ at which $\sigma_\lambda = 0$ or $\Phi_\lambda = 0$.

In calculating rates, we search this (λ, I_λ) table to locate a bounding interval for a given λ in a highly correlated manner (*i.e.*, increasing λ), and therefore the calculation can benefit from an interpolation method that has a 'memory.' The slowest method for finding a bounding interval is linear search, *i.e.*, compare the input λ with each table λ starting at the first value in the (λ, I_λ) table each time. For totally un-correlated input λ, bisection is a fast method for locating the bounding interval. Because the interval widths in the (λ, I_λ) table may be highly variable and because our input λs *are* correlated, a 'hunt' from the previous point followed by a bisection phase, if needed, is an optimum method. This technique, adopted from Press, *et al.*, "Numerical Recipes, The Art of Scientific Computing,"[16] is illustrated in Figure 32.

Using this hunt-find location method, one finds the index of the bounding wavelength interval $(i-1, i)$ for a given wavelength, λ_o, such that

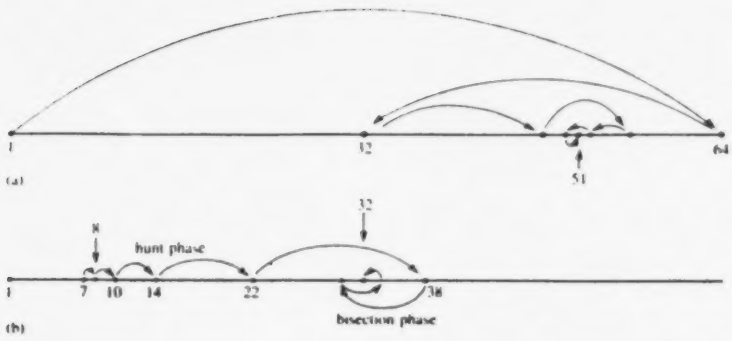

Figure 32. Example of 'hunt' algorithm for locating bounding interval in a one-way table. Top: bisection only, shown is the sequence of steps that converge to element 51 in a table of length of 64. Bottom: Hunt routine searches from a previously known position in the table by increasing steps, then converges by bisection. Shown here is a particularly unfavorable example, converging to element 32 from element 7. A favorable example would be convergence to an element near 7, such as 9, which would require just three "hops."

$$\lambda(i-1) \leq \lambda_o < \lambda(i)$$

Then we can linearly interpolate a value of I_λ at λ_o by

$$u = \frac{\lambda_o - \lambda(i-1)}{\lambda(i) - \lambda(i-1)}$$

and

$$I_{\lambda_o} = (1-u)I_\lambda(i-1) + uI_\lambda(i)$$

This value is a good approximation of

$$I_{\lambda_o} = \int_0^{\lambda_o} \sigma_\lambda \Phi_\lambda \, d\lambda$$

The integral average product of the cross-section and quantum yield, $\overline{\mathcal{P}_{\Delta_k\lambda}}$, for an interval defined by $(\lambda_{k-1}, \lambda_k)$ is computed by

$$\overline{\mathcal{P}_{\Delta_k\lambda}} = \frac{\int_{\lambda_{k-1}}^{\lambda_k} \sigma_\lambda \Phi_\lambda \, d\lambda}{\Delta_k\lambda} = \frac{\int_o^{\lambda_k} \sigma_\lambda \Phi_\lambda \, d\lambda - \int_o^{\lambda_{k-1}} \sigma_\lambda \Phi_\lambda \, d\lambda}{\lambda_k - \lambda_{k-1}}$$

which we approximate by

$$\overline{\mathcal{P}_{\Delta_k\lambda}} = \frac{I_{\lambda_k} - I_{\lambda_{k-1}}}{\lambda_k - \lambda_{k-1}}$$

where I_{λ_k} and $I_{\lambda_{k-1}}$ are computed by the linear interpolation method described above. Note that $\overline{\mathcal{P}_{\Delta_k\lambda}}$ has units of cm^2-molecule^{-1}.

When the two wavelengths λ_{k-1} and λ_k are the beginning and ending bounds of a spectral actinic flux interval, $\overline{\mathcal{P}_{\Delta_k\lambda}}$ is the exact value needed to compute the interval rate, $j_{\Delta_k\lambda}$, for this interval

$$\begin{aligned} j_{\Delta_k\lambda} &= \overline{\mathcal{A}_\lambda}\Delta_k\lambda\,\overline{\mathcal{P}_{\Delta_k\lambda}} \\ &= (\text{photons-cm}^{-2}\text{-sec}^{-1})(\text{cm}^2\text{-molecule}^{-1}) \\ &= \text{sec}^{-1} \end{aligned}$$

Computing Double Trapezoidal Integrals

We need a method to compute

$$j_{\Delta_k\lambda} = \int_{\lambda_{k-1}}^{\lambda_k} \mathcal{A}_\lambda \sigma_\lambda \Phi_\lambda \, d\lambda$$

when both $\mathcal{A}_\lambda$ and $\sigma_\lambda \Phi_\lambda$ are represented by 'points' and the height of the connecting line at any wavelength is *assumed* to represent the irradiance or the reaction potential at that wavelength. If the lines in each interval are represented in the standard slope-intercept form, *e.g.*,

$$f_i = m_i\lambda + b_i$$

for irradiance and

$$r_i = p_i\lambda + d_i$$

for reaction potential

then

$$\begin{aligned} j_i &= \int_{\lambda_{i-1}}^{\lambda_i} (m_i\lambda + b_i)(p_i\lambda + d_i)\,\Delta\lambda \\ &= (1/2)(m_ip_i)\lambda^3 + (m_id_i + p_ib_i)\lambda^2 + b_id_i\lambda\Big|_{\lambda_{i-1}}^{\lambda_i} \end{aligned}$$

which is a difficult equation in terms of evaluation considering that all the m_i, b_i, p_i, and d_i's have to be computed and stored.

An easier method is illustrated in Figure 33. In this figure assume the bold solid lines represent the irradiance spectrum and the bold dashed lines represent the reaction potential. The points that define each are shown as circles and are labeled as A1..A5 and B1..B8. Vertical lines have been dropped from the points to the x-axis to create trapezoid panels. What we desire, however, are trapezoid panels in each spectrum that have the same base interval (*e.g.*, the first panel would have a base of B1 to A2, the second would be A2 to B2, and so forth). We construct these new points by interpolating one spectrum at the location of the defining points of the other and vice versa. These interpolated points are shown in Figure 33 as triangles. Thus we need to know the height (a) of the line connecting A1 and A2 at abscissa B1 and likewise the height (d) of the line connecting B1 and B2 at abscissa A2. This is most easily done using a parametric representation of the point connecting line defined by

$$\begin{aligned} \lambda_{i-1} \le \lambda \le \lambda_i \\ 0 \le t \le 1 \end{aligned}$$

which leads to

$$\lambda = (1-t)\lambda_{i-1} + (t)\lambda_i$$

or

$$t = \frac{\lambda - \lambda_{i-1}}{\lambda_i - \lambda_{i-1}}$$

Let

$$a = \mathcal{A}_\lambda(\lambda_{i-1}) \qquad b = \mathcal{A}_\lambda(\lambda_i)$$

and

$$c = \sigma_\lambda \Phi_\lambda(\lambda_{i-1}) \qquad d = \sigma_\lambda \Phi_\lambda(\lambda_i)$$

and a, b, c, and d may be either given or interpolated. We can now define simple equations for the flux and the reaction potential anywhere within the i^{th} interval.

$$\mathcal{A}_\lambda = (1-t)a + tb \qquad \text{and} \qquad \mathcal{P}_\lambda = (1-t)c + td$$

These equations can now be substituted for $\mathcal{A}_\lambda$ and $\mathcal{P}_\lambda$ in the definition of j_{λ_k},

$$j_{\lambda_k} = \int_{\lambda_{k-1}}^{\lambda_k} \mathcal{A}_\lambda \mathcal{P}_\lambda \, d\lambda$$

and knowing that

$$d\lambda = dt(\lambda_i - \lambda_{i-1})$$

then substituting a, b, c, d gives

$$\begin{aligned} j_{\lambda_k} &= \int_{t=0}^{t=1} ((1-t)a + tb)((1-t)c + td)\, dt(\lambda_i - \lambda_{i-1}) \\ &= [(1/3)(ac + bd) + (1/6)(ad + bc)]\,(\lambda_i - \lambda_{i-1}) \end{aligned}$$

The last equation is the definition of the *Double Trapezoid Rule*.

Let us calculate the error produced by a common procedure in which (a) the actinic flux spectrum is averaged by the trapezoid rule and (b) the reaction potential spectrum is averaged by the trapezoid rule and (c) the two averages are used to estimate the product (*i.e.*, the interval rate) compared with using the double trapezoid rule to compute the interval rate directly. One of the worst cases is shown in Figure 34.

In this figure only one interval of a whole spectrum is shown, and in this particular interval the flux spectrum is decreasing (1 in Figure 34) while the reaction potential spectrum is increasing (2). Let us assume that the height of a and d are each 2.0 units and that $(\lambda_2 - \lambda_1) = 1.0$. Then the application of the trapezoid rule to 1 and 2 would yield

$$\begin{aligned} \overline{\mathcal{A}_\lambda}\Delta_k\lambda &= (1/2)(a+b)(\lambda_2 - \lambda_1) \\ &= (1/2)a\Delta\lambda \\ \overline{\mathcal{P}_{\Delta_k\lambda}} &= (1/2)(c+d) \\ &= (1/2)d \end{aligned}$$

therefore

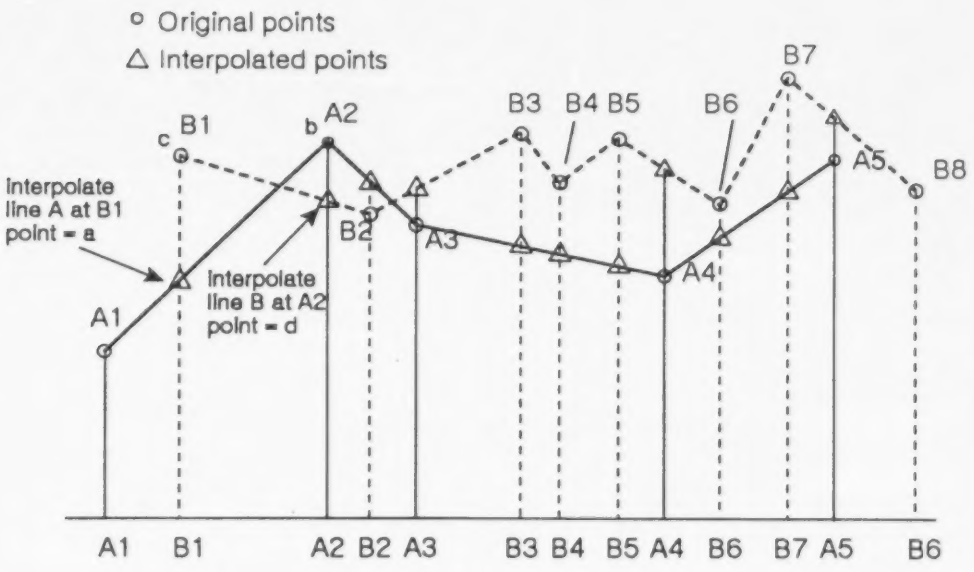

Figure 33. The double trapezoid rule method.

$$j_{\Delta_\star\lambda} = (1/4)(ad)\Delta\lambda$$
$$= (1/4)(4)1 = 1.0$$

That is, the average area in each spectral interval is 1.0 unit and therefore the product spectrum would have 1.0 unit of area.

The double trapezoid rule, however, gives

$$j_{\Delta_\star\lambda} = [(1/3)(ac + bd) + (1/6)(ad + bc)](\lambda_2 - \lambda_1)$$
$$= (1/6)(ad)\Delta\lambda$$
$$= (1/6)(4)1 = 0.666$$

That is, the product of the averages based upon the simple trapezoid rule is too large by a factor of 1.5 for this worse case condition.

For 'bar'-type irradiance spectra this problem can not arise, because we have no knowledge of how the irradiance spectrum might change *within* an interval, but

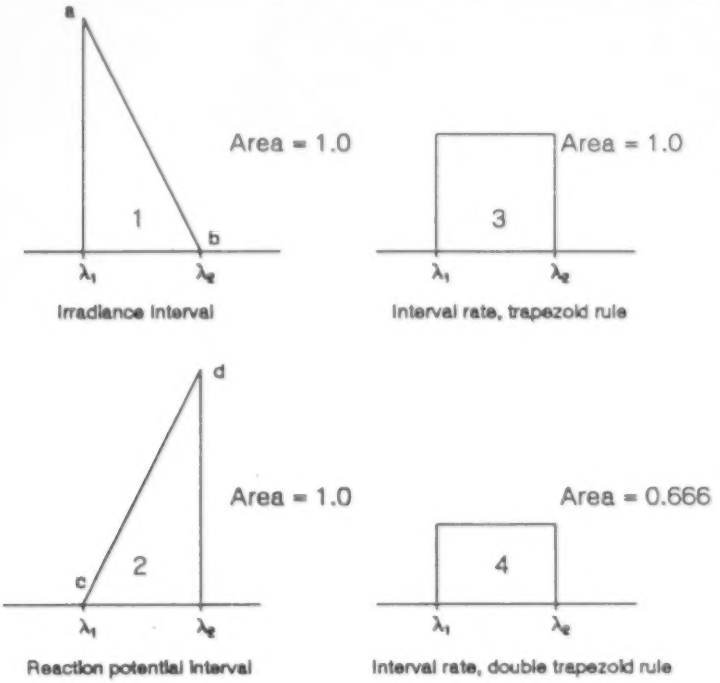

Figure 34. Comparison of simple trapezoid rule applied twice and the direct use of the double trapezoid rule. (1) represents a flux spectrum interval; (2) represents a matching reaction potential interval; (3) is the calculated interval rate and is the result of applying the simple trapezoid rule to 1 and 2 and then computing the product; (4) is the correct calculated interval rate and is the result of applying the double trapezoid rule to 1 and 2. The error in the first procedure is 50%.

only know the average height in the interval. Thus we have no choice but to form the product of the average irradiance with the average reaction potential. Higher resolution spectra are the only way to improve the accuracy of the calculations.

Problems with Sources of Photolytic Data

When examining the recommendations for photolysis cross sections and quantum yields given in reviews such as Atkinson and Lloyd[17] or NASA85, it is difficult to determine the proper form of the data presented.

For example, in the Atkinson and Lloyd review, the NO_2 σ_λ data were given with a heading of "NO_2 Absorption Cross-Sections at 298 K, as recommended by NASA" with no information as to whether these data, which were presented every 5 nm from 280 to 410 nm, were 'point' values or interval averaged values. In a later table for NO_3, however, the table caption clearly states, "Absorption Cross Sections (cm^2-$molecule^{-1}$, base e), Averaged Over Each nm, for NO_3." But this table does not say if the intervals are centered on the wavelengths or at the beginning of the interval. For HONO the Atkinson and Lloyd table says "Absorption Cross Sections as Recommended by NASA." and the data are given every nanometer. For HNO_3 the data are given every 5 nm. Are these averaged over the 5-nm interval? Are they point values at the given wavelengths? Consulting the NASA document is little help in these cases: it says nothing about the form of the data. One must go to the original sources and see how the authors collected the data. In the case of HCHO, the NASA document and Atkinson and Lloyd clearly indicate at the bottom of the table that the cross section values are the average of Bass and Moortgat and are "averaged over 10 nm intervals centered at the indicated wavelength." Clearly, in this case, it would be inappropiate to treat these data as points, as was done by Carter in the CAL development work. In his most recent work, Carter still uses the 'points' treatment on all spectra, but he now uses a 1-nm averaged HCHO spectrum, and so the points treatment does not add as much error as it did for the 10-nm points.

Molina and Molina,[18] are a good example of clear and explicit statements about the spectral conditons in their cross section data on ozone. They state,

> "The spectral resolution of the Cary 219 is 0.07 nm ... the slit was kept at 0.07 nm with a scanning rate of 0.02 nm-s^{-1}"

In the listing of the cross section data they clearly state that the intervals are 0.5 nm. These are clearly 'point' data in that each point has a $\Delta\lambda$ of 0.07 nm, and they are spaced at 0.5 nm.

Methodology for Rate Calculation

Case: Reaction Potential Spectra as Bars

Assume the CHMRATE program described in the first chapter was used to calculate sets of actinic flux and that one of these sets has been read and stored in a table of wavelengths and interval actinic fluxes which we will represent as (λ, F_λ). Likewise, assume the first part of the procedure for computing interval averages for reaction potential spectra—the integration of the reaction potential spectrum—has been performed, and that the results are also stored in a table represented by (λ, I_λ). These two tables most likely have different values for the λs in each. For most conditions, the limiting factor for accurate calculation of photolysis rate is the irradiance spectrum resolution. Therefore, the density of our calculations will be that of the irradiance spectrum. This means that there is no interpolation of the irradiance spectrum, but the reaction potential $(\sigma_\lambda \Phi_\lambda)$ will have to be (re-)averaged over the same interval as the irradiance spectrum intervals. The interval averaging algorithm described above does this correctly, accounting for all of the spectral detail in the cross- section spectrum.

The steps in the method are:

1) Find the first index of (λ, F_λ) table such that the indexed λ is equal to or greater than the first λ in (λ, I_λ); call this k.
2) Find the first index of (λ, I_λ) table such that the indexed λ is equal to or greater than the first λ in (λ, F_λ); call this i.
3) Let lambda-hi be the wavelength from the k^{th} row of (λ, F_λ), and lambda-low be the wavelength from the $(k-1)$ row of (λ, F_λ). Similarly, let F-hi be the flux value from the k^{th} row of (λ, F_λ).
4) The interval actinic flux for this interval is

$$\overline{\mathcal{A}_\lambda} \Delta_k \lambda = \text{F-hi}.$$

5) Using the lambda-low and lambda-hi from the flux spectrum interval, and starting at the i^{th} location in (λ, I_λ), use the 'hunt-find' procedure to calculate the I_λ values that correspond to lambda-low and lambda-hi. Let these be P-low and P-hi. Also, as part of 'hunt-find' procedure, up-date the value of i to index the current interval in (λ, I_λ).
6) Compute the interval averaged reaction potential by

$$\overline{\mathcal{P}_{\Delta_k \lambda}} = \frac{\text{P-hi} - \text{P-low}}{\text{lambda-hi} - \text{lambda-low}}$$

7) Compute the interval photolysis rate for this interval by

$$j_{\Delta_k\lambda} = \overline{A_\lambda}\Delta_k\lambda\,\overline{P_{\Delta_k\lambda}}$$

8) Compute the total photolysis rate over the whole spectrum by incrementing k and repeating steps 3–7. This is equivalent to

$$j = \sum_{k=m}^{n} j_{\Delta_k\lambda}$$

where m is the index of the lowest interval in which $j_{\Delta_k\lambda} > 0$ and n is the index of the highest interval in which $\overline{P_{\Delta_k\lambda}} > 0$.

This method is implemented as the BarBarRate procedure in the CHMRATE Pascal program listed in Appendix E.

Case: Reaction Potential Spectra as Points

As above assume the CHMRATE program was used to calculate sets of actinic flux and that one of these sets has been read and stored in a table of wavelengths and interval actinic fluxes which we will represent as (λ, F_λ). In this case, however, the reaction potential spectrum has been stored *un-modified* in a table which we will also represent by (λ, I_λ). That is, the contents of (λ, I_λ) are the wavelengths and the point values of the reaction potential at the wavelengths. As in the first case, these two tables most likely have different values for the λs. Here, however, we will calculate product areas that are bounded by the union of the wavelengths in the irradiance spectrum and the reaction potential spectrum. Even though the irradiance spectrum is a 'bar'-type spectrum, we can treat each bar it as if it were a line connecting the two end points and for which a=b in the double trapezoid rule. This allows a number of otherwise special conditions to be dispensed with in a straight forward manner (*e.g.*, a reaction potential inflection point in the middle of an irradiance 'bar' interval). The steps in this method are:

1) Find the first index of (λ, F_λ) table such that the indexed λ is equal to or greater than the first λ in (λ, I_λ); call this k.
2) Find the first index of (λ, I_λ) table such that the indexed λ is equal to or greater than the first λ in (λ, F_λ); call this i.
3) Let lambda-low be the wavelength from the $(k-1)$ row of (λ, F_λ). Similarly, let F-hi be the flux value from the k^{th} row of (λ, F_λ).

4) Both a and b are equal to the height of the irradiance bar, but F-hi is the area in the bar, so compute an average height

$$a \text{ and } b = \text{F-hi}/(\text{lambda-hi} - \text{lambda-low}).$$

5) Using lambda-low from the irradiance spectrum interval, and starting at the i^{th} location in (λ, I_λ), use the 'hunt-find' procedure to calculate the I_λ value that correspond to lambda-low. Let this be c in the double trapezoid rule. Also, as part of 'hunt-find' procedure, up-date the value of i to index the current interval in (λ, I_λ).

6) Examine the next interval boundary in both (λ, F_λ) and (λ, I_λ) tables and decide which spectrum has the next wavelength greater than lambda-low; let this wavelength be lambda-hi. If the wavelength is the end of the irradiance bar, then use the 'hunt-find' procedure to interpolate the reaction potential spectrum at lambda-hi and call the value d in the double trapezoid rule, else assign the value of the reaction potential stored in the i^{th} row of (λ, I_λ) to d in the double trapezoid rule.

7) Compute the interval photolysis rate for this interval by

$$\begin{aligned} j_{\Delta_k\lambda} &= (1/3)(ac + bd) + (1/6)(ad + bc)(\text{lambda-hi} - \text{lambda-low}) \\ &= (a)(1/2)(c + d)(\text{lambda-hi} - \text{lambda-low}) \end{aligned}$$

8) Compute the total photolysis rate over the whole spectrum by letting $c = d$ and lambda-low = lambda-hi; if lambda-low is greater or equal to the k^{th} wavelength in (λ, F_λ) then increment k and repeat steps 3–7. This is equivalent to

$$j = \sum_{k=m}^{n} j_{\Delta_k\lambda}$$

where m is the index of the lowest interval in which $j_{\Delta_k\lambda} > 0$ and n is the index of the highest interval in which $\overline{P_{\Delta_k\lambda}} > 0$.

This method is implemented as the **BarLineRate** procedure in the CHMRATE Pascal program listed in Appendix E.

Practical Considerations

Data Input Formats

The irradiance spectrum is a binary file produced by the CHMJMOD program and has a fixed number of spectral intervals for which the interval actinic flux is given with the wavelength at the end of the interval. It is read into the (λ, F_λ) table directly. The cross section and quantum yield spectra, however, can be of several forms:

- **P**–points, use straight lines to connect
- **B**–interval averaged values, beginning of interval wavelength
- **C**–interval averaged values, center of interval wavelength
- **E**–interval averaged values, end of interval wavelength

where the bold letter is used as a code in the file header to indicate to the program the form of the data.

The CHMRATE program, following a convention established by Carter, ignores lines that begin with a '!' in column 1, as well as blank lines. In **P**oint data, the data part of the file includes just the points, one set of wavelength and values per line. In **B**eginning data, the data part of the file should include an *additional final line* that has the next logical wavelength and values of zero. This is because on reading the data, each newly read wavelength is associated with the previous values (the first wavelength in a beginning interval file is the ending wavelength for the values that came before the file's first point, which are assumed to be zero). In **E**nding data, the data part of the file should include an *additional initial line* that has the logical ending wavelength of a previous interval and values of zero. Similarly, for **C**entered data, the data part of the file should include an *additional initial line* that has a wavelength such that the difference between it and the next wavelength is the interval width of the first real interval. The values associated with this additional first line should be zero. In summary,

- point data have no extra lines
- beginning interval data have an extra last line
- ending and centered data have an extra first line

In addition to the data, a reaction potential spectral file can contain FAC= commands that specify a scale factor to multiply the product of the cross section and quantum yield. Finally, if the quantum yield is missing in the file, then it is assumed to be 1.0.

An example of a cross section and quantum yield file is shown in Table 4.

Table 4. Example of a cross section and quantum input file. Lines beginning with '!' are ignored. The first line is a title line. The first column is the wavelength in nanometers, the second column is the cross section, and the third column is the quantum yield.

```
C2CHO
! CAL reaction:
!   RCHO + HV = C2-O2. + RO2. + CO + HO2.
Points
!units are (cm^2/molecule)
!
280  5.26E-20  0.96
290  5.77E-20  0.91
300  5.05E-20  0.86
310  3.68E-20  0.60
320  1.66E-20  0.36
330  6.49E-21  0.20
340  1.44E-21  0.08
345  0.0       0.02
```

CHMRATE Program Commands

The CHMRATE program has seven commands in three groups. Group 1 commands set up input and output paths for finding and creating files:

- **IRRDefault**—set the directory path to the irradiance or actinic flux files.
- **CQDefault**—set the directory path to the cross section and quantum yield files.
- **LIXDefault**–set the directory path at which the output files will be placed; if command not given, place output *.LIX files in same directory as input *.FIB files.

Group 2 commands identify input fluxes and cross section data:

- **CsQy**—followed by name of file containing the $\sigma_\lambda \Phi_\lambda$.
- **Single**–(optional) followed by a time in EDT to specify a single actinic flux spectrum as a source.
- **IRRA**—followed by the name of file containing sets of actinic flux. After reading a flux from file, the photolysis rate of all species read by CsQy are calculated and written to the output file.

Group 3 is a single command:

- **Exit**—used to stop the program.

In addition, any part of the command file can be placed in a second file and the second file can be 'called" from the first file by beginning a line with '@" followed by the second filename. After the second file has been read, reading continues with the first file. This allows lists of input files for cross sections and for fluxes to be maintained.

Examples of two command files are given in Table 5 and Table 6. The first command file computes all the rates for the Carbon Bond Four Mechanism for all the current SegFiles. The list files refered to in the example are given in Table 7 and Table 8.

Appendix C lists all CsQy files used by UNC as of June, 1988.

Table 5. Example of a CHMRATE command file.

```
!This is a cmdfile for CHMRATE
!It assumes it is run from SegFile disk.

! Set locations of input file directories
CQdefaultdir=\csqydata
IRRdefaultdir=\segfiles

!The list file below has al'
! CsQy commands to read (  ss-section+quantum yield
! file for species in CB4 (see table next page)

@\csqydata\cb4rxn.lst

!The list file below has all
! IRRAD commands to read a chamber solar spectrum file which has
! a series of arrays of fluxes and then to calculate rates using
! CsQy above.  (see table next page)

@\csqydata\allfib.lst

exit
```

Table 6. Example two of a CHMRATE command file.

```
!This is a cmdfile for CHMRATE
! It assumes it is run from the SegFile disk.

CQdefaultdir=\csqydata
IRRdefaultdir=\segfiles
LIXdefaultdir=e:\lix

@\csqydata\calrxn.lst

! Perform a single rate calculation using the flux at
!  0958 EDT in the following IRRadiance file.
Single=0958
Irrad=77\au0977.fib

exit
```

Table 7. Example of an external list file of CsQy commands for CHMRATE.

```
!CB4RXN.LST as of June 1988
CsQy=NO2.CQY
CsQy=NO3NO.CQY
CsQy=NO3NO2.CQY
CsQy=HONO.CQY
CsQy=O3O1D.CQY
CsQy=O3O3P.CQY
CsQy=H2O2.CQY
CsQy=HCHOBASR.CQY
CsQy=HCHOBASM.CQY
CsQy=CCHO.CQY
CsQy=GLY1.CQY
CsQy=GLY2.CQY
CsQy=MEGLY1.CQY
CsQy=MEGLY2.CQY
```

Table 8. Example of an external list file of IRRAD commands for CHMRATE program.

```
!This file lists all flux in-chamber binary files (*.FIB)
!  as of June 1, 1988
IRRAD=77\MY1877.FIB
IRRAD=77\JN0377.FIB
 ...
 ...
 ...
IRRAD=85\AU2985.FIB
IRRAD=86\JL0986.FIB
IRRAD=86\JL1386.FIB
```

References

1 Parrish, D.D., P.C. Murphy, D.L. Albritton, F.C. Fehsenfeld, "The Measurement of the Photodissociation Rate of NO_2 in the Atmosphere," *Atmos. Environ.* **17** pp 1365-1378, 1983.

2 Blackburn, T.E., "Solar Photolysis of ozone to singlet D oxygen atoms," Ph.D. Thesis, University of Michigan, 1984.

3 Peterson, J.T.,"Calculated Actinic Fluxes for Air Pollution Photochemistry Applications," EPA-600/4-76-002, U.S. Environmental Protection Agency, Research Triangle Park, NC, 1976.

4 Dave, J.V.,"Development of Programs for Computing Characteristics of Ultraviolet Radiation," Final Report, NAS5-21680, NASA Report CR-139134, National Aeronautics and Space Administration, Goddard Space Flt. Ctr., Greenbelt, MD, 1971.

5 Iqbal, M., "An Introduction to Solar Radiation," Academic Press, NY, 1983.

6 Bird, R.E. and C. Riordan, "Simple Solar Spectral Model for Direct and Diffuse Irradiance on Horizontal and Tilted Planes at the Earth's Surface for Cloudless Atmospheres," *J. Clim. and Appl. Metero.*, **25**, pp 87–97, 1986.

7 Justus, C.G. and M.V. Paris, "A Model for Solar Spectral Irradiance and Radiance at the Bottom and Top of a Cloudless Atmosphere," *J. Clim. and Appl. Metero.*, **24**, pp 193–205, 1985.

8 Brine, D.T. and M. Iqbal, "Diffuse and Global Solar Spectral Irradiance Under Cloudless Skies,"*Solar Energy*, **30**, pp 447–453, 1983.

9 Jeffries, H.,"A Simple Model for Computing Solar Spectral Irradiance and Spectral Spherical Irradiance at the Earth's Surface,", Department of Environmental Sciences, University of North Carolina, 1988.

10 Barkstrom, Bruce, "What Time Does the Sun Rise and Set?", *BYTE*, 6, No. 7, p 94, July 1981

11 Shettle, E.P. and R.W. Fenn, "Models for the aerosols for the lower atmosphere and the effects fo humidity variations on their optical properties," AFGL-TR- 79-0214, 1979

12 Peterson, J.T., E.C. Flowers, G.J. Berri, C.L. Reynolds, J.H. Rudisill, "Atmospheric Trubidity over Central North Carolina," *J. Appl. Metero.* **20**, pp 229–241, 1981.

13 Sherry, J.E. and C.G. Justus, "A Simple Hourly Clear-Sky Solar Radiation Model Based on Meteorological Parameters," *Solar Energy* **30**, pp 425–431, 1983

14 McAuthor, L.J.B. and J.E. Hay,"A technique for mapping the distribution of diffuse solar radiation over the sky hemisphere,", *J. Appl. Meterol.*,**20**(4), 421–429, 1981

15 NASA, "Chemical Kinetics and Photochemical Data of Use in Stratospheric Modeling," JPL Publication 85-37, Jet Propulsion Laboratory, Pasadena, CA, 1985.

16 Press, *et al.*, "Numerical Recipes, The Art of Scientific Computing,", Cambridge Press, New York, 1986

17 Atkinson, R. and A. Lloyd, "Kinetic and Mechanistic Data for Modeling of Photochemical Smog," *J. Phys. Chem. Ref. Data* **13** 315–444, 1983.

18 Molina, L.T. and M.J. Molina, "Absolute Absorption Cross Sections of Ozone in the 185- to 350-nm Wavelength Range," *J. Geophy. Res.*, **91** p14501–14508, 1986.